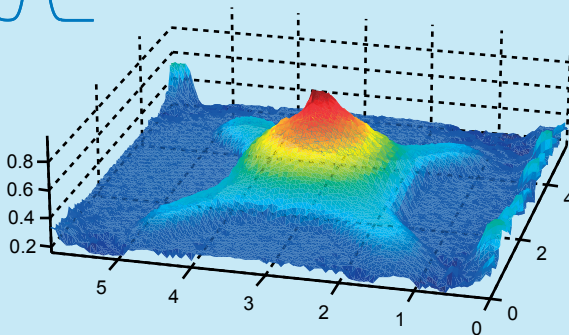
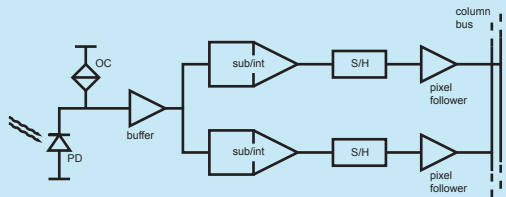
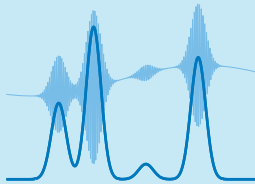


Real-Time Photon-Noise Limited Optical Coherence Tomography Based on Pixel-Level Analog Signal Processing

A dissertation submitted to the Faculty of Science of the
University of Neuchâtel for the degree of Doctor of Science
presented by

Stephan Beer



IMPRIMATUR POUR LA THESE

Real-time photon-noise limited optical coherence tomography based on pixel-level analog signal processing

Stéphane BEER

UNIVERSITE DE NEUCHATEL

FACULTE DES SCIENCES

La Faculté des sciences de l'Université de Neuchâtel,
sur le rapport des membres du jury

MM. P. Seitz (directeur de thèse),
H.P. Herzig,
R.-P. Salathé (EPF Lausanne) et
A.F. Fercher (Vienne A)

autorise l'impression de la présente thèse.

Neuchâtel, le 20 mars 2006

Le doyen :

J.-P. Derendinger

für meine geliebte Frau Christine

Abstract

This thesis presents the development of a CMOS smart imager for real-time optical coherence tomography (OCT). OCT is a measuring technique that allows the acquisition of three-dimensional pictures of discontinuities in the refractive index and phase steps in the sample. This technique has gained a lot of impact not only for many biomedical but also for industrial applications over the last few years, especially due to the achieved depth resolution in the micrometer range. It allows topographic imaging and the determination of surfaces as well as the tomographic acquisition of transparent and turbid objects. This method features an outstanding depth resolution in the sub-micrometer scale over a depth range of up to some millimeters. OCT is based on the low-coherence interferometry (white-light interferometry) with light in the visible or near infrared spectrum. The underlying physical principle allows the suppression of multiply-scattered photons in order to detect mainly ballistic photons, i.e. direct reflected photons.

The goal of this thesis was to realize a very fast, robust 3D OCT system performing close to the physical limit. A CMOS smart imager was developed as key component and an appropriate optical system was set up. This system proves that by the use of parallel optical coherence tomography (pOCT) in combination with custom designed CMOS image sensors, compact devices are realizable allowing the acquisition of topographic and cross-sectional images in real time with resolutions in the micrometer range.

Two different principles are applied in OCT imaging based either on the detection in the time-domain (TD) or the frequency-domain (FD). For TD-OCT, the reference path length of the interferometer is varied, and a simultaneous amplitude demodulation of the optical signal generates the depth image. In FD-OCT, a spectral analysis or the scanning of the illumination wavelength replaces the the path length variation.

The cross-sectional or volumetric image of a conventional TD-OCT system is gene-

rated by combining many laterally shifted one-dimensional depth scans through the object. Therefore, very fast reference path scanners and one or two translation stages are required, resulting in a non-negligible mechanical system complexity. In parallel OCT (pOCT), the translation scanners are replaced by image-forming optics and a two-dimensional image sensor. Assuming the same volume acquisition rate, this leads to a reduction of the depth scan speed by a factor corresponding to the image sensor's number of pixels, allowing real-time volumetric OCT imaging with acquisition times of some milliseconds. On the other hand, the image sensor requirements are extremely challenging: In real-time pOCT, Doppler frequencies of typically 50 kHz and more occur. In order to detect the envelope of this signal, a conventional image sensor would be required that exhibits frame rates of more than 100'000 images per second (Nyquist-Shannon sampling theorem), or, if simpler envelope detection algorithms are used, even up to 200'000 images per second. Today's fastest line sensors almost achieve line rates of this order, but area sensors are definitely slower.

The optical contrast of an OCT signal is very small, i.e. the modulation amplitude can be several decades smaller than the constant part of the signal. In this work, it is derived that the number of photons illuminating the sample limits the OCT system sensitivity, which signifies the smallest detectable reflection in the sample. This principle applies not only to TD-OCT but also to FD-OCT, and it can be used to explain the performance difference of the two principles. A relationship between the sensitivity and the number of detected photoelectrons is pointed out. From this rule of thumb, it can be concluded that the required electron storage capacity of a pOCT sensor amounts up to several millions of electrons. However, conventional image sensors feature capacities typically ranging from only tens of thousands up to hundreds of thousands of electrons.

Due to the above-mentioned reasons, a custom-designed image sensor is required for pOCT in real time. CMOS semiconductor technology allows the production of image sensors with extended functionality. Signal processing can be integrated onto the sensor and even at the pixel-level of so-called smart pixels. The pOCT sensor presented in this thesis exploits this CMOS property: Each pixel contains an offset compensation unit, a signal demodulation unit, and two global shutter units. The offset compensation unit increases the electron storage capacity to over 15 million electrons. The demodulation unit reduces the necessary external frame rate by almost two orders of magnitude to a manageable 5000 frames per second. The shutter enables the read-out of the sensor while at the same time acquiring the next image. By reading out two signals per pixel, not only is the demodulation amplitude detected but also the phase of the received signal. Therefore, the sensor is also suitable for high-resolution phase topography and polarization-sensitive OCT e.g. for the detection of birefringence coefficients. The electronic circuits in the pixel are based on the switched current (SI) and switched capa-

erator (SC) techniques, fulfilling the requirements, which are mainly due to the massive parallelism, particularly low power dissipation and small area consumption, as well as guaranteed stability. The circuit is very versatile; for example, in addition to the demodulation mode, an intensity mode is also selectable in which the sensor acquires conventional grey-level images. This mode simplifies the adjustment of the system significantly.

The presented pOCT system has a measured sensitivity of more than 90 db, which is very close to the physical limit imposed by the illumination and the depth scan speed of 20 mm/s. Therefore, it is suited not only for real-time topographic imaging, but also for a variety of tomographic applications. A phase resolution of 2° was achieved in the laboratory. The use of this information to increase the depth resolution is mainly limited by the insufficient scanner accuracy.

The developed smart imager is the world's first pOCT image sensor, which acquires the demodulation amplitude and phase close to the physical limits in real time. To our knowledge, the world's fastest TD-OCT system was realized based on this sensor. In addition, this work led to the gaining of know-how, a patent portfolio, and the foundation of a start-up company.

Keywords: Optical Coherence Tomography (OCT), real-time OCT, parallel OCT, full-field OCT, photon noise limit, parallel signal processing, smart pixel imager

Kurzfassung

Diese Dissertation handelt von der Entwicklung eines CMOS Smart Imagers für die Optische Kohärenz-Tomographie (OCT) in Echtzeit. OCT ist eine Messmethode zur Aufnahme dreidimensionaler Bilder von Sprüngen im Brechungsindex und Veränderungen in der Phasenlage. Insbesondere auf Grund der erzielten Ortsauflösung im Mikrometerbereich hat OCT in den letzten Jahren nicht nur für viele biomedizinische Anwendungen sondern auch in der Industrie enorm an Bedeutung gewonnen. OCT ermöglicht die Vermessung der Topographie von Oberflächen, als auch die tomographische Aufnahme transparenter und optisch trüber Objekte. Mit Tiefenauflösungen bis zu unter einem Mikrometer über einen Tiefenbereich von bis zu einigen Millimetern ist dieses Verfahren einzigartig. OCT basiert auf der Niederkohärenz-Interferometrie (Weisslicht-Interferometrie) mit Licht im sichtbarem oder nahen infrarot-Spektrum. In dieser Technik werden mehrfach gestreute Photonen, d.h. Photonen mit unterschiedlicher Laufzeit, unterdrückt und hauptsächlich ballistische, d.h. geradlinig reflektierte Photonen detektiert.

Das Ziel dieser Dissertation war es, ein sehr schnelles, robustes 3D OCT System zu realisieren mit einer Leistung nahe an der physikalischen Grenze. Dazu wurde ein CMOS Smart Imager entwickelt und ein entsprechendes optisches System aufgebaut. Es beweist, dass kompakte Geräte zur Erfassung von Topographien und Schnittbilder in Echtzeit mit Auflösungen im Mikrometerbereich dank der parallelen optischen Kohärenz-Tomographie (pOCT) in Kombination mit anwendungsspezifischen CMOS Bildsensoren möglich sind.

OCT Systeme werden unterschieden auf Grund ihres Detektionsprinzips in Time-Domain (TD) und Frequency-Domain (FD). In TD-OCT wird die Referenzpfadlänge verändert, und mittels gleichzeitiger Amplitudendemodulation des optischen Signals das Tiefenbild erstellt. In FD-OCT ersetzt eine spektrale Analyse oder die Änderung der Beleuchtungswellenlänge die Veränderung der Pfadlänge.

In konventionellen TD-OCT Systemen werden viele lateral versetzte eindimensionale Scans durch das Objekt zu einem Schnitt- oder Volumenbild zusammengefügt. Deshalb benötigen sie eine sehr schnelle Referenzpfadlängen-Modulation und ein, bzw. zwei Translationsscanner. Dadurch erhält das System eine nicht zu vernachlässigende mechanische Komplexität. Parallel OCT (pOCT) ersetzt die Translationsscanner durch eine Abbildungsoptik und einen zweidimensionalen Bildsensor. Bei gleicher Volumenbild-Aufnahmezeit reduziert sich dadurch auch die Geschwindigkeit des Weglängenscanners um einen Faktor entsprechend der Anzahl Pixel des Sensors. Dies ermöglicht OCT in Echtzeit mit Aufnahmezeiten von einigen Millisekunden. Dafür sind die Anforderungen an den zu verwendenden Bildsensor enorm: Bei pOCT in Echtzeit entstehen Dopplerfrequenzen von 50 kHz und mehr. Um die Umhüllende dieses Signals zu detektieren, müsste ein konventioneller Bildsensor Bildwiederholraten von mehr als 100'000 Bilder pro Sekunde (Nyquist-Shannon-Abtasttheorem), bzw. für eine vereinfachte Detektion mittels Hüllkurven-Detektionsalgorithmen, 200'000 Bilder pro Sekunde aufweisen. Die schnellsten Zeilensensoren erreichen heute beinahe Zeilenwiederholraten dieser Grössenordnung, Flächensensoren sind definitiv langsamer.

Der optische Kontrast eines OCT Signals ist sehr klein, d.h. die Modulationsamplitude ist mehrere Dekaden kleiner als der konstante Anteil des Signals. In dieser Arbeit wird hergeleitet, dass die Sensitivität eines OCT Systems, also das Mass für die kleinste detektierbare Reflexion in der Probe, durch die Anzahl der auf die Probe auftreffender Photonen physikalisch limitiert ist. Diese Formel gilt nicht nur für TD-OCT sondern auch für FD-OCT, und erklärt den Leistungsunterschied der beiden Prinzipien. Ein Zusammenhang mit der Anzahl detektierter Photoelektronen wird aufgezeigt. Aus dieser Regel wird geschlossen, dass ein pOCT Sensor eine Elektronen-Speicherkapazität von mehreren Millionen Elektronen braucht. Konventionelle Bildsensoren haben aber typischerweise Speicherkapazitäten von nur zehntausenden bis hunderttausenden von Elektronen.

Aus den hier genannten Gründen ist deshalb für pOCT in Echtzeit ein dedizierter Bildsensor notwendig. CMOS Halbleiterherstellungsprozesse gestatten die Fertigung von Bildsensoren mit erweiterter Funktionalität. Signalverarbeitung kann nicht nur auf den Sensor, sondern sogar direkt in die so genannten Smart-Pixel integriert werden. Der im Rahmen dieser Arbeit entwickelte pOCT Sensor baut auf dieser CMOS Eigenschaft auf: Jedes Pixel beinhaltet eine Offset-Kompensationseinheit, eine Signal-Demodulationseinheit und zwei Global Shutter. Die Offset-Kompensationseinheit erhöht die Elektronen-Speicherkapazität auf über 15 Millionen Elektronen. Die Demodulationseinheit reduziert die benötigte externe Bildwiederholrate um beinahe zwei Grössenordnungen auf zu bewältigende 5000 Bilder pro Sekunde. Der Shutter, ein elektronischer Verschluss, ermöglicht es, den Sensor auszulesen und gleichzeitig schon das nächste Bild aufzunehmen. Das Auslesen von zwei Signalen pro Pixel erlaubt nicht

nur die Amplitudendetektion, sondern auch die Auswertung der Phase des empfangenen Signals. Der Sensor eignet sich daher auch für hochauflösende Phasen-Topographie und polarisationssensitives OCT z.B. zur Detektion von Doppelbrechungskoeffizienten. Die elektronischen Schaltkreise im Pixel basieren auf den Switched Current (SI) und Switched Capacitor (SC) Techniken und erfüllen die Anforderungen der massiven Parallelisierung, wie besonders sparsamer Stromverbrauch, kleine Siliziumfläche und garantierte Stabilität. Die Schaltung ist sehr flexibel einsetzbar, z.B. kann neben dem Demodulationsmodus auch ein Intensitätsmodus gewählt werden, in dem der Sensor ein normales Graustufenbild erzeugt, was die Justierung des Systems vereinfacht.

Das hier präsentierte pOCT System hat eine maximale gemessene Sensitivität von 90 dB, und liegt damit nur ganz wenig unter der durch die Beleuchtung und die Scangeschwindigkeit von 20 mm/s gegebenen physikalischen Grenze. Er eignet sich damit vor allem für topographische, aber auch für einige tomographische Echtzeit-Anwendungen. Eine Phasenauflösung genauer als 2° wurde im Labor erreicht. Limitierend bei der Verwendung der Phaseninformation zur Erhöhung der Auflösung ist vor allem die ungenügende Scannergenauigkeit.

Der entwickelte Smart Imager ist der welterste pOCT-Bildsensor, der in Echtzeit Amplituden-Demodulation und Phasenmessung nahe an der physikalischen Grenze durchführt. Auf der Basis dieses Sensors wurde das unseres Wissens weltweit schnellste TD-OCT System realisiert. Zusätzlich führte diese Arbeit zum Aufbau von Know-how und eines Patent-Portfolios, welches die Gründung einer Start-up Firma ermöglichte.

Stichwörter: Optische Kohärenztomographie (OKT), OKT in Echtzeit, parallele OKT, abbildende OKT, Photonenrauschgrenze, parallele Signalprozessierung, Bildsensor mit intelligenten Pixel

Contents

Abstract	vii
Kurzfassung	xi
1 Introduction	1
1.1 Motivation	1
1.2 Thesis outline	4
Bibliography	5
2 Theory of Optical Coherence Tomography	7
2.1 Low-coherence interferometry and axial resolution	7
2.1.1 Illumination spectrum and temporal coherence function	7
2.1.2 Spatial coherence	11
2.1.3 Interferogram	11
2.1.4 Axial resolution	12
2.2 OCT signal detection and sensitivity	12
2.2.1 Detection: phase and group delay	12
2.2.2 Signal to noise ratio and sensitivity	13
2.2.3 Noise sources	16

2.3	Phase detection	17
2.4	Lateral resolution and depth range	17
2.5	Frequency domain OCT	18
	Bibliography	21
3	State of the art parallel OCT	23
3.1	Introduction	23
3.2	Full-field optical coherence microscopy	24
3.3	Illumination of pOCT systems	24
3.4	Smart pixel detectors for pOCT	25
3.4.1	Limitations of standard CCD and CMOS APS image sensors	25
3.4.2	POCT smart pixels with product demodulation using a rectifier	26
3.5	Conclusion	27
	Bibliography	31
4	Fundamental physical and technical limitations of pOCT	33
4.1	SNR and optical power in pOCT	33
4.2	Natural sampling	34
4.3	Comparison of the SNR of TD-OCT, TD-pOCT, and FD-OCT	35
4.4	Performance degradation by modulation frequency mismatch and vibrations	39
4.4.1	Scan speed mismatch	39
4.4.2	POCT under vibrations	40
4.5	Conclusion	43
	Bibliography	45
5	An Optimized Smart pOCT Pixel	47

5.1	Introduction	47
5.2	Theory on pOCT sensors	48
5.2.1	In-pixel demodulation requirements	49
5.2.2	Different demodulation principles	50
5.2.3	Transducer stage with offset reduction	56
5.3	Realization of the discrete time direct demodulation pixel architecture	61
5.3.1	Targeted specifications	62
5.3.2	Pixel architecture	63
5.3.3	Transducer stage	64
5.3.4	Demodulation stage	67
5.3.5	Pixel readout circuit	72
5.3.6	Noise analysis and dimensioning of C_{sub} and C_{int}	75
5.3.7	Intensity mode	76
5.3.8	Pixel Layout	78
	Bibliography	82
6	POCT System Realization	83
6.1	POCT high-speed image sensor	83
6.2	High-speed data acquisition and system control electronics	88
6.2.1	POCT camera	88
6.2.2	Software for POCT data acquisition and viewing	88
6.2.3	Axial scanner	90
6.3	Optical set-up	90
6.4	Conclusion	92
	Bibliography	93

7	POCT measurements and system performance	95
7.1	Sensitivity measurements	95
7.1.1	Experimental set-up	96
7.1.2	Data processing	96
7.1.3	Results and discussion	99
7.2	Phase measurements	103
7.2.1	Experimental set-up	103
7.2.2	Signal processing and expected performance	104
7.2.3	Results and discussion	105
7.3	Demodulation frequency mismatch and vibrations	106
7.3.1	Mismatch of modulation and demodulation frequency	107
7.3.2	Sample vibration effects	109
7.4	Grey-level imaging performance	110
7.4.1	Optimum number of integration cycles N	110
7.4.2	Sensor characterization in grey-level mode	111
7.5	Conclusion	113
	Bibliography	114
8	Applications	115
8.1	High-speed topography imaging	115
8.1.1	Measurements	116
8.1.2	Results and discussion	117
8.2	Conclusion	118
	Bibliography	119
9	Conclusion	121

Bibliography	125
A Appendix: Formulas	127
A.1 Gaussian illumination spectrum	127
A.2 Rectangular illumination spectrum	128
A.3 Theoretical <i>SNR</i> and sensitivity	129
A.4 <i>SNR</i> calculation from measurements	130
A.5 Theoretical phase noise due to the limited amplitude <i>SNR</i>	131
Bibliography	131
Acknowledgments	133
Curriculum Vitae	135

Chapter 1

Introduction

1.1 Motivation

We live in a three-dimensional world, and the human visual system is well adapted to it, allowing us to perceive three-dimensional images in a large range in real-time. Due to the properties of light and its interaction with matter, as well as the so-called visible spectrum range that we are able to perceive, we mostly see only the outside of objects. But mankind's curiosity always drove us towards the hidden, to get insight, to look behind the surface, and through things, in the figurative sense but also literally. The first approach is the dissection of the objects, which usually leads to the destruction of the examined sample. Similarly, we increased the distance range of our visual perception to the very large scale with telescopes and to the very small scale with microscopes of many kind. A price often paid for this extension of range is the loss of information about the third dimension. Optical coherence tomography (OCT) is an emerging technique that extends our visible range to the micrometer scale and offers three-dimensional information. Furthermore it even allows imaging of structures inside turbid objects. The goal of this thesis was to develop an OCT system, offering this functionality in real-time.

OCT and the related technique white-light interferometry for surface detection is based on low-coherence interferometry. A typical interferometric set-up is the Michelson interferometer shown in Fig. 1.1(a). The beam splitter divides the optical wave from the source into two paths and recombines them after they have been reflected by mirrors. The recombined wave is detected by an optoelectronic device. If the light from the two beams is at least partially coherent, i.e. the phase fluctuations of the two waves

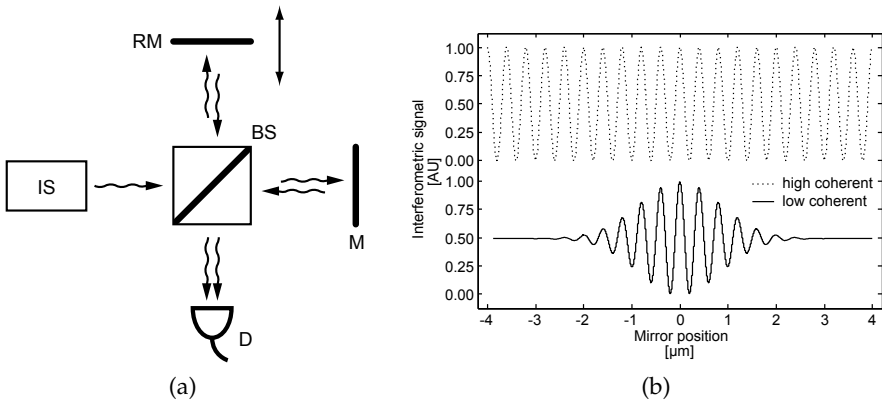


Figure 1.1: Interferometry with temporally coherent and incoherent illumination sources: (a) Michelson interferometer with an illumination source (IS) and a beam splitter (BS) that divides the light beam into two paths. These two beams are reflected by a static mirror (M) and a reference mirror (RM) with variable position and recombine at the detector (D). (b) The interferogram is the detected signal strength in e.g. optical power, versus the reference mirror position. Two light sources with the same center wavelength $\lambda_0 = 800 \text{ nm}$ are compared. The high-coherence source, such as a laser, features a coherence length much larger than the maximum path difference between the two interferometer arms. The simulated low-coherence source such as a femtosecond laser or a thermal light source has a coherence length FWHM of only $4 \mu\text{m}$. In both cases, the detected signal is modulated with a period corresponding to $\lambda_0/2$.

are related instead of being completely random, the two waves interfere. This means that the detected optical power depends on the difference of the lengths of the two paths. Typically, the power is sinusoidally modulated as function of the optical path difference with a period corresponding to the wavelength. The interferogram is the measured optical power at the detector as a function of the position of one of the two mirrors called reference mirror. If the illumination source of the interferometer is coherent, e.g. a laser, the signal modulation stretches over a large interferometer arm length difference of up to many meters. If the source is of so-called low temporal coherence, such as an light emitting diode (LED) or a thermal lamp, the width of the modulated packet, called coherence length, becomes very small and may even be of the order of a micrometer. If now the reference mirror is moved in a controlled manner and the optical signal is analyzed to detect the signal modulation, the position of the static mirror can be detected unambiguously with a precision corresponding to half of the coherence length. In OCT, the static mirror is replaced by a sample, and since every reflecting interface of the sample generates a signal modulation at the corresponding reference mirror position, cross-sectional images can be acquired even through scatter-

ing material [1,2].

Most systems exploiting the above explained time-domain (TD-) OCT principle, acquire a depth scan for one lateral position of the sample at a time, a so-called A-scan, then move to a laterally neighboring position to acquire the next scan, and so on. Cross-sectional or volumetric images are then composed of a multitude of A-scans. Real-time volumetric imaging, which is a requirement for many applications, is with this principle only achievable by the use of extremely fast axial scanners. By replacing the single-spot detector by a detector array, a three-dimensional image is acquired by one depth scan [3–5]. This so-called parallel OCT (pOCT) or full-field OCT also reduces the complexity and costs of the system.

POCT potentially achieves very high 3D frame rates due to the simultaneous acquisition of a multitude of measurement spots. For real-time 3D imaging, the requirements for the image sensor are extremely high. Frame rates in the order of 200'000 frames per second have to be achieved with charge handling capabilities of the order of a million photoelectrons and more. No commercially available system meets these requirements. A custom design imager therefore needed to be developed. The versatility of semiconductor technology allows the monolithic integration of photosensitive, analog and digital functionality on a single chip. In so-called smart pixel imagers, additional signal processing is even executed at the pixel level [6]. To achieve the above mentioned real-time 3D tomographic imaging performance, it was decided to develop a pOCT system based on a dedicated CMOS sensor with massively parallel signal processing at the pixel level. The main focus of this work is the development of a smart pixel architecture and a complete sensor that achieves the above stated requirements [7,8]. In previous work, a former generation pOCT sensor has already been developed by Bourquin [9,10]. The new pixel architecture is based on a different demodulation principle. This allowed to increase the sensitivity, while at the same time reducing the pixel size and improving circuit robustness.

The performance of an OCT system is characterized by the following proprieties: the number of acquired voxels* per complete two-dimensional or three-dimensional image, the axial and lateral resolution, the depth range, the acquisition time, the dynamic range, and the sensitivity, which represents the smallest detectable reflection. These proprieties are all related and physically limited by the choice of the illumination source. Besides high-speed operation, sensitivity performance near the physical limit has been emphasized, which is imposed by the Poisson distribution of light.

* volumetric pixels

1.2 Thesis outline

This thesis consists of nine chapters, each of them, except for this first and the last, focussing on a different aspect or development step of the pOCT demonstrator system. Chap. 2 explains the physical principles behind OCT. The notions and parameters characterizing an OCT system are discussed. In Chap. 3, state of the art parallel OCT imaging and the related technique parallel optical coherence microscopy (OCM) are presented. The focus is laid on pOCT imaging with conventional two-dimensional image sensors and the first-generation pOCT smart pixel sensor mentioned above. Chap. 4 then investigates the fundamental physical but also technical limits of pOCT imaging performance, especially for the targeted smart pixel architecture. The smart pixel TD-pOCT system is compared to scanning TD-OCT and frequency-domain (FD-) OCT. Also the effects of vibrations in the system and scan speed variations are analyzed. The next two chapters present the development that has been accomplished within the scope of this thesis: Chap. 5 specifies the task of a smart pixel dedicated to pOCT imaging. Different concepts for pixel-level signal demodulation are discussed together with high signal-offset removal techniques. In the second part of this chapter, the developed smart pixel architecture is presented in detail. Chap. 6 then describes the implementation of the high-speed pOCT sensor based on the smart pixel architecture. The final pOCT system and especially its parts control electronics, optical set-up, and axial scanner are presented. Chap. 7 is devoted to the experimental analysis of the pixel and the system performance. Measurements of the sensitivity, the phase accuracy, and the grey-level imaging properties are described and their results discussed in detail. The influence of vibrations and speed variations is also experimentally verified. Chap. 8 finally presents results of smart pixel pOCT imaging for an industrial quality control application.

Bibliography

- [1] D. Huang, E. A. Swanson, C. P. Lin, J. S. Schuman, W. G. Stinson, W. Chang, M. R. Hee, T. Flotte, K. Gregory, C. A. Puliafito, and J. G. Fujimoto, "Optical coherence tomography," *Science*, vol. 254, pp. 1178–1181, 1991.
- [2] J. M. Schmitt, "Optical coherence tomography (OCT): A review," *IEEE J. Quantum Electron.*, vol. 5, pp. 1205–1215, 1999.
- [3] G. S. Kino and S. S. C. Chim, "Mirau correlation microscope," *Appl. Opt.*, vol. 29, pp. 3775–3783, Sept. 1990.
- [4] T. Dresel, G. Häusler, and H. Venzke, "Three-dimensional sensing of rough surfaces by coherence radar," *Appl. Opt.*, vol. 31, pp. 919–925, Mar. 1992.

- [5] E. Beaurepaire, A. C. Boccara, M. Lebec, L. Blanchot, and H. Saint-Jalmes, "Full-field optical coherence microscopy," *Opt. Lett.*, vol. 23, pp. 244–246, Feb. 1998.
- [6] P. Seitz and N. Blanc, "CCD and APS/CMOS technology for smart pixels and image sensors," in *Detectors and Associated Signal Processing* (J. P. Chatard and P. N. J. Dennis, eds.), vol. 5251 of *Proc. SPIE*, pp. 142–153, Feb. 2004.
- [7] S. Beer, S. Waldis, and P. Seitz, "Video-rate optical coherence tomography imaging with smart pixels," in *Optical Coherence Tomography and Coherence Techniques* (W. Drexler, ed.), vol. 5140 of *Proc. SPIE*, pp. 69–76, June 2003.
- [8] S. Beer, P. Zeller, N. Blanc, F. Lustenberger, and P. Seitz, "Smart pixels for real-time optical coherence tomography," in *Three-Dimensional Image Capture and Applications VI* (B. D. Corner, P. Li, and R. P. Pargas, eds.), vol. 5302 of *Proc. SPIE*, pp. 21–32, Apr. 2004.
- [9] S. Bourquin, V. Monterosso, P. Seitz, and R. P. Salathé, "Video-rate optical low-coherence reflectometry based on a linear smart detector array," *Opt. Lett.*, vol. 25, pp. 102–104, Jan. 2000.
- [10] S. Bourquin, P. Seitz, and R. P. Salathé, "Optical coherence topography based on a two-dimensional smart detector array," *Opt. Lett.*, vol. 26, pp. 512–514, Apr. 2001.

Chapter 2

Theory of Optical Coherence Tomography

2.1 Low-coherence interferometry and axial resolution

Optical coherence tomography is based on low coherence interferometry. Fig. 2.1(a) shows a Michelson interferometer. The light beam from the illumination source is divided into two paths by the beam splitter. In the sample path, the light is partially reflected by the inspected sample; in the reference path, the reference mirror reflects the beam. The two beams are recombined in the beam splitter. At the detector, the incoming photons are converted into electrical charges that are further analyzed by the detection electronics.

The following section describes the theory leading to the optical intensity signal of a low coherence interferogram shown in Fig. 2.1(b).

2.1.1 Illumination spectrum and temporal coherence function

The complex wave function $V(t)$ describes the light beam of the interferometer illumination, in the case of a spatially coherent source. Its intensity in power per unit area is given as the wave function's time-averaged absolute square $I = \langle |V(t)|^2 \rangle_T$. The wave function itself can be characterized by two related properties: its power spectral density or spectrum $S(\nu)$, and its complex temporal coherence function $\Gamma(\tau)$. Although the Fourier transform of $V(t)$ does not exist, since it does not necessarily fulfill the Dirichlet condition*, the power spectral density exists as the limit of the absolute square of

* The weak Dirichlet condition states that the Fourier transform of $V(t)$ exists, if $\int_{-\infty}^{+\infty} |V(t)| dt < \infty$

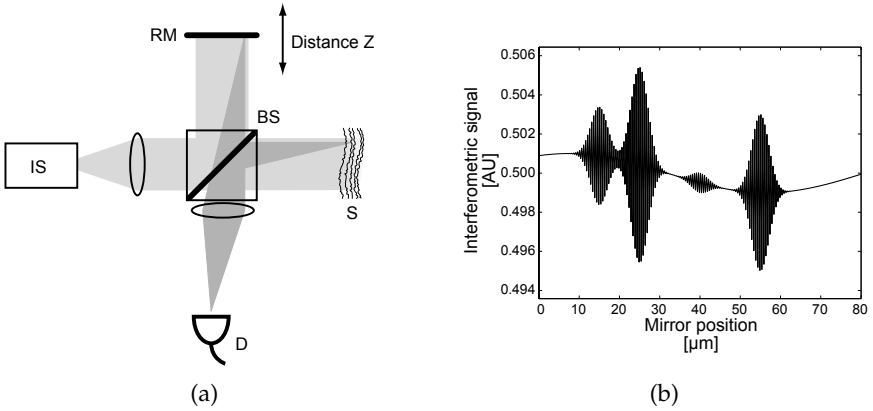


Figure 2.1: Low coherence interferometry: (a) Michelson interferometer with an illumination source (IS) and a beam splitter (BS) that splits the light beam into two paths. These two beams are reflected by the reference mirror (RM) and the sample (S) and recombine at the detector (D). (b) The interferogram shows the measured intensity as a function reference mirror position: Every reflecting site in the sample produces a fringe packet: the intensity is modulated with a period corresponding to half the central wavelength $\lambda_0/2$. The amplitude of the fringe packet envelope is proportional to the square root of the corresponding reflection coefficient, and its width, i.e. the interferogram’s axial resolution σ_z , is determined by the illumination spectrum.

the Fourier transform approximation of $V(t)$:

$$\hat{V}_T(\nu) = \int_{-T}^{+T} V(t) \cdot e^{-j2\pi\nu t} dt \tag{2.1a}$$

$$S(\nu) = \lim_{T \rightarrow \infty} \frac{1}{2T} \langle |\hat{V}_T(\nu)|^2 \rangle_{E'} \tag{2.1b}$$

where $\langle \rangle_E$ denotes the ensemble average. It is zero for negative frequencies and non-negative for positive frequencies and represents the amount of average power per unit area and frequency of the wave function $V(t)$ as a function of the frequency ν . The total intensity can be expressed as its integral

$$I = \int_0^{\infty} S(\nu) d\nu. \tag{2.2}$$

The temporal coherence function of the wave is defined as its autocorrelation function

$$\Gamma(\tau) = \langle V^*(t)V(t+\tau) \rangle, \quad (2.3)$$

where $\langle \rangle$ denotes time averaging. It carries not only information about the coherence of the illumination wave function but also about its intensity ($I = \Gamma(0)$). The so-called complex degree of temporal coherence γ is the normalized form of the temporal coherence function and is independent of the signal intensity

$$\gamma(\tau) = \frac{\Gamma(\tau)}{\Gamma(0)} = \frac{\langle V^*(t)V(t+\tau) \rangle}{I_0} \quad (2.4)$$

and describes the degree of correlation between a wave and a by τ time shifted copy of itself. It features a Hermitian symmetry e.g. $\gamma(-\tau) = \gamma^*(\tau)$, is unity for $\tau = 0$, and usually has a decreasing modulus for an increasing time delay.

For quasi-monochromatic waves, i.e. when the power of the spectrum is contained in a rather narrow band around a center frequency ν_0 , $\Delta\nu \ll \nu_0$, the complex degree of coherence can be expressed as

$$\gamma(\tau) = |\gamma(\tau)| \cdot e^{j2\pi\nu_0\tau} \cdot e^{j\varphi_\gamma(\tau)}, \quad (2.5)$$

where the autocorrelation phase $\varphi_\gamma(\tau)$ varies slowly compared to $2\pi\nu_0\tau$.

The coherence time τ_c represents a rather arbitrarily chosen limit to distinguish wave superpositions into strongly correlated (e.g. interfering) and weakly or not correlated as a function of its time delay. Different definitions exist, e.g.

$$\tau_{c1} = \int_{-\infty}^{+\infty} |\gamma(\tau)|^2 d\tau \quad (\text{power equivalent width}) \quad (2.6a)$$

$$|\gamma(\tau = \tau_c/2)| = \frac{1}{2} \quad (\text{FWHM}), \quad (2.6b)$$

where Eq. 2.6b defines the coherence time as full width at half maximum (FWHM) and will be employed in this work for its simplicity and because it allows to directly derive the depth resolution of an OCT system. For an optical system such as the interferometer shown in Fig. 2.1(a), the delay between two waves is usually measured as a distance. The coherence time translates into the coherence length by $l_c = c\tau_c$, where c denotes the speed of light in the corresponding medium.

Since the Wiener-Khinchin theorem relates the power spectral density to the temporal

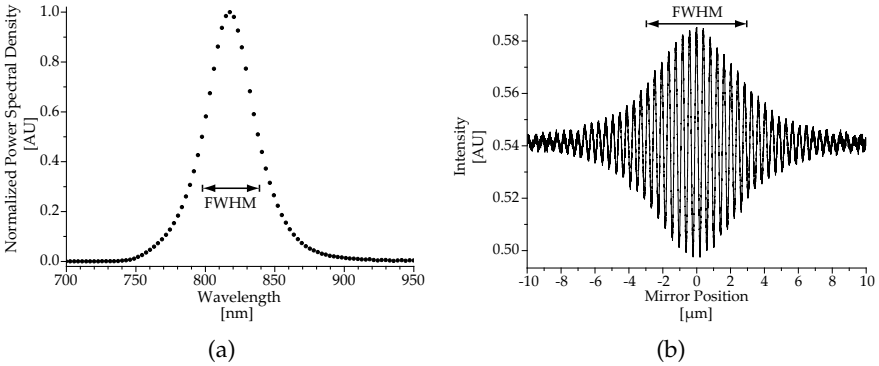


Figure 2.2: Spectrum and interferogram of an LED (EPIGAP ELJ-810_228B): (a) The LED has an almost Gaussian distribution with a peak wavelength of $\lambda_0 \simeq 820$ nm and a spectrum width (FWHM) of $\Delta\lambda \simeq 45$ nm, leading to a theoretical coherence length of $l_c \simeq 13.0$ μm . (b) The measured interferogram versus the reference mirror position shows a modulation period corresponding to half of the wavelength. The envelope width (FWHM) or depth resolution corresponds to almost half of the calculated coherence length. The contrast is about $\mathcal{V} \simeq 7\%$.

coherence function as a Fourier transform pair

$$S(\nu) = \int_{-\infty}^{+\infty} \Gamma(\tau) e^{-j2\pi\nu\tau} d\tau \quad \Gamma(\tau) = \int_0^{+\infty} S(\nu) e^{j2\pi\nu\tau} d\nu, \quad (2.7)$$

the coherence time τ_c is inversely proportional to the FWHM of the power spectral density. Many illumination sources have a Gaussian-like spectrum as the LED shown in Fig. 2.2(a). For a Gaussian spectrum such as

$$S(\nu) = I_0 \cdot \frac{2\sqrt{\frac{\ln 2}{\pi}}}{\Delta\nu} \cdot e^{-4\ln 2 \frac{(\nu-\nu_0)^2}{\Delta\nu^2}}, \quad (2.8)$$

the temporal coherence function has also a Gaussian modulus e.g. has no sidelobes, and features a FWHM coherence length of (see App. A.1)

$$l_c = \frac{4\ln 2}{\pi} \cdot \frac{c}{\Delta\nu} = \frac{4\ln 2}{\pi} \cdot \frac{\lambda^2}{\Delta\lambda}. \quad (2.9)$$

2.1.2 Spatial coherence

The concept of temporal coherence can be extended to the mutual coherence by considering also spatial coherence i.e. the correlation between the fluctuations of the illumination wave at two different positions \mathbf{r}_1 and \mathbf{r}_2 . The complex degree of coherence is

$$\gamma(\mathbf{r}_1, \mathbf{r}_2, \tau) = \frac{\Gamma(\mathbf{r}_1, \mathbf{r}_2, \tau)}{\sqrt{\Gamma(\mathbf{r}_1, \mathbf{r}_1, 0)\Gamma(\mathbf{r}_2, \mathbf{r}_2, 0)}} = \frac{\langle V^*(\mathbf{r}_1, t)V(\mathbf{r}_2, t + \tau) \rangle}{\sqrt{I(\mathbf{r}_1)I(\mathbf{r}_2)}}. \quad (2.10)$$

Parallel or wide-field OCT can suffer from optical cross-talk between the parallel detection channels due to multiply scattered light from the full-field illuminated sample. In point-scanning OCT, this noise is significantly suppressed by the focused sample illumination and the pinhole propriety of the single mode fibre receiving the reflected light. In parallel OCT, a similar cross-talk suppression can be achieved by exploiting the properties of spatially incoherent light sources [1-3].

2.1.3 Interferogram

In the interferometer, the wave is split into the two arms and recombined later on. V_r is the wave reflected by the reference mirror, V_s the one from the sample. The measured intensity on the detector for a spatially coherent illumination source is given by

$$I_D(\tau) = \langle |V_r(t) + V_s(t)|^2 \rangle = \langle |s_r V(t + \tau) + s_s V(t)|^2 \rangle \quad (2.11a)$$

$$= I_{D0} \cdot \left[1 + \frac{2|s_r s_s|}{|s_r|^2 + |s_s|^2} |\gamma(\tau)| \cos(2\pi\nu_0\tau + \varphi_g(\tau) + \Delta\phi_{sr}) \right] \quad (2.11b)$$

$$\simeq I_{D0} \cdot \left[1 + \mathcal{V}(\tau) \cos(2\pi\nu_0\tau + \Delta\phi) \right], \quad (2.11c)$$

where I_{D0} is the average optical intensity, which is the sum of the average intensity coming from the reference and from the sample arm. In the case of a semitransparent sample with several reflecting interfaces, interference fringes are detected for each of them at their corresponding depth position. The envelope amplitude, expressed as fringe visibility \mathcal{V} , is proportional to the square root of the power reflectance of the coherently detected interface:

$$\mathcal{V} = \frac{I_{D_{\max}} - I_{D_{\min}}}{I_{D_{\max}} + I_{D_{\min}}} = \frac{2\sqrt{R_{sc}R_r}}{R_{\text{tot}} + R_r} |\gamma(\tau)| \xrightarrow{R_{sc} \ll R_{\text{tot}} \ll R_r} 2\sqrt{\frac{R_{sc}}{R_r}} |\gamma(\tau)|, \quad (2.12)$$

where R_r is the power reflectance in the reference arm, R_{s_c} the reflectance of the coherently detected sample interface and $R_{s_{tot}}$ is the total power reflectance of the sample.

By reducing the intensity coming from the reference arm, e.g. its power reflectance R_r to match the total sample reflectance $R_{s_{tot}}$, the OCT signal contrast can be increased at the cost of a loss in the detected signal to noise ratio (SNR), as will be shown later.

2.1.4 Axial resolution

The depth resolution σ_z of an OCT system is the minimum distance in the scan direction for which two reflecting sites with reflection coefficients of the same order still can be distinguished. It is defined as half of the FWHM coherence length l_c :

$$\sigma_z = \frac{l_c}{2} = \frac{2 \ln(2)}{\pi} \cdot \frac{\lambda_0^2}{\Delta\lambda}. \quad (2.13)$$

Resolutions in the sub-micrometer range have been reported for tomographic imaging with light sources of several 100 nm spectral width [4–7].

The broader the illumination spectrum respectively the better the axial resolution is, the larger is the influence of the group velocity dispersion: different wavelengths propagate with different non-linearly related velocities. The dispersion in an optical system can be compensated [4] but in some samples this is hardly possible, leading to a broadening of the coherence function and degrading of the depth resolution.

2.2 OCT signal detection and sensitivity

Most time-domain (TD-) OCT systems use heterodyne detection, i.e., the optical path length difference between the reference and the sample path is changed at a constant speed, and the detected signal is analyzed resulting in a one-dimensional data set of power reflection coefficients versus depth position, called A-scan. In point scanning OCT, many A-scans are acquired consecutively to form a two- or three-dimensional image, while in parallel or full-field OCT all A-scans are acquired simultaneously.

2.2.1 Detection: phase and group delay

By sweeping the optical path difference between the two interferometer arms, the detected photocurrent, which is proportional to the interferogram described by Eq. 2.11,

becomes a time-domain signal. Its center frequency or carrier is determined by the phase delay scan speed V_ϕ and the carrier of the complex coherence function, and is therefore related to the illumination source spectrum. For an optical delay line consisting of a moving reference mirror with a scan speed $v = V_\phi/2$, the center frequency of the detected signal becomes

$$f_D = \frac{2v}{\lambda_0}, \quad (2.14)$$

where λ_0 is the center wavelength. This so-called Doppler frequency corresponds to the beat frequency of the optical heterodyne detector response.

Every frequency component of the detected signal is related by the group delay scan speed V_g to the coherence function. For a moving mirror, the group delay scan speed equals the phase delay scan speed $V_g = V_\phi$, and the detected photocurrent becomes

$$I_{\text{el}}(t) \simeq \frac{\eta P_{D0}}{hc/\lambda_0} q_e \cdot \left[1 + \mathcal{V}(t) \cos(2\pi f_D t + \Delta\phi) \right], \quad (2.15)$$

where η is the probability that a photon generates an electron-hole pair in the photodiode, P_{D0} is the optical power on the photosensitive area, and q_e is the electron charge. The bandwidth of the photocurrent signal is given by

$$\Delta f = f_D \cdot \frac{\Delta\lambda}{\lambda_0}. \quad (2.16)$$

2.2.2 Signal to noise ratio and sensitivity

OCT systems achieve very high detection sensitivities, since due to the underlying interferometric measuring method, rather the electromagnetic field amplitude instead of its intensity is detected. The sensitivity of the OCT system is a measure for the minimum detectable reflectivity in the sample. In this section the OCT SNR and the sensitivity in the shot-noise limited case are derived.

The signal to noise ratio *SNR* of an optical system is defined as the ratio of the squared mean value of the output signal and its variance [8]. The standard deviation or noise of an optical signal of a certain mean number of photons \bar{n} equals its square root $\sqrt{\bar{n}}$ (shot noise due to the Poisson statistics.) The *SNR* becomes

$$SNR = \frac{\bar{n}^2}{\sigma_n^2} = \bar{n} = \bar{\Phi} \cdot T = \frac{\bar{P}T}{h\nu}, \quad (2.17)$$

where $\bar{\Phi}$ is the mean value of the photon flux in photons per second on the detection

area, T the integration time, \bar{P} is the optical power, and $E_{\text{ph}} = h\nu$ is the photon energy. The electron/hole pair generation by photon absorption in the semiconductor and their separation due to an electric field, e.g. in the depletion zone of a diode, is a random process of probability η called quantum efficiency. If these electron/hole generations are treated as independent events, the photo-electron probability distribution is a sum of binomial distributions weighted with the photon distribution. In the case of a Poisson (coherent light) or a Bose-Einstein (single mode thermal light) photon distribution, the photon and the photo-electron distributions are of the same form [9]. In our case, where a Poisson distribution is assumed, the optical SNR translates into the electronic $SNR_{\text{el}} = \eta\bar{n} = \eta\bar{P}T/h\nu$, for a shot-noise limited sensor, i.e. a detection system, for which the electrical circuit noise is much smaller than the shot noise of the photogenerated charges $\sigma_{n_{\text{el}}} = \sqrt{\eta\bar{n}}$.

In optical coherence tomography, the signal of interest is the modulated part of the incoming light with a modulation frequency corresponding to the Doppler frequency f_D . Hence, the SNR may be expressed as

$$SNR_{\text{OCT}} = \frac{(\eta n_{\text{mod}})^2}{\sigma_{\eta n_{\text{total}}}^2}, \quad (2.18)$$

where n_{mod} is the root mean square number of modulation photons

$$n_{\text{mod}} = \frac{P_{\text{mod}}T}{h\nu} = \frac{T}{h\nu} \cdot \sqrt{\langle (P - \bar{P})^2 \rangle_T}. \quad (2.19)$$

By injecting the optical power proportional to the above mentioned detector photocurrent (Eq. 2.15) into Eq. 2.19 the number of modulated photons becomes

$$n_{\text{mod}} = \frac{T}{h\nu} \cdot 2 \sqrt{P_r P_s} \cdot \sqrt{\langle (|\gamma(t)| \cdot \cos(2\pi f_D t + \Delta\phi))^2 \rangle_T}, \quad (2.20)$$

where $P_{r,s}$ are the optical powers on the detector coming from the reference path and the sample path, respectively.

With a correctly chosen integration bandwidth (noise equivalent filter bandwidth) $NEB = 2\Delta f = 2f_D \Delta\lambda/\lambda_0$ as proposed by [10], corresponding to an integration time $T = 1/2 \cdot NEB^*$, the influence of the amplitude of the complex degree of coherence becomes negligible

* The equivalent signal duration and the noise equivalent filter bandwidth have the following relation: $NEB \times T_{\text{eq}} \geq 0.5$. For signals that are always positive, $NEB \times T_{\text{eq}} = 0.5$, this can be assumed for OCT low-pass filtering [8].

for a measurement taken around the envelope center,

$$\begin{aligned} \langle |\gamma(t)|^2 \rangle_T &= \frac{1}{T} \cdot \int_{-T/2}^{+T/2} e^{-\frac{\pi^2}{2 \ln 2} \cdot \left(\frac{\Delta \lambda}{\lambda_0}\right)^2 \cdot f_B^2 \cdot t^2} dt \\ &= \sqrt{\frac{8 \ln 2}{\pi}} \cdot \operatorname{erf} \left(\pm \frac{\pi}{8 \sqrt{2 \ln 2}} \right) \Big|_{-}^{+} = 0.964 \end{aligned} \quad (2.21)$$

The number of modulation photons therefore is

$$n_{\text{mod}} \simeq \frac{T}{h\nu} \cdot \sqrt{2P_r P_{s_c}}, \quad (2.22)$$

where P_{s_c} is the coherently detected power counting all the photons reflected by a site in the sample for which the optical path difference between the reference and the sample arm is near zero. The maximum OCT SNR becomes

$$\text{SNR} \simeq \frac{\eta}{h\nu \cdot \text{NEB}} \cdot \frac{P_r P_{s_c}}{P_r + P_{s_{\text{tot}}}}. \quad (2.23)$$

This can be simplified in the case where the power from the reference arm is much larger than the power reflected by the sample $P_r \gg P_{s_{\text{tot}}}$ to

$$\text{SNR} \simeq \frac{\eta P_{s_c}}{h\nu \cdot \text{NEB}}, \quad (2.24)$$

which is the common definition [10–12]. This is a factor 2 more than could have been intuitively guessed by the Poisson distribution described by Eq. 2.17 of the coherently detected optical power. Often the power from the reference arm is attenuated to match with the total power reflected from the sample $P_{s_{\text{tot}}}$ in order to increase the signal visibility \mathcal{V} , to avoid sensor saturation, and to reduce the relative intensity noise treated in the next section [13, 14]. As long as the optical power from the reference arm is still much higher than the power reflected by the sample, the above stated simplification holds.

The OCT sensitivity S is defined as the smallest detectable power reflection, e.g. the reflectance leading to an SNR of unity. In the case of an ideal Michelson interferometer with a 50/50 beam splitter, the coherently detected power from the sample can be rewritten as $P_{s_c} = R_{s_c} \cdot P_0/4$, where P_0 is the total optical power of the illumination source. In a photocharge shot-noise limited OCT system, the sensitivity becomes

$$S = \frac{1}{R_{s_c, \text{min}}} \simeq \frac{\eta}{h\nu \cdot \text{NEB}} \cdot \frac{P_0}{4}. \quad (2.25)$$

In the case of $R_r = 1$, the sensitivity corresponds to twice the number of received photoelectrons while temporarily blocking the sample arm. This is a new interpretation of the commonly known formula stated above. A rule of thumb can be derived from it to dimension the detection part of an OCT system for a certain minimum sensitivity. In Chap. 5, it will be used to determine the number of photogenerated charges the smart pixel must be able to handle without signal saturation. By increasing the optical power of the illumination source and simultaneously decreasing the reflection coefficient in the reference arm, the sensitivity can be increased without increasing the number of photoelectrons.

The sensitivity S of a shot-noise limited OCT system given by Eq. 2.25 is proportional to the optical power illuminating the sample, inversely proportional to the noise equivalent bandwidth NEB , respectively proportional to the integration time per sample T . Therefore it is inversely proportional to the scan speed and image acquisition rate as well as inversely proportional to the illumination spectrum width, e.g. there is a system trade-off between illumination power, sensitivity, axial resolution, sample volume, and image acquisition speed. For biomedical applications, e.g. ophthalmology, sensitivities of 100 dB and more are required [15].

2.2.3 Noise sources

For the SNR analysis only photonic shot noise has been taken into account. In order to exploit the physical limit of the detection principle, it is a requirement for the sensor and the signal processing electronics to exhibit a total noise comprising thermal, flicker, electronic shot*, and quantification noise that should be smaller, in total, than the photocharge shot noise.

Another important noise source is the relative intensity noise (RIN). It includes all fluctuations in the amplitude of the optical signal on the sensor. It is mainly due to the illumination source but also mechanical motion of optical fixtures may cause it. Balanced detection can be used to eliminate it [16,17]. Broadband illumination sources such as Kerr lens mode-locked femtosecond lasers and superluminescent diodes feature a larger mean-squared photodetector current fluctuation than single mode lasers due to the photon bunching in the Bose-Einstein distribution [18–21]. This so-called excess noise not only depends on the mean number of photons but also on the relation between the integration time of the photodetector T and the coherence time τ_c . Still

* This shot noise is not due to the photogenerated charges but is generated by other currents in the electronic circuit.

assuming photon noise limited detection, the OCT SNR becomes

$$SNR \simeq \frac{\eta P_{sc}}{h\nu \cdot NEB} \cdot \frac{1}{1 + \frac{1+\Pi^2}{2} \cdot \frac{\eta P_r \tau_c}{h\nu}}, \quad (2.26)$$

where Π is the degree of polarization. The first multiplicand is the OCT SNR calculated by assuming a Poisson distribution (Eq. 2.24), the second is the correction term due to the excess noise. For a large reference power in a fast scanning system, this correction term can be limiting the system SNR , and therefore the reference power must be reduced to maximize the SNR [13, 14]. In parallel OCT, similarly to other multichannel detection systems [22], the integration time is large and therefore the optical power per pixel is comparatively small. In our case the loss due to this additional noise is much below 1 dB and has therefore been neglected for all further calculations.

2.3 Phase detection

The phase of the interferometric signal carries an even more precise depth information as can be derived from Eq. 2.11c. By detecting the phase difference between two laterally adjacent reflection sites, their relative depth position modulo half the center wavelength is determined. By unwrapping the phase, continuous interfaces with moderate slopes can thus be detected with resolutions down to 0.1 nm [11].

Systems with two detectors measure the phase difference of e.g. the light portions of two polarization axes, so-called polarization-sensitive (PS-) OCT. This allows the detection of Stokes vectors and therefore the acquisition of three-dimensional images of the local birefringence of the sample [23, 24].

2.4 Lateral resolution and depth range

The transverse resolution Δx of an OCT system is determined by the diffraction limited focusing of the imaging system like in a conventional microscope [25, 26] and depends on the numerical aperture $NA = n \cdot \sin(\theta)$, where n is the refractive index and θ signifies the half acceptance angle. In the case of fixed sample imaging optics, the depth range of the system Z corresponding to the depth of focus depends also on the NA .

They are given as

$$\Delta x = 1.22 \cdot \frac{\lambda}{2 \cdot NA} \simeq 0.48 \cdot \sqrt{Z \cdot \lambda}, \quad (2.27)$$

$$Z = \frac{\pi \lambda}{2 \cdot NA^2} \simeq 4.22 \cdot \frac{(\Delta x)^2}{\lambda}. \quad (2.28)$$

In order to expand the depth range of a TD-OCT system, as well as to increase its lateral resolution, concepts with dynamically focussing optics have been developed [27]. For topography imaging, the sample arm focussing optics is moving synchronously with the reference mirror, its speed matching the speed of the reference mirror. But for tomography imaging, a ratio of two between the reference mirror path-length change and the imaging optics position change compensates better for sample refractive indices close to $n = \sqrt{2} \simeq 1.4$, which is the case for many soft biomedical tissues [28].

Dynamically focussing by applying a depth scan movement to the probe imaging system is usually not possible for high-speed OCT imaging except if the parallel approach is chosen as in the context of this work.

2.5 Frequency domain OCT

Recently frequency domain (FD-) OCT principles, alternatively referred to as spectral domain (SD-) OCT, have gained a lot of attention due to their high sensitivity even at low illumination powers. Instead of mechanically scanning the optical delay between the sample and the reference path as in the presented TD-OCT, the optical spectrum of the detected signal is analyzed. The depth profile is then generated by means of Fourier transformation.

Spectrum analysis can either be done sequentially, e.g. by changing the center wavelength of a monochromatic tunable laser, which is referred to as swept source (SS-) OCT, or simultaneously for example by means of a broadband illumination source, a grating, and a CCD or CMOS line sensor, usually called Fourier-domain OCT.

FD-OCT offers an advantage in sensitivity compared to TD-OCT, especially for low-light applications [21, 29]. This will be discussed in more details in Chap. 4.

Bibliography

- [1] B. Karamata, P. Lambelet, M. Laubscher, R. P. Salathé, and T. Lasser, "Spatially incoherent illumination as a mechanism for cross-talk suppression in wide-field optical coherence tomography," *Opt. Lett.*, vol. 29, pp. 736–738, Apr. 2004.
- [2] B. Karamata, M. Laubscher, M. Leutenegger, S. Bourquin, T. Lasser, and P. Lambelet, "Multiple scattering in optical coherence tomography. I. Investigation and modeling," *J. Opt. Soc. Am. A*, vol. 22, pp. 1369–1379, July 2005.
- [3] B. Karamata, M. Leutenegger, M. Laubscher, S. Bourquin, T. Lasser, and P. Lambelet, "Multiple scattering in optical coherence tomography. II. Experimental and theoretical investigation of cross talk in wide-field optical coherence tomography," *J. Opt. Soc. Am. A*, vol. 22, pp. 1380–1388, July 2005.
- [4] W. Drexler, U. Morgener, F. X. Kärtner, C. Pitris, S. A. Boppart, X. D. Li, E. P. Ippen, and J. G. Fujimoto, "In-vivo ultrahigh-resolution optical coherence tomography," *Opt. Lett.*, vol. 24, pp. 1221–1223, 1999.
- [5] A. F. Fercher, C. K. Hitzenberger, M. Sticker, E. Moreno-Barriuso, R. Leitgeb, W. Drexler, and H. Sattmann, "A thermal light source technique for optical coherence tomography," *Opt. Commun.*, vol. 185, pp. 57–64, Nov. 2000.
- [6] L. Vabre, A. Dubois, and A. C. Boccara, "Thermal-light full-field optical coherence tomography," *Opt. Lett.*, vol. 27, pp. 530–532, Apr. 2002.
- [7] B. Povazay, K. Bizheva, A. Unterhuber, B. Hermann, H. Sattmann, A. F. Fercher, W. Drexler, A. Apolonski, W. J. Wadsworth, J. C. Knight, P. S. J. Russell, M. Vetterlein, and E. Scherzer, "Submicrometer axial resolution optical coherence tomography," *Opt. Lett.*, vol. 27, pp. 1800–1802, 2002.
- [8] B. E. A. Saleh and M. C. Teich, *Fundamentals of Photonics*, ch. 17.5. New York: John Wiley & Sons Inc, 1991.
- [9] B. E. A. Saleh and M. C. Teich, *Fundamentals of Photonics*, ch. 11.2. New York: John Wiley & Sons Inc, 1991.
- [10] E. A. Swanson, D. Huang, M. R. Hee, J. G. Fujimoto, C. P. Lin, and C. A. Puliafito, "High-speed optical coherence domain reflectometry," *Opt. Lett.*, vol. 17, pp. 151–153, Jan. 1992.
- [11] B. E. Bouma and G. J. Tearney, *Handbook of Optical Coherence Tomography*. New York: Marcel Dekker Inc, 2002.
- [12] T. Dresel, G. Häusler, and H. Venzke, "Three-dimensional sensing of rough surfaces by coherence radar," *Appl. Opt.*, vol. 31, pp. 919–925, Mar. 1992.
- [13] W. V. Sorin and D. M. Baine, "A Simple Intensity Noise Reduction Technique for Optical Low-Coherence Reflectometry," *IEEE Photonics Techn. Lett.*, vol. 4, pp. 1404–1406, Dec. 1992.
- [14] B. M. Hoeling, A. D. Fernandez, R. C. Haskell, E. Huang, W. R. Myers, D. Petersen, S. E. Ungersma, R. Wang, M. E. Williams, and S. E. Fraser, "An optical coherence microscope for 3-dimensional imaging in developmental biology," *Opt. Express*,

- vol. 6, pp. 136–145, Mar. 2000.
- [15] D. Huang, E. A. Swanson, C. P. Lin, J. S. Schuman, W. G. Stinson, W. Chang, M. R. Hee, T. Flotte, K. Gregory, C. A. Puliafito, and J. G. Fujimoto, “Optical coherence tomography,” *Science*, vol. 254, pp. 1178–1181, 1991.
- [16] M. R. Hee, J. A. Izatt, J. M. Jacobson, J. G. Fujimoto, and E. A. Swanson, “Femtosecond transillumination optical coherence tomography,” *Opt. Lett.*, vol. 18, pp. 950–952, June 1993.
- [17] G. J. Tearney, B. E. Bouma, S. A. Boppart, B. Golubovic, E. A. Swanson, and J. G. Fujimoto, “Rapid acquisition of *in vivo* biological images by use of optical coherence tomography,” *Opt. Lett.*, vol. 21, pp. 1408–1410, Sept. 1996.
- [18] K. Takada, “Noise in optical low-coherence reflectometry,” *IEEE J. Quantum Electron*, vol. 34, pp. 1098–1108, 1998.
- [19] A. G. Podoleanu, “Unbalanced versus balanced operation in an optical coherence tomography system,” *Appl. Opt.*, vol. 39, pp. 173–182, Jan. 2000.
- [20] C. C. Rosa and A. G. Podoleanu, “Signal-to-noise ratio in balanced OCT under wideband illumination,” in *Optical Methods for Tumor Treatment and Detection: Mechanisms and Techniques in Photodynamic Therapy XIV* (D. Kessel, ed.), vol. 5690 of *Proc. SPIE*, pp. 365–371, Apr. 2005.
- [21] R. A. Leitgeb, C. K. Hitzenberger, and A. F. Fercher, “Performance of fourier domain vs. time domain optical coherence tomography,” *Opt. Express*, vol. 11, pp. 889–894, Mar. 2003.
- [22] R. A. Leitgeb, W. Drexler, A. Unterhuber, B. Hermann, T. Bajraszewski, T. Le, A. Stingl, and A. F. Fercher, “Ultrahigh resolution Fourier domain optical coherence tomography,” *Opt. Express*, vol. 12, pp. 2156–2165, May 2004.
- [23] M. R. Hee, D. Huang, E. A. Swanson, and J. G. Fujimoto, “Polarization-sensitive low-coherence reflectometer for birefringence characterization and ranging,” *J. Opt. Soc. Am. B*, vol. 9, pp. 903–908, June 1992.
- [24] H. Ren, Z. Ding, Y. Zhao, J. Miao, J. S. Nelson, and Z. Chen, “Phase-resolved functional optical coherence tomography: simultaneous imaging of *in situ* tissue structure, blood flow velocity, standard deviation, birefringence, and Stokes vectors in human skin,” *Opt. Lett.*, vol. 27, pp. 1702–1704, Oct. 2002.
- [25] J. A. Izatt, M. D. Kulkarni, Hsing-Wen Wang, K. Kobayashi, and M. V. Sivak Jr., “Optical coherence tomography and microscopy in gastrointestinal tissues,” *IEEE Journal of Selected Topics in Quantum Electronics*, vol. 2, pp. 1017–1028, Dec. 1996.
- [26] J. G. Fujimoto, “Optical coherence tomography,” in *Encyclopedia of Optical Engineering* (R. G. Driggers, ed.), New York: Marcel Dekker Inc, Sept. 2003.
- [27] F. Lexter, C. K. Hitzenberger, W. Drexler, S. Molebny, H. Sattmann, M. Sticker, and A. F. Fercher, “Dynamic coherent focus OCT with depth-independent transversal resolution,” *Journal of Modern Optics*, vol. 46, pp. 541–553, Mar. 1999.
- [28] J. M. Schmitt, S. L. Lee, and K. M. Yung, “An optical coherence microscope

with enhanced resolving power in thick tissue," *Optics Communications*, vol. 142, pp. 203–207, Feb. 1997.

- [29] M. A. Choma, M. V. Sarunic, C. Yang, and J. A. Izatt, "Sensitivity advantage of swept source and Fourier domain optical coherence tomography," *Opt. Express*, vol. 11, pp. 2183–2189, May 2003.

Chapter 3

State of the art parallel OCT

3.1 Introduction

Most TD-OCT systems are based on fiber-optic interferometers with a fast axial scanning unit as optical delay line (ODL) and a slow translation unit for the lateral scanning of the sample [1, 2]. Consecutively acquired one-dimensional depth scans are eventually combined to a section or volume image. For high-speed cross-sectional imaging, depth scan speeds up to 175 m/s have been achieved [3]. Fast ODLs are very complex and delicate electro-mechanical systems [4–6], and their performance is a key factor limiting the acquisition speed of the sequential time-domain OCT systems. In contrast, parallel or full-field OCT (pOCT) systems are based on free-space interferometers with a one- or two-dimensional image sensor first explored by Dresel *et al.* [7]. This allows the simultaneous detection of a multitude of measurement spots and obviates completely the need for lateral scanning, reducing the system complexity and cost.

In a pOCT system that features the same number of volume frames per second as a similar sequential OCT system, the speed of the axial scanning unit, compared to the sequential system, is reduced by a factor equivalent to the number of parallel pixels. This can amount to several ten thousand and hence a speed reduction by a more than four orders of magnitude. Or, on the other hand, by increasing this low scan speed, high-speed pOCT imaging can be achieved.

3.2 Full-field optical coherence microscopy

Optical coherence microscopy (OCM) [8, 9] is a variant of OCT that exploits high numerical aperture (NA) objectives and lateral scanning instead of depth scanning in order to provide high-resolution *en face* cross-sectional imaging (compare Sec. 2.4). Full-field OCM [10] is a technique situated in between OCM and pOCT: As in pOCT, a free-space interferometer is used and a two-dimensional image sensor, usually a high-dynamic range CCD camera. But in contrast to pOCT, the reference path is not scanned during the acquisition of one head-on slice, allowing the use of immersion objectives to further increase the NA and reduce the very strong reflection at the sample surface that may saturate the detection device. For volume imaging the sample is stepped to the next depth position after every slice acquisition. The high resolution and sensitivity is traded in for a long 3D acquisition time. The power reflection coefficients proportional to the absolute square of the optical signal autocorrelation are extracted by lock-in detection, i.e. the phase shift between the signals of the two interferometer arms is modulated at a certain frequency f_0 during the *en face* slice acquisition, for example by a periodic change of the reference arm length [11–13]. By amplitude demodulating of the measured intensity, the large signal background is filtered off as well as noise sources at other frequencies than the modulation frequency such as e.g. the temporal drift of the illumination power.

The frame rate of the two-dimensional detection device usually limits the lock-in detection frequency. This is overcome by applying the so-called multiplexed lock-in detection principle [10, 14, 15]: Instead of multiplying the detected signal with a signal of the same frequency, a second modulation in the experimental set-up is used, e.g. an illumination source intensity modulation. By synchronizing the two modulations and using the CCD camera integration time as low-pass filter, an *en face* slice can be detected with only four camera frames. It is also possible to obtain the phase relation with these four measurements improving the depth sensitivity of surface and interface detection to as precise as 0.1 nm [16]. By employing two cameras, the multiplexed lock-in detection can also be applied to pOCT [17].

3.3 Illumination of pOCT systems

In scanning OCT, the detected signal originates from a very confined sample area, which is not the case for pOCT. Therefore tomographic imaging with pOCT with spatially coherent broadband light sources such as Kerr lens mode-locked femtosecond lasers and superluminescent diodes suffers from coherent crosstalk degrading the image quality [18]. Using spatially incoherent light sources such as thermal light sources

[11, 19–21] or illumination source arrays [22], suppresses this crosstalk significantly [23–26].

The disadvantage of thermal light sources is their smaller optical radiance compared to the above mentioned coherent sources, leading to a reduced sensitivity. Although the radiance is smaller, thanks to the multichannel detection principle of pOCT, a larger area can be illuminated and imaged simultaneously, increasing the total optical power per pixel, thus partially overcoming the disadvantage. Still, the limited fillfactor of the detector pixels demands an even higher illumination power.

3.4 Smart pixel detectors for pOCT

3.4.1 Limitations of standard CCD and CMOS APS image sensors

Although one- or two-dimensional signal detectors are required for pOCT, real-time tomographic imaging with conventional cameras such as CCD or CMOS APS image sensors suffers from two sensor inherent limitations: limited dynamic range and limited frame rate.

The optical signal features a modulation with a small contrast, e.g. the modulation amplitude can be several decades smaller than the slowly varying signal offset. This is not only due to the high optical reference path power but also to the ratio between the power reflection coefficient of the coherently detected interface and the total power reflection coefficient of the sample (compare Eq. 2.12). To avoid saturation of conventional image sensors, the illumination level and time must therefore be limited. High dynamic range imagers such as logarithmic [27] or linear-logarithmic [28] response pixel sensors may avoid sensor saturation but decrease the signal conversion gain at high illumination levels. Furthermore their shot-noise limited *SNR* becomes difficult to control since the integration bandwidth depends on the generated photocurrent, as will be described in Sec. 5.2.3 in more details.

So-called smart-pixel architectures that are rarely offered commercially, significantly reduce saturation avoidance without compromising the conversion gain. Architectures with in-pixel current sources allowing to compensate for a large constant part of the photocurrent have been presented e.g. as externally programmable device by Vietz and Seitz [29] or as self-adjusting circuit by Pain and Fossum [30]. Besides an intrinsic loss of 3 dB, as described in detail in Sec. 5.2.3, they have shown to achieve almost photonic shot-noise limited performance.

Real-time pOCT imaging with a volumetric frame rate of a several Hertz to a few ten

Hertz implies optical signals with Doppler modulation frequencies of typically several tens of kHz. For lock-in detection, the imager frame rate should be a triple, a quadruple, or a higher multiple of the modulation frequency [7,31–33] implying hundreds of kHz. This limit is rarely reached, even by the fastest CCD and CMOS line sensors [34–40], not to mention two-dimensional array sensors. The above mentioned multiplexed lock-in detection principle, while working well for OCM, cannot be applied to real-time pOCT, where a depth scan is made within some milliseconds, since they require three or four repetitive measurements with a predetermined phase relation; otherwise the detected envelope becomes dependent on the phase delay between Doppler and illumination modulation frequency [41]. Only a custom design smart pixel architecture with a lock-in or signal demodulation circuit at the pixel level can reduce the required external frame-rate to values that are implementable in an image sensor and suitable readout electronics with reasonable complexity.

3.4.2 POCT smart pixels with product demodulation using a rectifier

Bourquin is, to our knowledge, the first and until this work the only one having developed one- and two-dimensional smart pixel sensors dedicated to pOCT [42–44]. Besides a photon sensing stage such as a reversed biased photodiode and a signal read-out stage, a signal demodulation circuit is implemented at the pixel level. The chosen demodulation principle is based on product demodulation with a rectifying diode, which is described in Sec. 5.2.2 in more detail. This demodulation principle requires bandpass filtering with large time constants, to be realized on a small available pixel area. Therefore NMOS transistors in the linear region are used as resistors. Their advantages of small size and programmable resistor value is compensated by strong non-linear behavior for large signals. A pOCT area smart pixel sensor has been developed with a resolution of 58×58 pixel of $110 \mu\text{m} \times 110 \mu\text{m}$ each and a fillfactor of 10%. The layout was made in a CMOS process with $2 \mu\text{m}$ feature size, double poly, and two metals.

In a setup acquiring volumes of $210 \mu\text{m} \times 210 \mu\text{m} \times 80 \mu\text{m}$ at a 3D frame rate of 25 Hz, this first-generation pOCT sensor has shown a maximum sensitivity of 76 dB [45]. As illumination source a mode-locked Ti:Sapphire femtosecond laser has been used featuring a total sample illumination of 120 mW and a longitudinal response of $3 \mu\text{m}$ in air. The reference path optical power has been attenuated to avoid saturation of the sensor and to increase the demodulation pixel's constant illumination level dependent AC gain. A shot-noise limited OCT system with optimum bandpass filter width would feature 92 dB with the available optical energy per voxel on the photodiode [4]. But the achieved sensitivity is almost shot-noise limited performance for the sensor's filter bandwidth, which is only tunable in a certain range.

This sensor lacks two desirable features: grey-level or intensity imaging is not possible and the phase of the interferometric signal can not be determined. It also suffers from thermal and temporal drift problems, component mismatch, leading to a large photo-response non-uniformity, and a limited range of demodulation and low-pass frequencies. A versatile sensor with an intensity imaging mode, i.e. conventional imaging like a CCD camera, simplifies aligning a set-up in the lab and probe handling, and may even obviate the need for a second camera in a commercial OCT system.

The possibility to detect the phase of the carrier of the interferogram opens up new possibilities in pOCT such as e.g. flow velocity measurements [46] or polarization-sensitive OCT for e.g. birefringence detection [47]. It might also be used to increase depth accuracy, especially for topography measurements [16].

3.5 Conclusion

Parallel optical coherence tomography is a time-domain OCT variant featuring good performance and reduced system complexity. Special care must be taken with the illumination source in order to avoid system performance degrading by optical cross-talk for tomographic imaging, e.g. spatially incoherent illumination sources must be employed.

Real-time imaging of one *en face* depth slice in OCM can be achieved with conventional image sensors and an appropriate synchronous illumination scheme, whereas real-time volumetric imaging with pOCT requires custom designed dedicated smart pixel sensors. A first generation of pOCT smart imagers was developed by Bourquin [44]. The continuously decreasing feature sizes of commercially available CMOS processes allows the reduction of the smart pixel size enabling large pixel array imagers, the improvement of the architecture robustness, and the introduction of additional features such as an intensity imaging mode or carrier phase detection.

Bibliography

- [1] J. M. Schmitt, "Optical coherence tomography (OCT): A review," *IEEE J. Quantum Electron.*, vol. 5, pp. 1205–1215, 1999.
- [2] J. G. Fujimoto, "Optical coherence tomography," in *Encyclopedia of Optical Engineering* (R. G. Driggers, ed.), New York: Marcel Dekker Inc, Sept. 2003.
- [3] J. Szydlo, N. Delachenal, R. Giannotti, R. Wälti, H. Bleuler, and R. P. Salathé, "Air-turbine driven optical low-coherence reflectometry at 28.6 kHz scan repetition rate," *Opt. Commun.*, vol. 154, pp. 1–4, 1998.

- [4] E. A. Swanson, D. Huang, M. R. Hee, J. G. Fujimoto, C. P. Lin, and C. A. Puliafito, "High-speed optical coherence domain reflectometry," *Opt. Lett.*, vol. 17, pp. 151–153, Jan. 1992.
- [5] G. J. Tearney, B. E. Bouma, S. A. Boppart, B. Golubovic, E. A. Swanson, and J. G. Fujimoto, "Rapid acquisition of *in vivo* biological images by use of optical coherence tomography," *Opt. Lett.*, vol. 21, pp. 1408–1410, Sept. 1996.
- [6] G. J. Tearney, B. E. Bouma, and J. G. Fujimoto, "High-speed phase- and group-delay scanning with a grating-based phase control delay line," *Opt. Lett.*, vol. 22, pp. 1811–1813, Dec. 1997.
- [7] T. Dresel, G. Häusler, and H. Venzke, "Three-dimensional sensing of rough surfaces by coherence radar," *Appl. Opt.*, vol. 31, pp. 919–925, Mar. 1992.
- [8] J. A. Izatt, M. R. Hee, G. M. Owen, E. A. Swanson, and J. G. Fujimoto, "Optical coherence microscopy in scattering media," *Opt. Lett.*, vol. 19, pp. 590–592, Apr. 1994.
- [9] J. A. Izatt, M. D. Kulkarni, Hsing-Wen Wang, K. Kobayashi, and M. V. Sivak Jr., "Optical coherence tomography and microscopy in gastrointestinal tissues," *IEEE Journal of Selected Topics in Quantum Electronics*, vol. 2, pp. 1017–1028, Dec. 1996.
- [10] E. Beaurepaire, A. C. Boccara, M. Lebec, L. Blanchot, and H. Saint-Jalmes, "Full-field optical coherence microscopy," *Opt. Lett.*, vol. 23, pp. 244–246, Feb. 1998.
- [11] L. Vabre, A. Dubois, and A. C. Boccara, "Thermal-light full-field optical coherence tomography," *Opt. Lett.*, vol. 27, pp. 530–532, Apr. 2002.
- [12] E. Abraham, E. Bordenave, N. Tsurumachi, G. Jonusauskas, J. Oberlé, C. Rullière, and A. Mito, "Real-time two-dimensional imaging in scattering media by use of a femtosecond Cr 4+ forsterite laser," *Opt. Lett.*, vol. 25, pp. 929–931, June 2000.
- [13] C. W. Dunsby, Y. Gu, and P. M. W. French, "Single-shot phase-stepped wide-field coherence-gated imaging," *Opt. Express*, vol. 11, pp. 105–115, Jan. 2003.
- [14] L. Blanchot, M. Lebec, E. Beaurepaire, P. Gleyzes, A. C. Boccara, and H. Saint-Jalmes, "Low-coherence in-depth microscopy for biological tissue imaging: design of a real-time control system," in *Photon Propagation in Tissues III* (D. A. Benaron, B. Chance, and M. Ferrari, eds.), vol. 3194 of *Proc. SPIE*, pp. 198–204, Dec. 1997.
- [15] P. Gleyzes, A. C. Boccara, and H. Saint-Jalmes, "Multichannel Nomarski microscope with polarization modulation: performance and applications," *Opt. Lett.*, vol. 22, pp. 1529–1531, Oct. 1997.
- [16] B. E. Bouma and G. J. Tearney, *Handbook of Optical Coherence Tomography*. New York: Marcel Dekker Inc, 2002.
- [17] M. Akiba, K. P. Chan, and N. Tanno, "Full-field optical coherence tomography by two-dimensional heterodyne detection with a pair of CCD cameras," *Opt. Lett.*, vol. 28, pp. 816–818, May 2003.
- [18] T. Anhut, B. Karamata, T. Lasser, M. G. Raymer, and L. Wenke, "Measurement of

- scattered light Wigner functions by phase space tomography and implications for parallel OCT," in *Coherence Domain Optical Methods and Optical Coherence Tomography in Biomedicine VII* (V. V. Tuchin, J. A. Izatt, and J. G. Fujimoto, eds.), vol. 4956 of *Proc. SPIE*, pp. 120–128, July 2003.
- [19] A. F. Fercher, C. K. Hitzenberger, M. Sticker, E. Moreno-Barriuso, R. Leitgeb, W. Drexler, and H. Sattmann, "A thermal light source technique for optical coherence tomography," *Opt. Commun.*, vol. 185, pp. 57–64, Nov. 2000.
- [20] A. F. Fercher, C. K. Hitzenberger, E. M. Moreno-Barriuso, M. Sticker, R. Leitgeb, and H. Sattmann, "Optical coherence tomography technique for thermal light sources," in *Photon Migration, Diffuse Spectroscopy, and Optical Coherence Tomography: Imaging and Functional Assessment* (S. Andersson-Engels and J. G. Fujimoto, eds.), vol. 4160 of *Proc. SPIE*, pp. 63–68, Nov. 2000.
- [21] B. Laude, A. De Martino, B. Drevillon, L. Benattar, and L. Schwartz, "Full-field optical coherence tomography with thermal light," *Appl. Opt.*, vol. 41, pp. 6637–6645, Nov. 2002.
- [22] S. Bourquin, L. Laversenne, S. Rivier, T. Lasser, R.-P. Salathe, M. Pollnau, C. Grivas, D. P. Shepherd, and R. W. Eason, "Parallel broadband fluorescent light source for optical coherence tomography," in *Coherence Domain Optical Methods and Optical Coherence Tomography in Biomedicine IX* (D. Kessel, ed.), vol. 5690 of *Proc. SPIE*, pp. 209–213, Apr. 2005.
- [23] B. Karamata, P. Lambelet, M. Laubscher, R. P. Salathé, and T. Lasser, "Spatially incoherent illumination as a mechanism for cross-talk suppression in wide-field optical coherence tomography," *Opt. Lett.*, vol. 29, pp. 736–738, Apr. 2004.
- [24] B. Karamata, *Multiple scattering in wide-field optical coherence tomography*. PhD thesis, École Polytechnique Fédérale de Lausanne, 2004.
- [25] B. Karamata, M. Laubscher, M. Leutenegger, S. Bourquin, T. Lasser, and P. Lambelet, "Multiple scattering in optical coherence tomography. I. Investigation and modeling," *J. Opt. Soc. Am. A*, vol. 22, pp. 1369–1379, July 2005.
- [26] B. Karamata, M. Leutenegger, M. Laubscher, S. Bourquin, T. Lasser, and P. Lambelet, "Multiple scattering in optical coherence tomography. II. Experimental and theoretical investigation of cross talk in wide-field optical coherence tomography," *J. Opt. Soc. Am. A*, vol. 22, pp. 1380–1388, July 2005.
- [27] S. G. Chamberlain and J. P. Y. Lee, "A novel wide dynamic range silicon photodetector and linear imaging array," *IEEE J. Solid-State Circ.*, vol. 19, pp. 41–48, Feb. 1984.
- [28] M. Willemin, N. Blanc, G. K. Lang, S. Lauxtermann, P. Schwider, P. Seitz, and M. Wány, "Optical characterization methods for solid-state image sensors," *Optics and Laser in Engineering*, vol. 36, pp. 185–194, 2001.
- [29] O. Vietze and P. Seitz, "Image sensing with programmable offset pixels for increased dynamic range of more than 150 dB," in *Solid State Sensor Arrays and CCD Cameras* (C. N. Anagnostopoulos, M. M. Blouke, and M. P. Lesser, eds.), vol. 2654

- of *Proc. SPIE*, pp. 93–98, Mar. 1996.
- [30] B. Pain and E. R. Fossum, “A Current Memory Cell With Switch Feedthrough Reduction By Error Feedback,” *IEEE J. Solid-State Circ.*, vol. 29, pp. 1288–1290, Oct. 1994.
- [31] K. G. Larkin, “Efficient nonlinear algorithm for envelope detection in white light interferometry,” *J. Opt. Soc. Am. A*, vol. 13, pp. 832–843, Apr. 1996.
- [32] S. S. C. Chim and G. S. Kino, “Three-dimensional image realization in interference microscopy,” *Appl. Opt.*, vol. 31, pp. 2550–2553, May 1992.
- [33] M. D. Kulkarni and J. A. Izatt, “Digital signal processing in optical coherence tomography,” in *Coherence Domain Optical Methods in Biomedical Science and Clinical Applications* (V. V. Tuchin, H. Podbielska, and B. Ovrzyn, eds.), vol. 2981 of *Proc. SPIE*, pp. 2–6, May 1997.
- [34] M. Lehmann, L. Cavalier, S. Lauxtermann, M. Richter, F. Lustenberger, N. Blanc, and P. Seitz, “High-speed photo line sensors,” in *Proceedings of the workshop on charge-coupled devices and advanced image sensors* (E. Fossum, A. Theuwissen, and N. Teranishi, eds.), (Elmau, Germany), 2003.
- [35] M. Lehmann, L. Cavalier, S. Lauxtermann, M. Richter, F. Lustenberger, N. Blanc, and P. Seitz, “A 2x2k photo line sensor for high-speed applications,” *Optics and Lasers in Engineering*, vol. 43, pp. 349–364, Mar. 2005.
- [36] B. Fowler, J. Balicki, D. How, S. Mims, J. Canfield, and M. Godfrey, “An ultra low noise high speed CMOS linescan sensor for scientific and industrial applications,” in *Proceedings of the workshop on charge-coupled devices and advanced image sensors* (E. Fossum, A. Theuwissen, and N. Teranishi, eds.), (Elmau, Germany), 2003.
- [37] Basler Vision Technologies AG, *L100*, Aug. 2004.
- [38] Dalsa Corp., *IT-P1*, Feb. 2004.
- [39] B. Benwell, O. Nixon, G. Allan, J. Huras, and M. Ledgerwood, “12k 5 μm linescan ccd sensor with 320 MHz data rate,” in *Proceedings of the workshop on charge-coupled devices and advanced image sensors* (E. Fossum, A. Theuwissen, and N. Teranishi, eds.), (Karuiizawa, Nagano, Japan), pp. 189–192, June 2005.
- [40] Dalsa Corp., *Piranha3 P3-8x*, June 2005.
- [41] R. Windecker, M. Fleischer, B. Franzer, and H. J. Tiziani, “Two methods for fast coherence tomography and topometry,” *J. Mod. Optics*, vol. 44, pp. 967–977, 1997.
- [42] S. Bourquin, *Low-coherence Interferometry Based on Customized Detector Arrays*. Thèse de doctorat, Ecole Polytechnique Fédérale de Lausanne, Switzerland, 2000.
- [43] S. Bourquin, V. Monterosso, P. Seitz, and R. P. Salathé, “Video-rate optical low-coherence reflectometry based on a linear smart detector array,” *Opt. Lett.*, vol. 25, pp. 102–104, Jan. 2000.
- [44] S. Bourquin, P. Seitz, and R. P. Salathé, “Optical coherence topography based on a two-dimensional smart detector array,” *Opt. Lett.*, vol. 26, pp. 512–514, Apr. 2001.
- [45] M. Laubscher, M. Ducros, B. Karamata, T. Lasser, and R. Salathe, “Video-rate

- three-dimensional optical coherence tomography," *Opt. Express*, vol. 10, pp. 429–435, May 2002.
- [46] V. X. D. Yang, M. L. Gordon, B. Qi, J. Pekar, S. Lo, E. Seng-Yue, A. Mok, B. C. Wilson, and I. A. Vitkin, "High speed, wide velocity dynamic range Doppler optical coherence tomography (Part I): System design, signal processing, and performance," *Opt. Express*, vol. 11, pp. 794–+, July 2003.
- [47] B. H. Park, M. C. Pierce, B. Cense, and J. F. de Boer, "Real-time multi-functional optical coherence tomography," *Opt. Express*, vol. 11, pp. 782–793, 2003.

Chapter 4

Fundamental physical and technical limitations of pOCT

This chapter describes the limiting factors of pOCT imaging in general but also especially for the chosen smart pixel architecture described in Chap. 5. The maximum SNR performance of frequency-domain (FD-), scanning time-domain (TD-), and time-domain parallel optical coherence tomography (TD-pOCT) are compared.

4.1 SNR and optical power in pOCT

The SNR of an OCT system is proportional to the optical energy on the sample per acquired voxel as derived in Chap. 2. Three factors are limiting this energy: the available power of the illumination source, the maximally allowable optical power on the sample to guarantee eye-safe operation, and the integration time per voxel. In pOCT many measurement points are acquired in parallel, increasing the acquisition time for the same volume acquisition but also dividing the available optical power from the source. It has been claimed that if there is an unlimited illumination source power but the allowable optical intensity on the sample is the limiting factor, parallel detection is favorable because of its multichannel advantage [1]. Unfortunately, high-power broadband illumination sources such as femtosecond lasers are very expensive, and, even worse, feature high spatial coherence, limiting their pOCT use to surface or thin sample imaging due to the optical cross-talk. Illumination sources with low spatial coherence such as LEDs or thermal sources e.g. a mercury gas discharge lamp, feature much smaller radiances and the system normally becomes illumination power

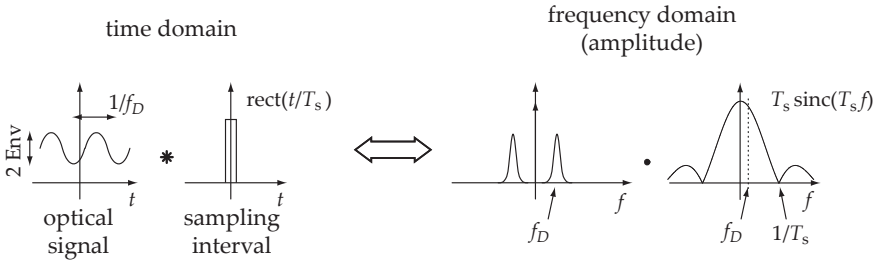


Figure 4.1: Contrast reduction due to the natural sampling: The optical signal composed of a sinusoid of frequency f_D and a Gaussian envelope (not shown) superposed on a constant offset is filtered (convolution) by a rectangular function, in our case with the integration time width $T_s = 1/4f_D$. In the frequency domain, this corresponds to a multiplication of their Fourier transforms. The amplitude of the filtered sinusoid is therefore reduced by a factor $\text{sinc}(1/4) = \sqrt{8}/\pi \simeq 0.90$.

limited. Furthermore, medical illumination safety rules rather state radiant sample exposure (maximum permissible exposure, MPE) instead of irradiance. In this case the multichannel advantage is not applicable either [2].

Scanning OCT systems detect the total optical power at the output of the interferometer. Today’s smart pixels of pOCT systems feature a fillfactor that is usually around 10%. In plane wave illumination, this implies that a large part of the optical power is lost in the detection process. A gain of 2 to 5 can be expected by the use of a microlens array on top of the sensor. It is probable that future smart pixels make use of a thin-film on ASIC (TFA), a hybrid, or a flip-chip technology in order to increase the fillfactor to almost 100%.

4.2 Natural sampling

The smart pixel architecture developed within the scope of this work applies lock-in detection as will be described in Chap. 5. The optical signal converted in a photodiode into a photocurrent is integrated in our case during a quarter period, the so-called natural sampling integration time. This integration reduces the contrast of the modulated signal and therefore the SNR of the detected envelope. Though decreasing the sampling time increases the contrast, it also decreases the SNR because fewer photons are captured and because of their Poisson distribution. A good trade-off has to be found.

The sampling process corresponds to the integration over time of the product of the input signal and a Dirac function, or, in practice, a rectangular function for ideal, re-

spectively natural, sampling. The naturally sampled value therefore corresponds to the convolution of the modulated signal with the rectangular function of the integration time T_{samp} . In the frequency domain, this corresponds to the input signal spectrum multiplication with a sinc function. Fig. 4.1 illustrates this fact. In our case, the input signal is approximated as a sinusoid of frequency f_D and Gaussian envelope superposed to a constant offset. The signal of interest, the component of frequency f_D , is therefore reduced by the factor $\text{sinc}(f_D T_{\text{samp}}) = \sin(\pi \cdot f_D T_{\text{samp}}) / \pi \cdot f_D T_{\text{samp}}$. If the sampling time corresponds to a quarter of the period of the modulated signal, the contrast reduction is the factor $\text{sinc}(1/4) = \sqrt{8}/\pi \simeq 0.90$ or less than 1 dB in SNR. This has been discussed for example by Büttgen [3] in general for a time-of-flight (TOF) smart pixel application or in the case of quarter-period sampling in [4].

By reducing the sampling time, the SNR reduction due to the natural sampling can be reduced. But if the number of samples per period of four is maintained, this is disadvantageous since it reduces the number of acquired photoelectrons and therefore the SNR significantly. A method to achieve better results is to increase the number of samples per period but this is impracticable for smart pixels dedicated to high-speed pOCT. Another solution is a reference arm movement of four steps per period instead of a continuous scanning movement [5]. In this case, the sampled value corresponds to exactly the value of the optical signal at a given time. However, the development of a mechanical mirror translation stage with this propriety able to scan a millimeter range with a speed of several millimeters per second does not look feasible at the time.

4.3 Comparison of the SNR of TD-OCT, TD-pOCT, and FD-OCT

The sensitivity defined as the minimum detectable reflection coefficient is a key factor of every OCT system determining the possible applications. As we have derived in Sec. 2.2, the SNR and therefore the sensitivity is proportional to the available illumination power, reciprocally proportional to the image volume in numbers of lateral pixels and the depth range, and proportional to the 3D image acquisition rate. This relations hold true for any TD-OCT system. When natural sampling over a quarter demodulation period is applied, which is the case in most pOCT systems, the SNR is reduced by less than 1 dB, as calculated in the last section. POCT with image sensors offering a reduced fillfactor suffers from the loss in optical power, the SNR being reduced by just that factor.

Recently FD-OCT principles have gained a lot of attention due to their high sensitivity even at low illumination powers. For this reason, this section compares not only the SNR of time-domain scanning and parallel OCT but takes also the performance of FD-

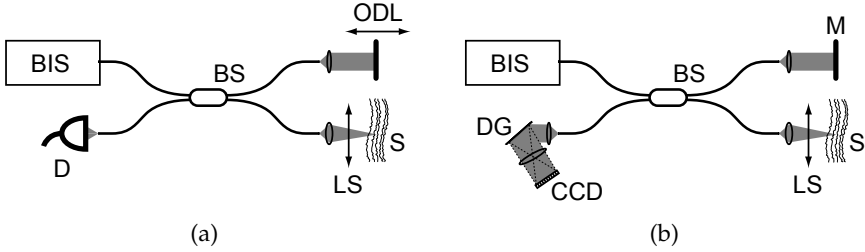


Figure 4.2: Simplified interferometer set-ups for scanning TD-OCT (a) and FD-OCT with a grating (b): both consist of a fiberoptic interferometer with a beam splitter (BS), a broadband illumination source (BIS), and a lateral scanning unit (LS) that moves the focused illumination spot across the sample (S). Furthermore, the TD-OCT system applies reference path length scanning with an optical delay line (ODL) and demodulation of the detected electro-optical signal (D). In the FD-OCT system, the optical wave in the reference path is reflected by a static mirror (M). The spectrum of the signal at the output of the interferometer is analyzed for example with a diffraction grating and a CCD line camera.

OCT into account. Fig. 4.2 compares the basic elements of a scanning TD-OCT system and an FD-OCT system with a diffraction grating.

A general expression of the *SNR* of an FD-OCT system in the shot-noise limited case is given by [6,7]:

$$SNR_{FD-OCT} = \frac{\rho\eta T}{h\nu_0} \gamma_s R_s P_0, \tag{4.1}$$

where ρ is the spectrometer efficiency comprising the diffraction grating efficiency and γ_s is the portion of the illumination source power that reaches the detector after having passed through the sample arm assuming a maximum sample reflectivity e.g. $\gamma_s \leq 1/4$ for a simple Michelson interferometer based set-up. $h\nu_0$ is the photon energy, R_s is the sample reflectivity, and P_0 is the optical power of the illumination source, therefore $P_{sc} = \gamma_s R_s P_0$ is the optical power measured on the detector, while temporarily blocking the reference arm. This equation corresponds exactly to the *SNR* of a TD-OCT system (Eq. 2.24) in the case of reference power adaptation or balanced detection and can also be intuitively explained by the Poisson distribution of the coherently detected light. The only difference to the TD-OCT performance lies in the additional spectrometer efficiency ρ and a significant difference in the meaning of the integration time T . The integration time is now the time that defines a complete A-scan independently of the illumination source spectrum. The light that is scattered back from each interface in the sample contributes to the FD-OCT signal during the entire time of the A-scan,

while in the case of TD-OCT it only contributes information during a time related to noise equivalent bandwidth $T = 1/2 \cdot NEB$ of the filter electronics.

The bandwidth of the TD-OCT filter should be chosen as

$$NEB \simeq 2\Delta f = 2 \cdot \frac{\Delta\lambda}{\lambda_0} f_D = 2 \cdot \frac{\Delta\lambda}{\lambda_0} \cdot \frac{2v_{\text{scan}}}{\lambda_0} \quad (4.2a)$$

$$\geq 4 \cdot \frac{\Delta\lambda}{\lambda_0^2} \cdot f_A \cdot \Delta Z, \quad (4.2b)$$

as recommended by Swanson *et al.* [8]. ΔZ denotes the depth imaging range. The assumption that the scan speed equals the depth range times the A-scan rate is optimistic since usually the duty cycle D of the optical delay line is below 100 %. The TD-OCT integration time therefore becomes

$$T_{\text{TD-OCT}} \simeq \frac{1}{8} \frac{\lambda_0^2}{\Delta\lambda \cdot \Delta Z} \frac{D}{f_A}. \quad (4.3)$$

For TD-pOCT with a smart pixel imager like the one presented in this work, the number of measurement points m taken per FWHM interferogram envelope σ_z , the integration time corresponds to

$$T_{\text{TD-pOCT}} \simeq \frac{\sigma_z/m}{\Delta Z} \frac{D}{f_{3D}}. \quad (4.4)$$

If a sensor with n pixels is used, the system acquires n A-scans simultaneously. Compared to a scanning system, an A-scan therefore takes n times longer. This factor cancels itself in the SNR calculation, since the available optical power must also be distributed onto n spots. Due to the natural sampling described in the section above the SNR of a sampling pOCT system is further reduced by a factor $8/\pi^2 \gtrsim -1$ dB.

The SNR of TD-, TD-p-, and FD-OCT for a given illumination source with a total power P_0 , an A-scan frequency f_A , and a depth range ΔZ is compared in Tab. 4.1.

FD-OCT's ability to acquire the depth information of an A-scan simultaneously within one measurement, not only reduces the number of moving parts of the system compared to scanning TD-OCT, but it is also the reason for its advantage in SNR. It can be concluded that, from a point of view that is just comparing the performance in SNR, FD-OCT is the favorable technique for limited illumination conditions such as high-speed imaging.

Nevertheless, FD-OCT suffers from the lack of dynamically focussing. In TD-OCT systems, it is possible to move the imaging system synchronously with the reference mir-

	TD-OCT	TD-pOCT	FD-OCT
SNR	$\frac{\eta\gamma_s R_s P_0}{h\nu \cdot NEB} = \frac{\eta\gamma_s R_s 2P_0 T}{h\nu}$	$\frac{16}{\pi^2} \cdot \frac{\eta\gamma_s R_s P_0 / nT}{h\nu} \star$	$\frac{\rho\eta\gamma_s R_s P_0 T}{h\nu}$
integration time T	$\frac{1}{8} \frac{\lambda_0^2}{\Delta\lambda \cdot \Delta Z} \frac{D}{f_A}$	$\frac{\sigma_z}{m \cdot \Delta Z} \frac{nD}{f_A}$	$\frac{1}{f_A}$
relative SNR	$\frac{1}{4} \frac{D}{\rho} \frac{\lambda_0^2}{\Delta\lambda \cdot \Delta Z}$	$\frac{16}{\pi^2} \frac{D}{\rho} \frac{\sigma_z}{m \cdot \Delta Z}$	1
relative SNR for typical values [†]	-16.5 dB	-16.7 dB [‡]	0 dB
maximum lateral resolution Δx [§]	14 μm	< a few μm	14 μm

* η comprises also the pixel fillfactor in the case of TD-pOCT.

† The calculated values are based on the following typical parameter values: Depth range $\Delta Z = 1$ mm, optical delay line duty cycle $D = 80\%$, center wavelength $\lambda_0 = 800$ nm, spectrum width (FWHM) $\Delta\lambda = 30$ nm leading to a depth resolution of $\sigma_z = 9.4$ μm , number of pOCT measurement points per envelope (FWHM) $m = 3$, and spectrometer efficiency $\rho = 0.19$.

‡ If a fillfactor of only 10% is assumed in the case of smart pixels without micro-lenses, the relative SNR drops again by 10 dB.

§ To achieve a depth range of 1 mm, the numerical aperture must be $NA \leq 0.035$ for TD-OCT and FD-OCT, where dynamically focussing is impracticable; this leads to a degradation of the lateral resolution.

Table 4.1: Performance comparison of TD-OCT, TD-pOCT, and FD-OCT: Despite the similar expressions, frequency-domain OCT has a significantly increased SNR performance compared to its time-domain variants due to a different meaning of the integration time T . The performance of time-domain scanning and parallel OCT is similar except for the limited fillfactor that degrades the SNR of pOCT.

ror in order to focus on the depth position, where the detected interference originates. For high-speed imaging, this is impractical with a conventional scanning system; although transverse-priority or *en face* scanning might offer a solution [1,9]. The reduced axial scan speed of pOCT allows dynamically focussing even for real-time volumetric imaging.

In Sec. 2.4, the dependance of the lateral resolution and the depth range on the numerical aperture has been described. Without acquisition synchronous focussing, very low-aperture optics has to be used, otherwise the depth range is reduced. If the system with the illumination source of the example in Tab. 4.1, featuring a depth resolution of ~ 10 μm , shall exhibit the same resolution in the lateral direction, the depth range is reduced to about $Z \leq 530$ μm .

Furthermore, the higher the NA is, the more light is received from a reflecting spot. For

topographic imaging, specularly reflecting surfaces can only be detected, if their angle is smaller than the maximum acceptance angle.

Many FD-OCT system implementations suffer from the limitations of CCD line cameras in dynamic range, read-out speed, and resolution. Smart imagers potentially solve these problems in the future.

From the point of system design, pOCT features a reduced set-up complexity, reducing engineering and manufacturing costs, especially in comparison with scanning TD-OCT.

4.4 Performance degradation by modulation frequency mismatch and vibrations

POCT can offer an ideal solution for several industrial applications in the field of high-accuracy metrology and quality control, since it offers surface measurements in real-time. In this section, the influences of typical industrial environments are discussed.

The pOCT approach with a smart pixel imager, presented in this work, faces some challenges in practical situations. The real Doppler frequency and the demodulation frequency never match exactly. This is due to the limited accuracy of the reference path scanner but also due to vibrations experienced by the system. These two effects degrade the maximum performance of the pOCT system.

4.4.1 Scan speed mismatch

The signals in-phase A_I and quadrature A_Q are generated inside every pixel, as will be described in the next chapter. They result from a multiplication of the detected electro-optical signal with a signal of frequency f_d , close to the interferogram Doppler frequency f_D . If the actual scan speed has a constant difference to the theoretically required speed, the detected signal and the demodulation signal have a constant frequency mismatch. Assuming a constant contrast during one measurement $\mathcal{V}(t) \simeq \mathcal{V} \quad \forall t$, which is a correct approximation if the depth sampling Δz is much smaller than the depth resolution σ_z , it can be shown that the demodulated in-phase

and quadrature signals degrade and become

$$\begin{aligned}
 A_I \propto \mathcal{V} \cdot \sum_{n=0}^{N-1} & \left[\sin \left(2\pi \frac{f_D}{f_d} \cdot (n + 1/4) + \Delta\varphi \right) - \sin \left(2\pi \frac{f_D}{f_d} \cdot n + \Delta\varphi \right) \right] \\
 & - \mathcal{V} \cdot \sum_{n=0}^{N-1} \left[\sin \left(2\pi \frac{f_D}{f_d} \cdot (n + 3/4) + \Delta\varphi \right) - \sin \left(2\pi \frac{f_D}{f_d} \cdot (n + 1/2) + \Delta\varphi \right) \right]
 \end{aligned} \tag{4.5a}$$

and

$$\begin{aligned}
 A_Q \propto \mathcal{V} \cdot \sum_{n=0}^{N-1} & \left[\sin \left(2\pi \frac{f_D}{f_d} \cdot (n + 1/2) + \Delta\varphi \right) - \sin \left(2\pi \frac{f_D}{f_d} \cdot (n + 1/4) + \Delta\varphi \right) \right] \\
 & - \mathcal{V} \cdot \sum_{n=0}^{N-1} \left[\sin \left(2\pi \frac{f_D}{f_d} \cdot (n + 1) + \Delta\varphi \right) - \sin \left(2\pi \frac{f_D}{f_d} \cdot (n + 3/4) + \Delta\varphi \right) \right],
 \end{aligned} \tag{4.5b}$$

where N is the number of periods over which the signals are integrated. A_I and A_Q are combined to form the amplitude and the phase as

$$A = \sqrt{A_I^2 + A_Q^2} \tag{4.6}$$

$$P = \arctan \left(\frac{A_I}{A_Q} \right) \tag{4.7}$$

Amplitude and phase have been calculated as function of the percentage mismatch between f_D and f_d , and the phase $\Delta\varphi$. The number of periods, over which the signal was integrated was chosen to be $N = 10$. Fig. 4.3 shows the results. One percent of speed mismatch e.g. of Doppler to demodulation frequency mismatch, gives a loss of about 3% in amplitude and already a phase error of about 18° . A speed mismatch of 5% already reduces the amplitude almost by a factor 2 (6 dB in SNR) and the resulting phase error becomes almost 90° . It is therefore a crucial requirement for smart pixel pOCT to have a high precision scanner to produce images in a reliable manner, where the exact speed mismatch tolerance depends strongly on the targeted performance, as well as whether the phase information is required or not.

4.4.2 POCT under vibrations

Vibrations are not avoidable in a system with moving parts such as our pOCT system. The problem is very similar to the scan speed mismatch problem. Due to the natural

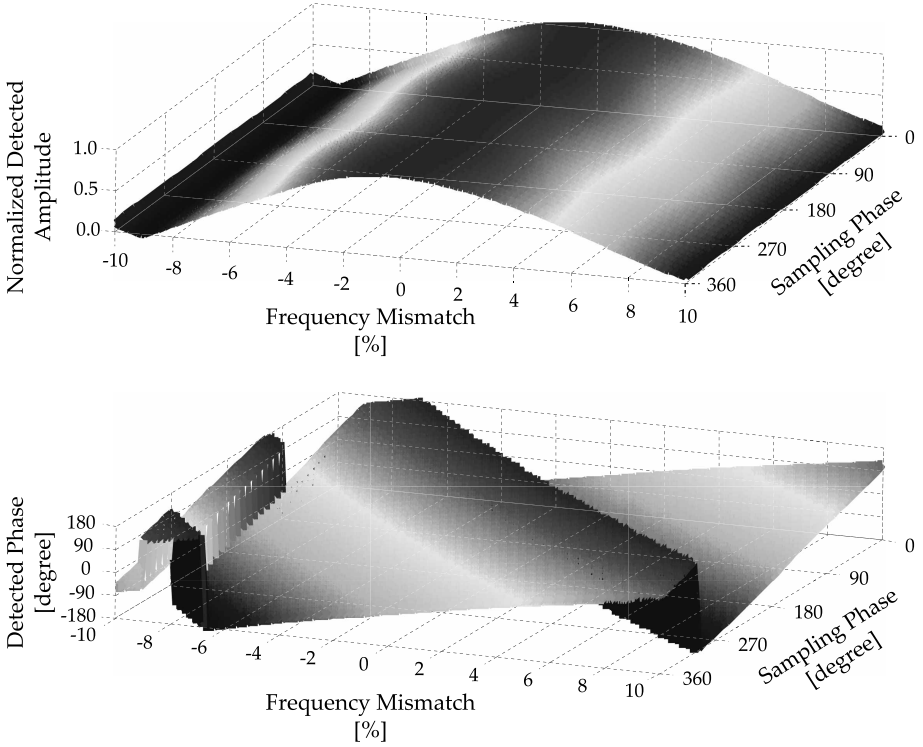


Figure 4.3: Calculated effect of scan speed mismatch, i.e. Doppler to demodulation frequency mismatch, on the detected amplitude and phase: A mismatch of 1% reduces the SNR by about 0.5 dB and gives a phase error of 18° . At 5% speed mismatch, the SNR drops by almost 6 dB and the phase information becomes unusable with an error of almost 90° . ($N = 10$ periods have been taken into account.)

sampling, the optical signal is integrated on the photodiode during a time corresponding to the quarter of a Doppler frequency period. If during this time the optical path difference is changed by more than a period, the signal contrast is destroyed. Vibrations with amplitudes smaller than a quarter period do not significantly degrade the performance. In this section, the problem is numerically analyzed.

If the path difference between reference and sample path Δl at a given time is not only determined by the scan speed v but also influenced by a superposed, sinusoidal vibration, the path difference can be described as

$$\Delta l(t) = v \cdot t + A_{\text{vib}} \cdot \sin(2\pi\nu_{\text{vib}}t + \varphi_{\text{vib}}), \quad (4.8)$$

where A_{vib} , ν_{vib} , and φ_{vib} are amplitude, frequency, and phase of the vibration. It is straightforward to show that the in-phase signal becomes

$$\begin{aligned}
 A_I \propto \mathcal{V} \sum_{n=0}^{N-1} \int_{\frac{n}{f_D}}^{\frac{n+1/4}{f_D}} \cos \left(2\pi f_D t + 2\pi \frac{2A_{\text{vib}}}{\lambda_0} \sin(2\pi \nu_{\text{vib}} t + \varphi_{\text{vib}}) + \Delta\varphi \right) dt \\
 - \mathcal{V} \sum_{n=0}^{N-1} \int_{\frac{n+1/2}{f_D}}^{\frac{n+3/4}{f_D}} \cos \left(2\pi f_D t + 2\pi \frac{2A_{\text{vib}}}{\lambda_0} \sin(2\pi \nu_{\text{vib}} t + \varphi_{\text{vib}}) + \Delta\varphi \right) dt.
 \end{aligned} \tag{4.9}$$

The quadrature signal A_Q is the same except for the integral limits that are shifted by $1/4f_D$.

Fig. 4.4 shows a numerical analysis of the detected amplitude as a function of the vibration frequency ν_{vib} and amplitude A_{vib} for typical smart pixel pOCT imaging values $\lambda_0 = 820 \text{ nm}$ and $v = 20 \text{ mm/s}$, e.g. $f_D \simeq 48.8 \text{ kHz}$. The amplitude's minimum value is displayed in order to suppress the vibration and the sampling phase in the graph. From this graph it can be seen that in order to guarantee a loss of less than 1 dB in SNR (11 % in amplitude), the vibration frequency amplitude product must be less than $1.6\text{E-}4 \text{ Hz} \cdot \text{m} = 160 \mu\text{m/s}$, unless the vibration frequency is less than 80 nm. This signifies that for a vibration peak to peak amplitude of $1 \mu\text{m}$, its frequency must be smaller than 160 Hz, at $10 \mu\text{m}$ the frequency limit goes down to 16 Hz, in order not to suffer from significant loss due to vibrations.

This vibration frequency amplitude product limit is found to be proportional to the the scan speed. The vibration amplitude limit under which the vibration influence is insignificant for any frequency is proportional to the wavelength. Reducing the natural sampling time detains only partially the effect at the cost of loss in optical power. Since the contrast reduction varies in function of the sampling and vibration phase, an additional non-negligible noise is introduced. From this analysis it can be concluded that scanning OCT systems suffer less from vibration-introduced noise due to their higher scan rates. On the other hand it is also true that a pOCT system generates much less vibrations thanks to the reduced scan frequencies and absence of lateral movements. A resonance analysis of the mechanical system, especially of the reference path scanner should be accomplished to prevent unpleasant surprises.

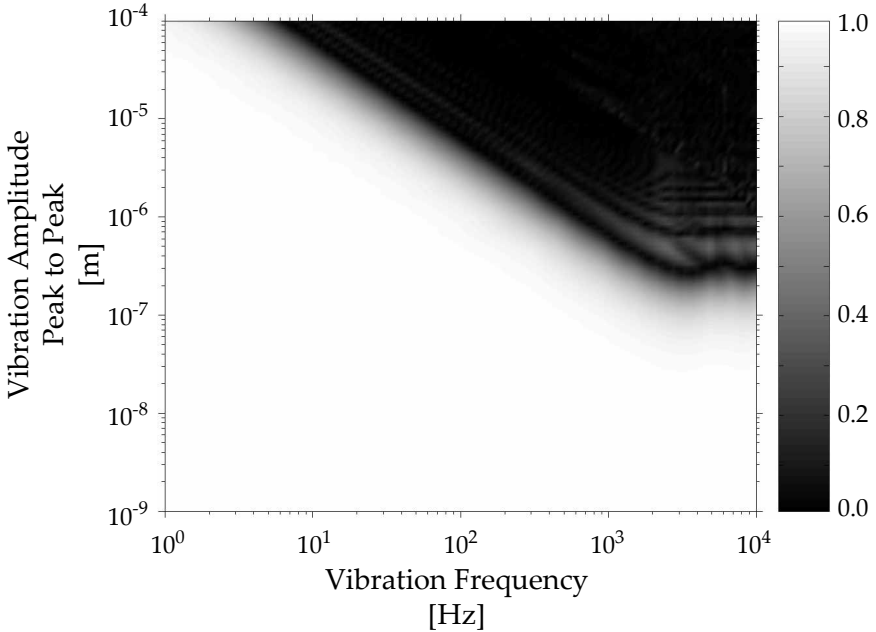


Figure 4.4: Calculated effect of a sinusoidal vibration on the detected amplitude, the minimum normalized amplitude is shown (scan speed $v = 20 \text{ mm/s}$, peak wavelength $\lambda_0 = 820 \text{ nm}$, and number of repetitions $N = 10$). To suffer from less than 1 dB loss, the vibration frequency times the vibration peak to peak amplitude must be smaller than $1.6\text{E-}4 \text{ Hz} \cdot \text{m}$, or the vibration peak to peak amplitude must be smaller than 180 nm.

4.5 Conclusion

The TD-pOCT imaging technique with smart pixels has a significant advantage over pOCT with conventional imagers but also over scanning OCT in terms of speed i.e. in the number of voxels that can be acquired per time interval. As other high-speed TD-OCT systems its SNR suffers because of the reduced optical energy per acquired measurement point [10]. This problem is exacerbated in tomographic imaging due to the need for spatially incoherent illumination sources to avoid optical cross-talk, which in general feature smaller radiances than spatially coherent light sources. The main application fields for pOCT are therefore in the high-speed topographic imaging, where also high-power illumination sources can be used.

Compared to FD- and scanning TD-OCT, pOCT offers also the possibility of dynam-

ically focussing for fast volumetric imaging and thus allows the advantageous use of high NA optics. It is therefore the only one of the three methods suited for high-speed imaging of samples with depth profiles of more than a few hundred micrometer.

Special care must be taken for the scanning system in order to suppress vibrations and speed mismatches to an insignificant level.

Bibliography

- [1] B. E. Bouma and G. J. Tearney, *Handbook of Optical Coherence Tomography*. New York: Marcel Dekker Inc, 2002.
- [2] R. Henderson and K. Schulmeister, *Laser Safety*. Bristol: Institute of Physics Publishing, 2004.
- [3] B. Büttgen, T. Oggier, R. Kaufmann, P. Seitz, and N. Blanc, "Demonstration of a novel drift field pixel structure for the demodulation of modulated light waves with application in three-dimensional image capture," in *Three-Dimensional Image Capture and Applications VI* (B. D. Corner, P. L, and R. P. Pargas, eds.), vol. 5302 of *Proc. SPIE*, pp. 9–20, Apr. 2004.
- [4] S. Beer, P. Zeller, N. Blanc, F. Lustenberger, and P. Seitz, "Smart pixels for real-time optical coherence tomography," in *Three-Dimensional Image Capture and Applications VI* (B. D. Corner, P. Li, and R. P. Pargas, eds.), vol. 5302 of *Proc. SPIE*, pp. 21–32, Apr. 2004.
- [5] K. Creath, "Phase-measurement interferometry techniques," in *Progress in Optics*, vol. XXVI, E. Wolf (Ed.), Elsevier, 1988.
- [6] R. A. Leitgeb, C. K. Hitzenberger, and A. F. Fercher, "Performance of fourier domain vs. time domain optical coherence tomography," *Opt. Express*, vol. 11, pp. 889–894, Mar. 2003.
- [7] M. A. Choma, M. V. Sarunic, C. Yang, and J. A. Izatt, "Sensitivity advantage of swept source and Fourier domain optical coherence tomography," *Opt. Express*, vol. 11, pp. 2183–2189, May 2003.
- [8] E. A. Swanson, D. Huang, M. R. Hee, J. G. Fujimoto, C. P. Lin, and C. A. Puliafito, "High-speed optical coherence domain reflectometry," *Opt. Lett.*, vol. 17, pp. 151–153, Jan. 1992.
- [9] A. G. Podoleanu, J. A. Rogers, D. J. Webb, D. A. Jackson, A. R. Wade, and F. W. Fitzke, "Compatibility of transversal OCT imaging with confocal imaging of the retina in vivo," in *Coherence Domain Optical Methods in Biomedical Science and Clinical Applications III* (V. V. Tuchin and J. A. Izatt, eds.), vol. 3598 of *Proc. SPIE*, pp. 61–67, Apr. 1999.
- [10] J. Szydlo, N. Delachenal, R. Giannotti, R. Wälti, H. Bleuler, and R. P. Salathé, "Air-turbine driven optical low-coherence reflectometry at 28.6 kHz scan repetition

rate," *Opt. Commun.*, vol. 154, pp. 1–4, 1998.

Chapter 5

An Optimized Smart pOCT Pixel

5.1 Introduction

Real-time parallel or full-field OCT using conventional CCD or CMOS APS image sensors as detection units suffers from two important disadvantages as already seen in Sec. 3.5: Firstly, typical imager frame rates are far below the Nyquist sampling frequency of the interferometric signal, secondly, the full well capacitance is in general much too low to reach the OCT inherent high sensitivity without oversampling.

Real-time pOCT systems with frame rates of a few Hertz to several ten Hertz produce interferometric signals with a modulation frequency of typically several tens of kHz. The envelope of these signals bears the tomographic information that is to be detected. The carrier frequency, called Doppler frequency, is directly proportional to the axial scanner speed and, hence, cannot be reduced if real-time 3D imaging is demanded. By the theorem of Nyquist, the sampling frequency must exceed the bandwidth of the interferometric signal by at least a factor of 2. For optimum envelope detection, the image sensor frame rate should be four times the Doppler frequency [1] or even more [2, 3], resulting in hundreds of kHz compared to conventional image sensors' frame rates of only hundreds of Hz. There has been research to avoid the Nyquist limit by modulating the illumination source [4]. With this method, the detected signal depends on the phase difference between the illumination source modulation and the interference modulation. Since this phase can not be known beforehand, some information is lost, and the sensitivity is reduced. Although this technique is unsatisfactory for pOCT, if applied to optical coherence microscopy (OCM) that detects the reflection coefficient at a certain depth with several phase-shifted images, multiplexed lock-in

detection by modulating the illumination source power has been shown to be a powerful technique [5,6].

The modulation to be detected in the interferometric signal is several decades smaller than the constant signal offset. As mentioned in Sec. 3.4, the sensitivity of an ideal time-domain OCT system corresponds to twice the number of electrons generated from photons coming from the reference arm (assuming a reference arm power reflectivity of 1) during the given envelope integration time, e.g. a sensitivity of $S = 80$ dB corresponds to 50 millions of integrated electrons. Compared to this requirement, commercial image sensors have rather low full well electron capacitances of some ten thousand to about half a million electrons. The use of a logarithmic imager or even a LinLogTM sensor [7] to increase the full well is discussed below. This type of pixels is not advantageous due to their signal compression at higher levels and the signal-level dependence of their integration bandwidth.

Therefore, parallel or full-field OCT for high speed applications rely on dedicated pOCT image sensors that overcome these two limitations of conventional image sensors at the pixel level.

5.2 Theory on pOCT sensors

Both problems of conventional imagers stated above could potentially be solved with ultra high-speed sensors. But there seems to be no way to design an imaging system that acquires several hundred thousand frames per second offering sufficient resolution at reasonable cost, e.g. with a silicon based single chip approach. An additional problem is the signal processing of such an amount of data in real-time.

The versatility of semiconductor technology allows the monolithic integration of photosensitive, analog and digital functionality on a single chip. Thanks to the continuing advances of CMOS processes and continuously decreasing feature sizes to the deep sub-micrometer range, so called smart pixel imagers even include additional signal processing at the pixel level, allowing completely new directions for image sensing [8]. For these reasons, a CMOS smart pixel architecture approach has been chosen to solve the pOCT detector problems with massively parallel signal processing at the pixel level.

Since the above mentioned frame rates required by the Nyquist sampling theorem can not be reached, signal pre-processing has to be applied, making it possible to read out only relevant depth information. The information of the interferometric signal is in the envelope of the modulation. The in-pixel processing must assure the possi-

bility to reconstruct the original envelope without loss of information. Averaging is only done after signal amplitude demodulation or envelope detection. The pixel read-out frequency must still comply with the Nyquist sampling theorem for the envelope bandwidth. The frame rate therefore can easily be reduced by almost two decades for a typical OCT illumination source. The amount of read out data is reduced by the same order.

The sensitivity disadvantage of conventional imagers due to their limited full well can be overcome by adding an additional capacitance. Although this bears the disadvantage of compressing the sensed optical signal in the voltage domain due to a reduction of the conversion factor. A more advanced offset compensation circuit removes a substantial part of the constant signal component without affecting the conversion factor. Some of the demodulation principles proposed below inherently increase the full well capacitance.

5.2.1 In-pixel demodulation requirements

Signal demodulation or envelope detection inside a CMOS pixel architecture underlies completely different boundary conditions than the demodulation circuits of fiber-optic OCT systems. Not only are the frequencies reduced by a factor corresponding to the number of lateral pixels, assuming the same volume acquisition rate. More important is the fact that the demodulation principle must have a corresponding electrical circuit that is realizable within a pixel. This means it must be realizable in standard CMOS technology without process modifications, e.g. neither inductors, nor varactors, nor CCD nor similar structures are allowed. Furthermore, the area consumption and the power dissipation must be sufficiently low to allow a large two-dimensional matrix of pixels on one chip. The demodulation and filter frequencies shall be tunable to allow the use of the same sensor in different illumination spectrum and scan speed conditions. Evidently, stable operation independent of the illumination signal level over a certain range of temperature must be guaranteed.

The power consumption is mainly limited by the allowable die temperature and the thermal resistance to ambient temperature $R_{\theta,JA}$ of the sensor carrier. Compared with other image sensors, the sensor temperature can be allowed to reach rather high values, since dark current is no major issue because it is removed together with the large signal offset, and dark current noise is negligible compared with the photonic shot noise. With a power dissipation of $5\ \mu\text{W}$ per pixel, large arrays with several ten thousands pixels are achievable, operating at a sensor temperature of less or equal 85°C .

The maximum die size corresponding to the reticle size (if no stitching is applied), is

typically around 400 mm^2 or less. Smaller sensor sizes are preferred not only because of the silicon production costs but also for the optical system. Some CMOS processes allow a big reduction in mask costs, which are the main costs for low volume production, if the sensor die fits into one quarter of the reticle. For a reasonable pixel field of $7 \times 7 \text{ mm}^2$ and a minimum resolution of 100×100 pixel, the maximum area per pixel is estimated to be $5000 \mu\text{m}^2$. Assuming half of this area is used for the photo-sensitive element and the pixel readout buffer, this leaves the other half for the signal demodulation circuitry.

Targeting an OCT sensitivity of 80 dB, the demodulation circuit must feature shot noise limited operation for the corresponding illumination, and desirably also for weaker optical powers. The dynamic range, i.e. the ratio between the largest and the smallest detectable modulation amplitude, is maximized by adjusting the conversion factor between the modulated optical power per photodiode and the output signal swing.

5.2.2 Different demodulation principles

The intensity variation of the interferometric signal is comparable to a double-sideband, full carrier amplitude modulation (DSB-AM) radio signal with an additional constant part. For this reason some OCT signal processing concepts have been borrowed from radio signal theory. In the following, a non-exhaustive list of well-known or derivative demodulation principles is presented and discussed with respect to the established in-pixel criteria.

Product demodulation using a rectifier

Arguably the simplest amplitude demodulation principle makes use of a non-linear element such as a rectifying diode to detect the envelope by multiplying the signal carrier with its sidebands. In the year 1901, eight years after Nikola Tesla made the first public presentation of radio communication [9], J. C. Bose filed a patent describing the first solid-state diode detector [10, 11]. Hundred years later, the circuits look basically the same: The input signal is first bandpass filtered corresponding to the desired signal spectrum, then rectified, and finally a low-pass filter removes the so called image frequency. Fig. 5.1 shows the three stages and a typical OCT signal before and after each stage. This method has been explored for the parallel OCT smart imager developed by Bourquin [12–15]. The disadvantage of this demodulation technique is the need for large RC-constants for frequencies below 10 kHz. This works well for very stable illumination conditions. But the design of signal level independent filters with these frequencies in standard CMOS technologies is incompatible with the required small

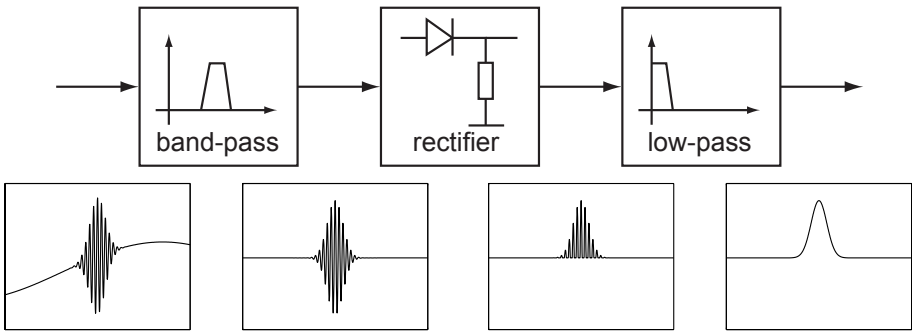


Figure 5.1: AM-demodulation of a typical OCT interferogram signal with a diode detector: the input signal is band-pass filtered, rectified and low-pass filtered; shown are the circuit blocks and corresponding signals.

pixel size, and therefore this principle becomes impractical for this application.

I-Q direct detector or lock-in detector

The I-Q direct detection principle consists of an analog or digital multiplication of the input signal with an oscillator signal matching the carrier frequency in one path (in-phase signal) and in quadrature in a second path (90 degrees temporal shift) followed by a low-pass filter that removes the image frequency part (Fig. 5.2). 'Direct' refers to the fact that the demodulation is done in one step without intermediate frequency mixing. In other applications this technique is named lock-in detection because the system is 'locked' on the signal component of a very narrow frequency band. A big advantage of this detector, if two mixers are applied, is the use of the information of both frequency side bands to reconstruct not only the amplitude of the envelope as the Euclidean norm of the two output signals, but also to determine the phase shift between the signal carrier and the demodulation signal. This renders this principle potentially useful for some functional OCT such as Doppler OCT to measure e.g. vascular flow velocities [16], and polarization-sensitive OCT as used for example for birefringence detection [17]. Furthermore, investigating this additional information may also increase the depth accuracy, especially for topography measurements [18].

Disadvantages of this detector are the doubling of the output signals and therefore also of the amount of data to be read out, as well as the increased off-sensor calculation effort. However, by use of the CORDIC algorithms [19,20] on programmable logic on the camera, the calculation effort is reduced to a pipeline of a few clock cycles. Another

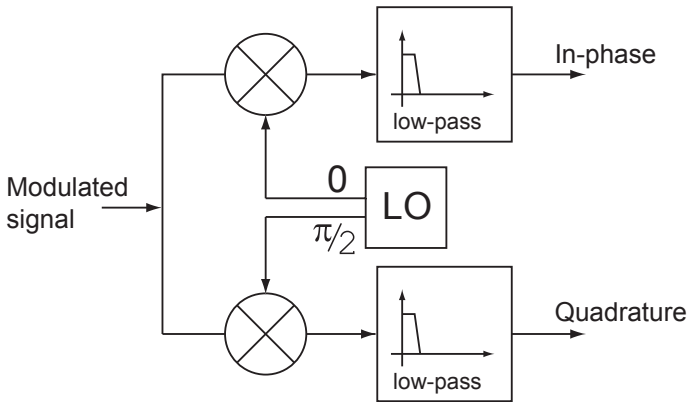


Figure 5.2: I-Q product direct detector with multiplication stages and low pass filters: The two multiplication stages obtain reference signals from the local oscillator differing from each other by a phase shift of 90 degrees. Their frequency equals the input signal's modulation frequency.

problem is the potential mismatch between carrier frequency and demodulation frequency leading to a signal beating that may reduce the measured amplitude for large time constants of the low-pass filter.

Furthermore, the analog signal multiplication, for example with a Gilbert cell [21], is complex and power consuming compared to the power available in every pixel. Finally, the main disadvantage and eliminating criterion is that the same filters as mentioned in the diode mixer circuit would have to be implemented, which is not possible with the specified pixel size.

I-Q direct detector with discrete-time mixers and integrators

The I-Q detector is a very interesting demodulation method. Can the weaknesses that make it unsuitable for in-pixel use be overcome? The sinusoidal multiplication signal can be replaced by either a square wave of the discrete values $[-1, +1]$ or a tristate signal of values $[-1, 0, +1]$, with the disadvantage of a reduction of the SNR by 4 dB for the former but only less than 1 dB for the latter due to the natural sampling as shown in Sec. 4.2. This opens up the use of completely different mixer structures based on integrate, sample, and hold circuits and subtractor and adder structures in switched capacitor (SC) or switched current (SI) IC design techniques.

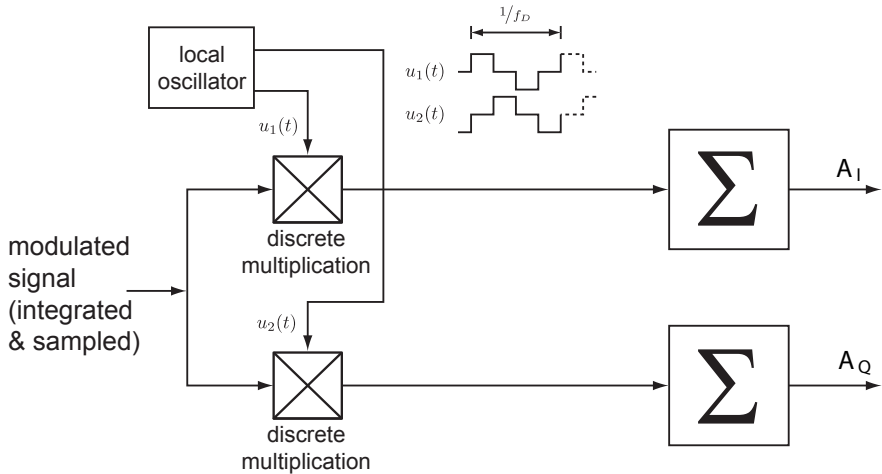


Figure 5.3: I-Q direct detector approach with discrete-time mixing stages and low-pass filtering. The two multiplication stages have reference signals from the local oscillator differing from each other by a phase shift of 90 degrees. Their frequency equals the modulation frequency of the input signal. The input signal is sampled at four times the demodulation frequency. After the mixing in the discrete multiplication stages, the samples are summed up in an integrator stage to filter out the image frequency at twice the modulation frequency. The summation also provide for noiseless signal time averaging.

Fig. 5.3 shows a block diagram of a I-Q direct demodulator with discrete-time mixers and integrators. The optical input signal is integrated and sampled (not shown in the diagram) with a sampling frequency four times the demodulation frequency (local oscillator frequency). Then the samples are multiplied with 1, 0, and -1 according to their order. By summing up the samples, the image frequency at twice the demodulation frequency is filtered out, and time averaging is performed to reduce the amount of read out data without losing SNR performance.

This demodulation principle has been chosen and implemented in the developed smart pixel architecture. An interpretation of the implementation as envelope detection algorithm is discussed below.

Complex analog demodulation techniques

A glance at any radio amateur handbook, e.g. [22], reveals a multitude of variations improving the performance of the presented first two demodulation principles, to-

gether with many other demodulation principles. For example superheterodyne detectors convert the input signal first to an intermediate frequency for signal filtering and level controlling before the signal is down converted to output frequency range. Synchronous detection takes advantage of a phase-locked loop (PLL) to recover the carrier frequency for signal mixing, while in quasi-synchronous detection the PLL is replaced by just amplifying and amplitude limiting of the AM signal. Quadrature detection consists of mixing of the input signal with a time delayed copy of itself. A Hilbert transformer performs a wide band 90° phase-shift operation and may be used to generate the signals for envelope detection. All these and other analog demodulation principles are not discussed here, because they seem far from being implementable in a CMOS smart pixel architecture.

Digital signal demodulation

All of the mentioned analog demodulation techniques can also be implemented in the digital domain. In addition, it is also possible to use more sophisticated digital signal processing such as e.g. the fast fourier transform (FFT) [23, 24], digital Hilbert transform [2, 25], or digital deconvolution [3] to detect the signal envelope. Although in-pixel analog to digital conversion (ADC) exists, up to now their implementations are either rather area consuming [26,27], or are not entirely placed inside the pixel but depend on an off-pixel post-processing stage, such as e.g. a digital low-pass filter in the case of $\Sigma\Delta$ ADCs [28] or counters for clock output [29] and voltage-to-frequency pixels [30]. Many of the known pixel-level ADC principles require a constant photocurrent during the full integration time for correct operation, which is not the case in OCT. Nevertheless in-pixel digital signal demodulation with the targeted frequencies could become an alternative for future CMOS processes with further reduced feature sizes, possibly in combination with a hybrid image sensor technology to increase the fillfactor to close to 100%.

Envelope detection algorithms

A different class of amplitude demodulation principles working in the digital domain, but also imaginable for the analog domain, are the phase-shifting or envelope detection algorithms. A three samples per fringe period algorithm was one of the first applied to white light interferometry [31]. Other very popular algorithms [1], closely related to the digital Hilbert transform, typically take four samples per modulation period after bandwidth limiting the input signal in order to avoid aliasing effects. An extremely simple example of a five-step algorithm with low computational effort and astonishing

robustness towards sampling frequency variations is the one proposed by Larkin [1, 32]. The envelope at a certain point in time is calculated from five successive samples by

$$E_n^2 = (I_{n+1} - I_{n-1})^2 + (I_n - I_{n-2}) \cdot (I_n - I_{n+2}) \quad (5.1)$$

Low-power and small-area analog signal subtraction or addition circuits can be developed taking advantage of the SC design technique. But low-noise analog signal squaring and multiplication is power consuming with respect to the defined in-pixel power dissipation criterion. An envelope detection algorithm can therefore not be entirely implemented within the smart pixel floor space.

Simple envelope detection algorithm with time averaging

A simple four-step version of the above mentioned envelope detection algorithm [33, 34] is also known as lock-in principle and has already been implemented in other smart pixels, so-called lock-in pixels e.g. for time-of-flight (TOF) range imaging [35] for other frequency ranges and fluence levels. The envelope values are given by

$$E_n^2 = (I_{n+3} - I_{n+1})^2 + (I_{n+2} - I_n)^2 \quad (5.2)$$

$$E^2 = \left[\sum_{n=0}^{N-1} (I_{4n+3} - I_{4n+1}) \right]^2 + \left[\sum_{n=0}^{N-1} (I_{4n+2} - I_{4n}) \right]^2 \quad (5.3)$$

in the four-step and the $4N$ -step version.

As mentioned before, by using the SC design technique, simple subtraction and summation circuits can be implemented with low power dissipation and small area requirements. If the two summands of Eq. 5.3 are read out of the pixel, the envelope as their Euclidian norm can be calculated off-pixel or even off-chip. The disadvantage of a doubled amount of read-out data compared to the minimally necessary data flow is compensated by the advantage that also the phase can be recovered from the two signals. Fig. 5.4 shows a schematic view of a circuit implementing the $4N$ -step envelope detection algorithm.

Prior to the sampling, the input signal must be bandwidth limited with respect to the Nyquist frequency to prevent aliasing. Furthermore, low-pass filtering increases the SNR of the samples to the photonic shot-noise limit. Integration of the modulated input signal over a quarter demodulation period can be seen as a signal convolution or filtering with a rectangular signal in the time domain leading to a multiplication of the input signal spectrum with a sinc function in the frequency domain, where the

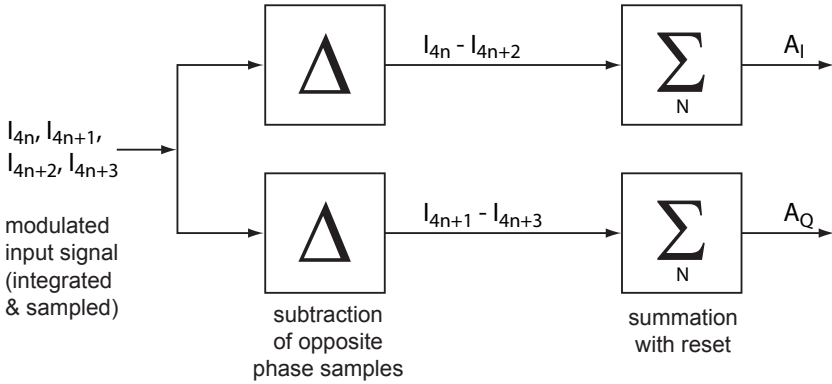


Figure 5.4: Building block view of a $4N$ -step envelope detection algorithm circuit. The modulated input signal is integrated and sampled (not shown) with a frequency four times the modulation frequency. The envelope detection consists of two identical circuit paths that are time shifted with respect to each other by one sample. In each path the difference of two samples is determined, of the pair samples in one path and of odd ones in the other. Then N differences are summed up, and these two sums are finally read out. The calculation of the envelope as Euclidian norm and the phase is done off-pixel.

bandwidth is reciprocally proportional to the integration time. As described in Sec. 4.2, a loss of less than 1 dB in SNR is caused by the natural sampling process [36,37].

The above described demodulation principle of the I-Q direct detector with discrete-time mixers and integrators, and the $4N$ -step envelope detection algorithm presented in this section are different interpretations of exactly the same circuit. This circuit has been chosen for the smart pixel architecture implementation because of its simplicity, its general nature, and the practicality of its implementation.

5.2.3 Transducer stage with offset reduction

The chosen demodulation principle together with an integrate, sample, and hold transducer stage reduces the targeted full-well capacitance of 50 millions of integrated electrons for a sensitivity of $S = 80$ dB by a factor $4N$ for the sampling stage. This corresponds to a full-well capacitance of 1.25 millions of photoelectrons or a photocurrent of $I_{ph} = 40$ nA for the specified modulation frequency $f_{mod} = 50$ kHz, leading to a large but for a custom design image sensor not impossible photodiode node capacitance of 200 fF at 1 V swing and a photonic shot noise of around 0.9 mV. For smaller numbers

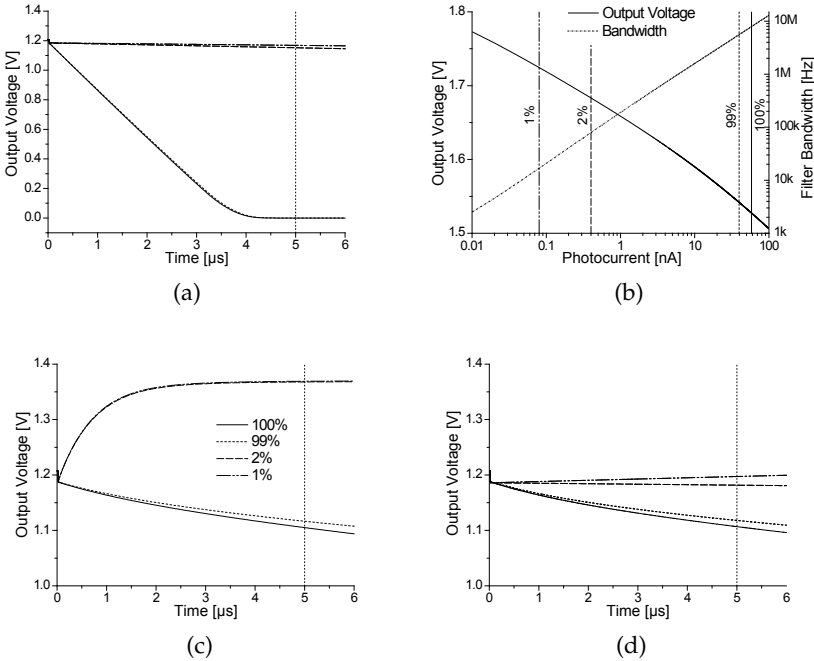


Figure 5.5: Simulation of different transducer stages with a photocurrent of 40 nA, 39.6 nA, 0.8 nA, and 0.4 nA, the maximum yielding a sensitivity of 80 dB under typical conditions (resp. 77 dB for stages with compensation current). (a) A transducer stage without offset reduction or signal compression saturates for the large currents. (b) In the logarithmic transducer stage, the signals do not saturate, but the integrating bandwidth depends on the current. (c) A transducer stage with a fixed offset compensation current shows correct output signals for the large currents but saturates for the small ones. (d) The transducer stage with the adaptive current compensation exhibits favorable behavior for both the large and the small photocurrents.

of repetition N or for higher sensitivities, an alternative solution than ever increasing the photodiode node capacitance must be found. The transducer stage shall be implementable in a conventional CMOS process and its signal shall be shot-noise limited. Solutions based on logarithmic photocurrent to voltage conversion and photocurrent compensation are discussed below.

The simulation results of the different approaches are shown in Fig. 5.2.3. As reference example, a simple APS with an NMOS follower (gain of 0.8) without offset limitation avoidance has been simulated with a photodiode node of $C_{pdn} = 100$ fF and a linear output swing of 1 V, leading to a full well capacitance of 780'000 photoelectrons. The

simulated photocurrent $I_{\text{ph}} = 40 \text{ nA}$ leading to a possible number of 1.25 million integrated electrons in the given time interval clearly saturates the transducer stage (Fig. 5.5(a)). A difference of 1 % in photocurrent can not be distinguished. This transducer stage works acceptably for smaller currents. The graph shows also the analysis with photocurrents of 1 % and 2 % of the initial current. Increasing the photodiode node capacitance to avoid saturation for large currents, if the available in-pixel area allows it, reduces the slope of the signals and therefore also the difference of two photocurrents that has to be detected subsequently.

Logarithmic response photodetection

The use of a logarithmic sensor such as a diode pixel as first proposed by Chamberlain *et al.* [38] allows very large photocurrents without saturation. A forward biased diode or an NMOS transistor in diode configuration is placed in series with the photodiode (see Fig. 5.6(b)). The diode transistor is in weak inversion for photocurrents smaller than

$$I_{\text{ph}} \leq \frac{I_{\text{lim}}}{8} = \frac{\beta 2nU_T^2}{8}, \quad (5.4)$$

and the output voltage becomes

$$V_{\text{out,log}} = \frac{VDDA}{n} - U_T \ln \left(\frac{I_{\text{ph}}}{I_{D0}} \right), \quad (5.5)$$

where $VDDA$ is the positive power voltage, the factor n , sometimes called subthreshold slope factor, is CMOS process dependent and usually between 1 and 1.5, $U_T = kT/q_e$ is the so-called thermal voltage and is around 26 mV at room temperature, and I_{D0} is also process dependent and proportional to the transistor aspect ratio. For larger photocurrents, the transistor goes into moderate and then strong inversion, and the output response shows a square root relationship. The non-linear behavior may introduce signal distortion for large OCT signals, e.g. when the difference between two subsequently measured photocurrents is large. But for small differences, the output can be linearized.

For optimum shot noise limited detection, the transducer stage signal shall be low-pass filtered with a bandwidth as small as possible without attenuating the input signal at the modulation frequency. As can be seen from the small signal schematic Fig. 5.6(d), the logarithmic transducer stage contains a first order low-pass filter with a bandwidth

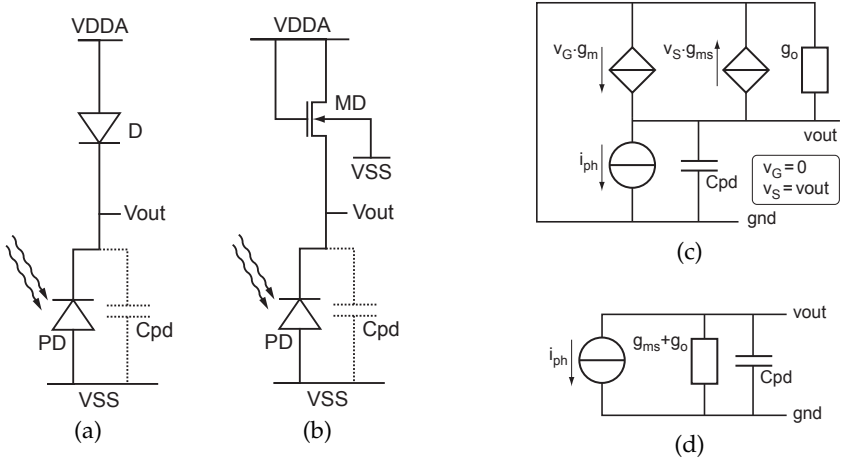


Figure 5.6: Schematic of a logarithmic transducer stage: (a) A forward biased diode is placed in series with the photodiode. The diode is replaced by an NMOS transistor in diode configuration in (b). (c) shows the small signal equivalent circuit, and (d) shows its simplified version exhibiting a low-pass filtered current to voltage conversion with a bandwidth of $BW \simeq g_{ms} + g_o / 2C_{pdn}$.

$BW \simeq g_{ms} + g_o / 2C_{pdn}$. The source transconductance in weak inversion is given by

$$g_{ms} = n \cdot g_m = \frac{I_{ph}}{U_T}, \quad (5.6)$$

and is much larger than the output conductance g_o . The above mentioned photocurrent $I_{ph} = 40 \text{ nA}$ together with a reasonable photodiode node capacitance leads to low-pass filter frequencies in the tens of MHz and exceeds the required low bandwidth by more than two decades. Additional filtering is therefore needed for optimum low-noise detection, which is a difficult task with respect to the available in-pixel area.

Signal transducer stage with offset compensation

By adding a constant compensation charge at a certain moment or continuously through a compensation current, the full well is increased by the total number of additional charges. The difference of two photocurrents is not affected. The result is similar as if the linear range was increased but with the advantage of a high charge to current conversion factor and moderate output voltages. Pixel-wise adding of a constant, externally controlled compensation current to enlarge the full well capacitance and the

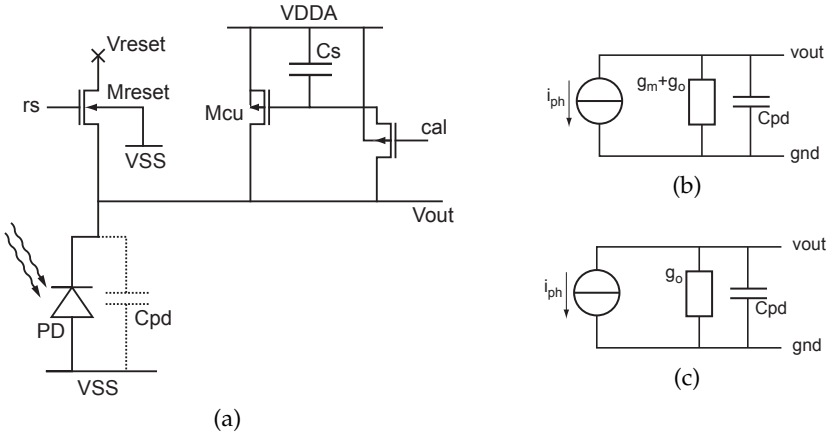


Figure 5.7: Schematic of a transducer stage with adaptive current compensation: (a) While *cal* is low, a current matching the photocurrent is programmed into the current memory cell formed by the transistor M_{cu} and the storage capacitor C_s . When *cal* goes low, the programmed current is delivered to the photodiode node independently of the photocurrent. (b) shows the small signal model during the calibration phase, and (c) its equivalent during the current compensation phase.

pixel’s dynamic range has been described for example by Vietze *et al.* [39]. The simulation result of the above mentioned APS pixel enhanced by a PMOS as programmable current source is shown in Fig. 5.5(c). A long transistor has been used to reduce the influence of the drain source voltage on the compensation current. It can be shown that a finite Early voltage V_{EARLY} leads to a signal non-linearity of exponential behavior. Integrating the photocurrent on a charge integrator instead of the photodiode inherent capacitance, avoids this effect at the cost of area and power-consumption. The same compensation current (39 nA) has been programmed for all simulated photocurrents (40 nA, 39.6 nA, 8 nA, and 4 nA) with the effect that for the small currents the pixel saturates. The average illumination power on the pixel array usually follows a Gaussian distribution. A homogenous distribution is only possible with a significant loss of power. The compensation current must therefore be programmed individually for every pixel.

The disadvantage of the need for time-costly programming of each pixel current is overcome by pixel-wise adaptive current compensation described for example by Fossum *et al.* [30,40]. A current memory cell is integrated into the transducer stage. During a calibration phase the additional current is adjusted to compensate for the photocurrent of every pixel. Thanks to the subsequent demodulation stage incorporating sig-

nal subtraction, an approximative current compensation is sufficient. The most basic implementation is shown in Fig. 5.7(a), its simulation results with two current pairs (40 nA/39.6 nA and 8 nA/4 nA) are shown in Fig. 5.5(d): The transducer stage is calibrated with the larger of the two currents, then the pixel is reset and the indicated photocurrent is applied. The charge injection by the transistor M_{cal} increases the potential on the gate of the current source M_{cu} , which lowers the compensation current and leads to a negative voltage slope for all signals. As described above, a small non-linear behavior is noticeable. None of the simulated current signals saturates the transducer stage. The β of the current source is chosen as a trade-off between a large Early voltage and the signal swing, which is limited by the drain source saturation voltage $V_{\text{DSsat}} = V_{\text{CS}} - V_{\text{T}}/n$.

Figs. 5.7(b) and (c) show the small signal model of the described basic compensating transducer stage during calibration and compensation, respectively. They show a current to voltage conversion with a low-pass filter with different cut-off frequencies. During calibration, the output voltage must settle close to its asymptotic limit. Therefore the calibration should last for several time constants $\tau_{\text{cal}} = C_{\text{pdn}}/g_{\text{m}} + g_{\text{o}}$ i.e. some microseconds in our example. During compensation, the transducer stage shall act as integrator, which implies that the integration time should be significantly less than the time constant $\tau_{\text{cal}} = C_{\text{pdn}}/g_{\text{o}}$, which in the case of our example is of the order of some hundreds of microseconds.

The offset compensation circuit adds some temporal noise to the detected signal. Only if this additional noise is significantly less than the photonic shot-noise, the transducer stage is said to be shot-noise limited. Is this possible? If we consider a transducer stage without compensation, and we fill it with a certain mean number N_1 of photoelectron charges, due to the Poisson distribution of the carriers, its noise is $\sqrt{N_1}$ photoelectrons. If now a certain mean number N_2 of electron charges with a noise of $\sqrt{N_2}$ is subtracted, the remaining signal has a noise corresponding to $\sqrt{N_1 + N_2}$ charges. In the same way, our transducer stage with the offset compensation current equaling the mean photocurrent increases the photonic shot-noise by at least a factor $\sqrt{2}$ or 3 dB. The transistors are designed in order to contribute negligible thermal and flicker noise.

5.3 Realization of the discrete time direct demodulation pixel architecture

The following section describes the implementation of the above described lock-in or time-discrete I-Q direct demodulation principle in a smart pixel architecture.

5.3.1 Targeted specifications

The power dissipation per pixel is to be less than $5\ \mu\text{W}$ and the area consumption less than $5000\ \mu\text{m}^2$ with a fill factor of at least 10%. The depth scan speed of the pOCT system shall be around $20\ \text{mm/s}$. With an illumination source peak wavelength $\lambda_0 \sim 800\ \text{nm}$, this leads to a Doppler frequency of 50 kHz. Cost-effective high-power illumination sources at this wavelength feature coherence lengths leading to FWHM depth resolutions ranging from about $6\ \mu\text{m}$ to $15\ \mu\text{m}$. By reading out at least 2 to 3 depth samples per envelope, the number of periods, over which the signals are averaged, becomes $N = 7$ to 12, offering a depth sampling distance of 3 to $5\ \mu\text{m}$.

Assuming a reference path reflectivity of 100%, the theoretical shot-noise limited sensitivity can be estimated as a function of the total received number of photogenerated charges leading to a rule of thumb

$$S_{\text{pOCT}} = 10 \log \left(2 \cdot n_{\text{pe}^-} \right) - \begin{cases} 1\ \text{dB} & \text{without additional offset compensation,} \\ 4\ \text{dB} & \text{with additional offset compensation,} \end{cases} \quad (5.7)$$

where n_{pe^-} is the number of detected photoelectric charges during the total sampling time. The reduction by 1 dB is due to the natural sampling over a quarter demodulation period, the additional reduction by 3 dB is due to the shot noise of the compensation current. By reducing the optical power from the reference arm, the number of photoelectrons can be reduced without reducing the sensitivity.

As mentioned in Sec. 5.2.1, the achieved OCT sensitivity is to be above 80 dB, leading to more than 100 million photoelectric charges to be handled according to the rule of thumb. But the pixel performance shall also be shot-noise limited already at smaller irradiance. An optical power of 20 nW per photodiode at a peak wavelength of $\lambda_0 \sim 820\ \text{nm}$ together with a scan speed of $v = 20.5\ \text{mm/s}$ and a depth sampling of $4.5\ \mu\text{m}$ features a sensitivity of 69 dB and shot-noise limited operation according to the simulations. Since the measured temporal noise of the overall electronic system is larger than the simulated noise in the pixel, this limit is not achieved. System operation, for which the shot-noise equals the electronic noise is only guaranteed for an optical power of more than 70 nW per photodiode, respectively for an irradiance on the photosensitive area of $160\ \text{pW}/\mu\text{m}^2$ under the same conditions, yielding 74 dB. The offset compensation circuit shall allow to countervail a maximum photocurrent of 500 nA corresponding to 620 million photo-charges per depth sample or 86 dB sensitivity. Higher sensitivities at the cost of increased illumination powers are achievable by adding a neutral density filter in the reference path.

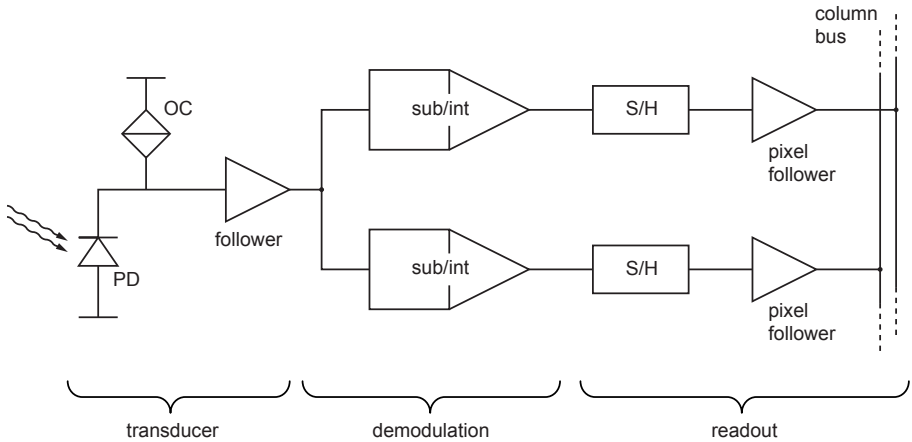


Figure 5.8: Schematic drawing of the pOCT smart pixel: The incoming light is converted to an electric signal in the photodetector (PD), the offset compensation unit (OC) reduces the signal offset. After the follower, the signal is split in two paths and mixed in the subtraction and integration block. The sample and hold stages (S/H) allow the simultaneous integration and read out of the pixel.

5.3.2 Pixel architecture

Fig. 5.8 shows an overview block diagram of the pOCT smart pixel schematics. There are three main blocks: the transducer stage, the discrete time demodulation stage and the readout circuitry. The incoming light is converted to an electrical signal by the photodetector in the transducer stage. The offset compensation unit reduces the signal offset by adding a constant current in the same order as the constant part of the photocurrent. A buffer follows to adapt the impedance. The demodulation stage is composed of two discrete-time mixers consisting of a subtracting and integrating circuit. The readout block contains two sample and hold stages that allow the simultaneous integration and read out of the pixel. The sample and hold stages are each connected to a buffer that drives the column bus.

When operated in demodulation mode, first the integrators are reset, and the offset compensation circuit is calibrated. Then the transducer stage starts a series of N times four integrations of a quarter of the demodulation frequency period each. N is the number of repetitions and freely selectable. These signals are buffered into the demodulation stage. The demodulator stage forms the subtraction of samples one and three and stores the result on one integrator. The subtraction of samples two and four are stored on the other integrator. This process is repeated N times and the subtraction re-

sults are added up in the two integrators consequentially. These sums of subtractions are then stored in the sample and hold stage. Then the integrators are reset, the offset compensation circuit is calibrated again, and the same sequence starts all over. While new signals are demodulated, the sums in the sample and hold stages are read out. The design has been optimized for typical values of number of repetitions $N = 10$ and demodulation frequency $f_{\text{demod}} = 50$ kHz. The time for one sequence is the reciprocal value of the sensor frame rate and given by $1/f_{2\text{Dframe}} = T_{\text{seq}} = (N + 1) \cdot 1/f_{\text{demod}} = 220 \mu\text{s}$ for the typical values.

5.3.3 Transducer stage

The basic structure of the transducer stage is very similar to a three transistor active pixel sensor (3T APS) pixel structure (see Fig. 5.9.) It consists of a photodiode (PD, n-well – p-substrate), an NMOS reset switch (NM1) and source follower (MP2). The source follower drives the capacitive input of the demodulation stage and in contrast to a conventional 3T APS, its current source (MP3) is integrated in the pixel. In the demodulation mode the optical signal received by the photodiode is integrated on the intrinsic capacitance (Cpd) during a quarter of the modulation frequency period, typically around $5 \mu\text{s}$. After the integration, when the voltage on the photodiode node (Vpd) is buffered into the following stage, the photodiode is reset. Transistors MP4 to MP6 build the programmable photocurrent offset compensation circuit.

Transducer buffer

A PMOS type source follower has been chosen for the following reasons: PMOS followers feature better linearity and almost unity gain in the applied CMOS technology since they may have a separate well, and PMOS transistors have less flicker noise than NMOS. Furthermore PMOS exhibit a lower transconductance parameter β_{\square} than NMOS, which eases the design of very small current sources. Large photocurrents are expected and we are not interested in detecting small currents but small differences of large currents. A PMOS follower therefore is better suited since it features a high linearity at low input voltage levels e.g. at high integrated signals, whereas an NMOS follower saturates at input voltages below 0.8 V . This implies that in cases, where small photocurrents are detected, the reset voltage V_{reset} must be set significantly below the supply voltage V_{DDA} .

During the reset time (around 100 ns) not only the intrinsic photodiode capacitance must be set to the applied reset voltage, but also the follower output must drive its capacitive load (demodulation stage input, $2 \times 35 \text{ fF}$) and become stable. Otherwise

saturates the pixel completely during an integration time of $5\ \mu\text{s}$. For illumination powers of more than $200\ \text{nW}$ per photodiode (around $40\ \text{nA}$ photocurrent), the offset compensation circuit should be used.

Switch MP6 is only used to activate and deactivate the offset compensation feature. MP4 and MP5 act as a switched current (SI) circuit. During a calibration phase the photodiode reset switch MN1 is open, the switch MP4 is closed and the transistor MP5 is behaving like a forward biased diode or the input device of a current mirror. The current through MP5 equals the photodiode current. When MP4 opens, the voltage on the gate of MP5 is stored and MP5 acts like a constant current source or the output device of a current mirror delivering a current equal to the photodiode current during the calibration.

Usually current mirrors are operated in strong inversion due to the reduced influence of the threshold voltage mismatch from device to device on the current mismatch. In this case, device mismatch is irrelevant. Nevertheless the transistor MP5 is dimensioned to be in strong inversion to reduce the influence of the drain-source voltage as well as the influence of a gate voltage variation due to kTC noise or charge injection by MP4. An adjustable photodiode reset voltage assures operation in the saturation region.

The maximum offset compensation current is set to $500\ \text{nA}$. MP5 is designed with a minimum width to length ratio to reduce the above mentioned current variations due to gate source voltage variations. It has maximum length with respect to the available pixel area because the current of long transistors depends less on the drain source voltage due to a larger Early voltage. Compensation current dependency on the integrated voltage introduces signal non-linearity. Another reason to make MP5 as large as possible is to increase the gate capacitance to minimize the voltage variation due to the charge injection and the leakage current of MP4. MP4 is designed as PMOS switch in order to avoid trapping of photogenerated charges in the substrate on the drain diffusion that would influence the current source gate voltage.

Even though only approximate offset signal compensation is required, it is imperative that the mismatch between the compensation current and the average photodiode current is significantly smaller than the above mentioned photodiode saturation current of $60\ \text{nA}$. Therefore the impact of all these mentioned parasitics on the compensation current must respect this limit.

Transistor MP5 is dimensioned to be in strong inversion for a compensation current of $I_{\text{com}} \geq 8 \cdot \beta 2nU_T^2 \simeq 10\ \text{nA}$. During calibration, the minimum voltage at MP5's gate is limited by MP4 and can be around $1.2\ \text{V}$. A gate source voltage of $V_{GS} = -2.15\ \text{V}$ leads to a maximum offset compensation current of $500\ \text{nA}$ by the drain current equation for

strong inversion:

$$I_d = \frac{\beta}{2n} (V_{GS} - V_T)^2 \cdot \left(1 + \frac{V_{DS} - V_{DSsat}}{V_{EARLY}} \right). \quad (5.8)$$

Offset current variations due to parasitics

There are some parasitic effects that influence the offset compensation current. The influence of the source drain voltage is negligible (less than 0.2 % even for the maximum compensation currents) if the reset voltage is lowered to 2.0 V.

The charge injection of switch MP4 to the gate of MP5 is given by

$$Q_{inj} = 1/2 \cdot c_{ox} \cdot WL \cdot (V_{in} - VSS - V_{T,p}), \quad (5.9)$$

where c_{ox} is the oxide capacitance per unit area, W and L are the width and the length of the transistor, V_{in} is the switched voltage, VSS is the ground voltage that the gate is set to during switching, and $V_{T,p}$ is the PMOS threshold voltage. The voltage change on the gate of the current source leads to a compensation current reduction of about 10 nA for both large and small currents. Since this current mismatch is constant and smaller than the above mentioned limit of 60 nA, no countermeasure is needed. The effect can be reduced by simply reducing the transition speed of the switch operation. As result of this effect, the voltage on the photodiode node has the tendency to decrease during integration even for constant illumination signals. The reset voltage should therefore be set to above the middle of the photodiode swing.

The absolute maximum leakage current through transistor MP4 is specified as $I_{leak} = 0.8$ pA. The time between two calibrations corresponds to the above mentioned sequence time. For a typical sequence time of $T_{seq} = 220$ μ s, this leakage current leading to a voltage change on the gate of MP5 results in an altering of the compensation current by a maximum of 1.5 nA. By the following subtraction stage the influence of this effect becomes negligible. Although the effective leakage current should be significantly smaller, this clearly shows that the offset calibration operation must be executed much more often than once per 3D scan to avoid signal saturation.

5.3.4 Demodulation stage

The demodulation stage consists of two identical paths with a time discrete signal mixer stage in each that work in parallel but phase shifted with respect to each other by 90 degrees, i.e. time shifted by a quarter period of the demodulation frequency. Fig.

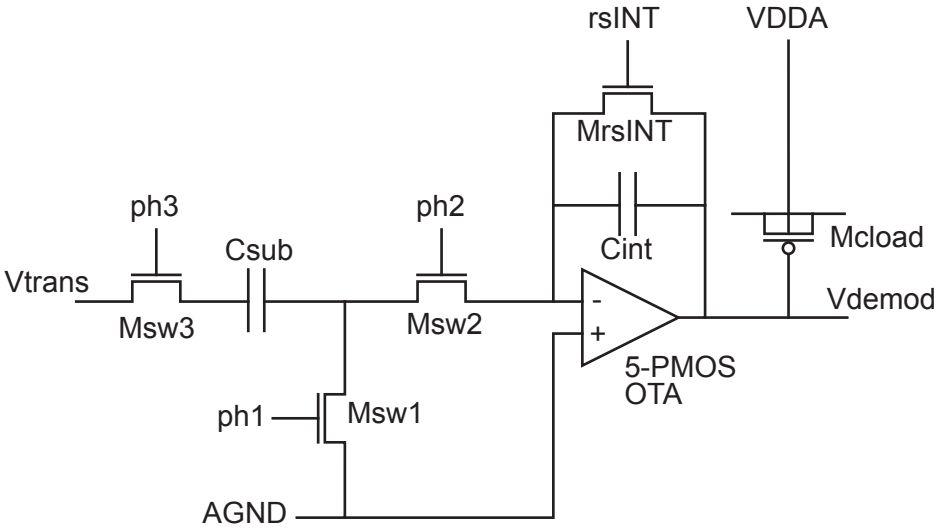


Figure 5.10: Schematic of one arm of the demodulation stage: signal subtractor and integrator circuit. Every pixel contains two of them, operating time shifted in respect to each other by 90 degrees. The switch signals *ph1* and *ph2* are non overlapping opposite phase clocks.

5.10 shows the circuit schematics of one path.

The mixer stage is a signal subtraction and integration circuit that is built in a switched capacitor (SC) design technique. Fig. 5.11 shows the timing diagram for the transducer and the demodulation stages in demodulation mode. At the begin of a demodulation sequence the integrator is reset to the analog ground signal *AGND* by closing the switch *MrsINT*. The switch command signals *ph1* and *ph2* are non overlapping opposite phase clocks. During the first sample *Msw1* is closed and *Msw2* is open. The signal *Vtrans* from the transducer stage charges the subtraction capacitor C_{sub} . For the third sample, *Msw1* is open and *Msw2* is closed, a charge proportional to the difference of the first and the third sample voltage is transferred to the integration capacitor C_{int} . This process is repeated *N* times. In the second arm the differences of the pair samples are summed up. After *N* demodulation periods we have

$$\begin{aligned}
 V_{demod_{stageI}} &= AGND + \sum_{n=0}^{N-1} [V_{trans_{4n}} - V_{trans_{4n+2}}] \cdot \frac{C_{sub}}{C_{int} + C_{ovl}} \\
 V_{demod_{stageQ}} &= AGND + \sum_{n=0}^{N-1} [V_{trans_{4n+1}} - V_{trans_{4n+3}}] \cdot \frac{C_{sub}}{C_{int} + C_{ovl}}
 \end{aligned}
 \tag{5.10}$$

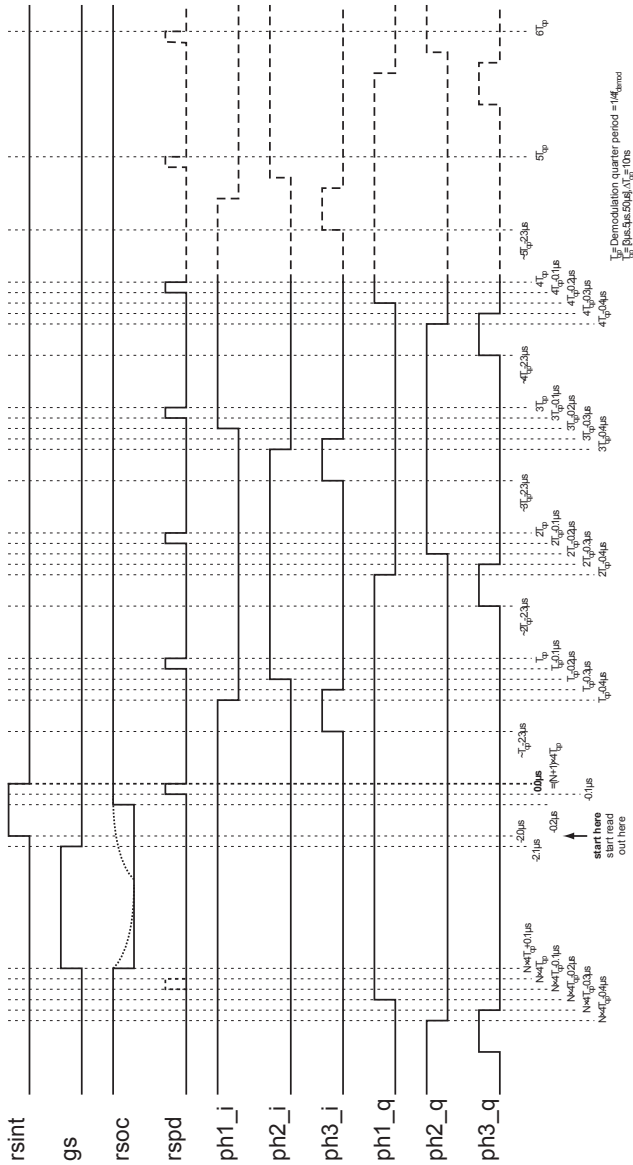


Figure 5.11: Timing diagram of the pixel control signals in the demodulation mode.

for the output voltages of the two integrators. C_{ovl} is the parasitic capacitance between the negative input of the OTA and its output, e.g. the gate drain overlap capacitance of the input transistor. The capacitor ratio is $C_{sub}/C_{int}+C_{ovl} = 0.40$.

Integrator OTA

For reasons of economical use of the pixel's area and available power, a simple amplifier structure has been chosen. The PMOS version of the applied 5-MOS operational transconductance amplifier (OTA) has the advantage of the possibility to reuse the current source gate voltage of the transducer buffer, and it features a reduced flicker noise compared to an NMOS OTA (for a local oxidation of silicon LOCOS process only). Its disadvantage is a slightly increased area occupation and reduced gain and gain bandwidth due to the lower transconductance parameter β_{\square} .

The current mirror NMOS transistors are in strong inversion, the differential pair is in moderate to weak inversion. A maximum gain of more than 62 dB can be achieved. The voltage swing is estimated to be 0.3 V to 2.2 V, where it features a gain of more than 20 dB to suppress parasitic capacitances to ground. The analog ground voltage $AGND$ on the positive input of the OTA determines the virtual ground voltage at the negative input. The output voltage V_{demod} is reset to this voltage by the switch MrsINT. Therefore its value is chosen about half way of the output swing to ensure symmetrical output performance. To assure saturation region operation of the OTA input transistor, it should not be chosen too low, otherwise the higher limit of the swing is reduced.

Simulation analysis

The AC analysis of the demodulator circuit with the switch Msw1 open and the switches Msw2 and Msw3 closed shows a transfer function attenuation of 0.40 that corresponds to the capacitor ratio (see Fig. 5.12). The cut-off frequency is around 1 MHz e.g. the time constant is $\tau \simeq 160$ ns, allowing SC operation with settling times in the order of a microsecond. In the noise analysis, flicker noise and thermal noise are easily distinguishable. The total noise with the specific timing of a signal reset after an interval of N/f_{demod} , is 0.35 mV including the kTC reset noise.

The slew rate is for rising and falling output around ± 0.5 V/ μ s. Fig. 5.13 shows the transient analysis of the OTA including the subtraction and the integration capacitors with a rather large input step of 500 mV, rising and falling. The output step corresponds to the mentioned capacitor ratio attenuation factor. After a delay of 1.5 μ s for rising and for falling output, the remaining error of the output signal due to the limited OTA

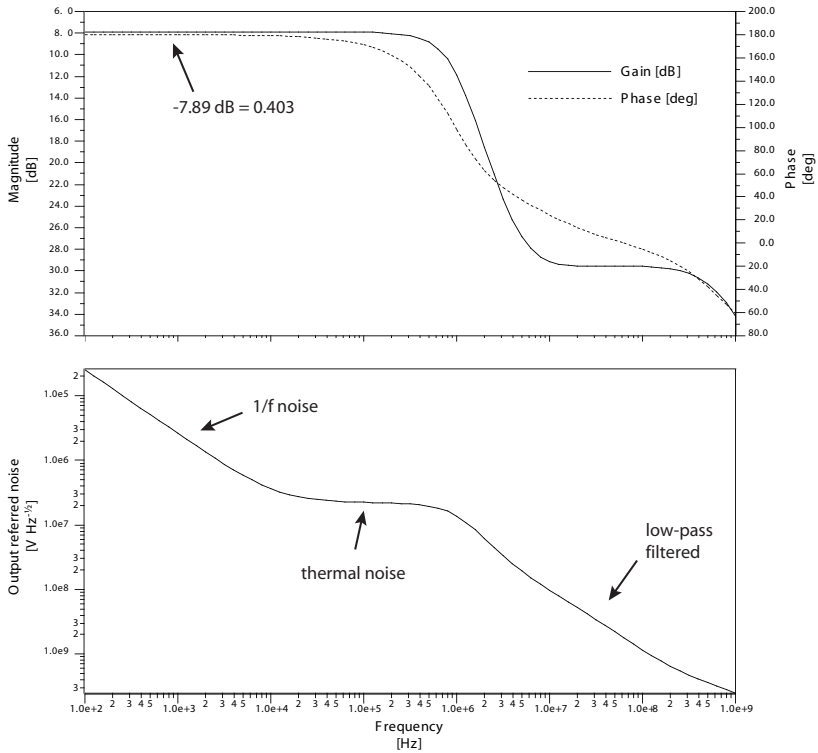


Figure 5.12: AC and noise analysis of the demodulation stage. The attenuation is 0.40 and corresponds to the capacitor ratio. The cut-off frequency is around 1 MHz i.e. the time constant is $\tau \approx 160$ ns allowing SC operation with settling times in the order of a microsecond. In the noise analysis flicker noise and thermal noise are easily distinguishable. The total noise with the specific timing is 0.32 mV including the kTC reset noise.

speed is less than 0.06 mV i.e. after 10 integration the accumulated error is less than half of the temporal noise (calculated with Eq. 5.11).

Charge injection

The channel charge injection of the switches into the switched capacitors in SC circuits typically introduces signal distortion because of the charge dependence on the signal level. The injection by the switch MrsINT for fast gate signals is given as $-1/2 \cdot WLC_{ox} \cdot$

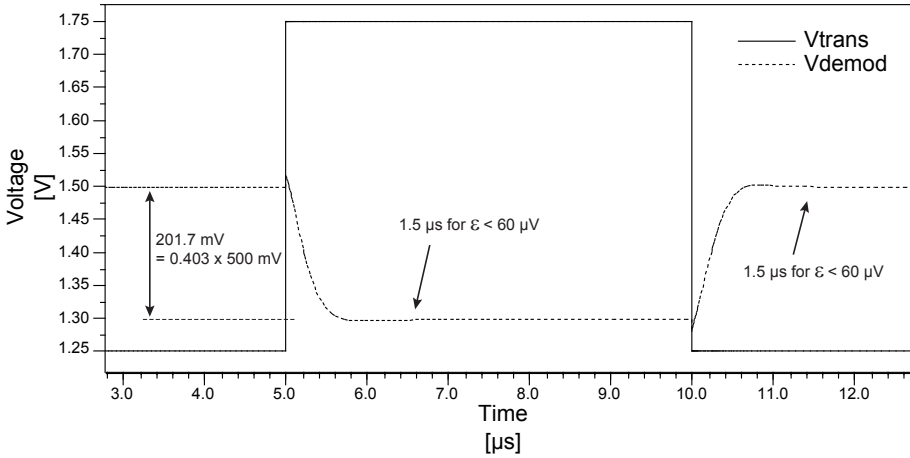


Figure 5.13: Simulation of the demodulation stage: A voltage step of 500 mV has been applied to the input voltage V_{trans} and produces a voltage drop of 201.7 mV at the output voltage V_{demod} , corresponding to the capacitor ratio attenuation factor $C_{sub}/C_{int}+C_{ovl}$. The voltage error becomes negligible compared to the total noise after a delay of 1.5 μ s.

($V_{high} - AGND - V_t$) causing a voltage rise of 36 mV in the signal V_{demod} . This is insignificant, since the effect is constant leading only to an additional signal offset that has to be corrected off-chip anyway. The situation is equivalent for the switches Msw1 and Msw2. The effect of the charge injection by the switch Msw3 depends on the input signal V_{trans} . On account of the subtraction, this should only lead to a small variation of the conversion factor $|V_{demod}/V_{trans}|$. To reduce the effect and the possible non-linear dependance, switches Msw1 and Msw2 are opened before opening Msw3, as can be seen in the timing diagram (Fig. 5.11). By doing so, the charge is injected towards the transducer buffer output instead of towards the basically infinite impedance capacitor node.

5.3.5 Pixel readout circuit

The pixel readout stage contains for both of the two mixer branches a sample and hold stage and an off-pixel buffer (see Fig. 5.14). The signal of the demodulation stage V_{demod} is stored in the sample and hold stage. Then the pixel starts the next demodulation sequence, while the pixel field is read out. The off-pixel buffer is a PMOS source follower. As in a conventional APS, the analog readout line is shared by all

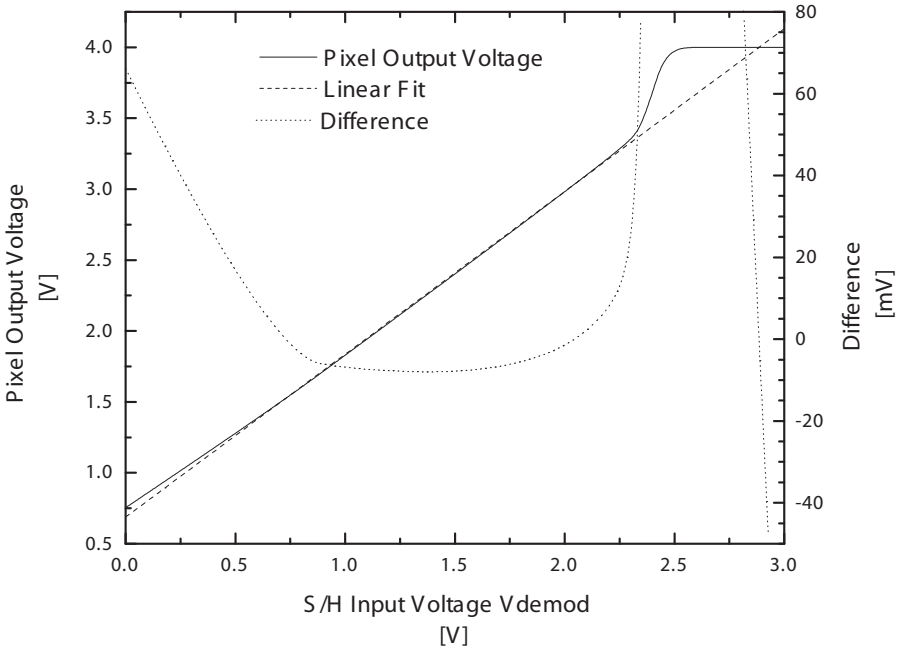


Figure 5.15: Simulation of the sample and hold stage and the pixel buffer: The linearity is better than 1% for an input range of 0.6 V to 2.2 V. At an output voltage of $V^{high-Vl/n} = 2.9$ V, the resistance of the switch M_{rd} increases rapidly, causing an increasing output voltage.

Speed, gain, and linearity of the readout circuit

The sample and hold stage and the PMOS follower have a gain of 1.16 due to the above described capacitive coupling. The linearity is better than 1% for an input range of 0.6 V to 2.2 V (see Fig. 5.15). This non-linearity leads to a dependence of the calculated modulation amplitude on the modulation phase. In theory, this could be corrected off-chip. Without correction, for very large modulation amplitudes with arbitrary phase relations, the measured peak amplitude SNR will be limited to 40 dB.

The settling time of the PMOS follower for large voltage steps is less than 400 ns.

5.3.6 Noise analysis and dimensioning of C_{sub} and C_{int}

The subtraction capacitor C_{sub} and the integration capacitor C_{int} have been sized maximally with respect to the available pixel area to contribute insignificant kTC sampling noise to the overall noise. Their ratio has been chosen in order to ensure photonic shot-noise limited operation above a certain illumination irradiance.

The transducer stage has a kTC reset noise of 0.23 mV and a thermal noise of 0.37 mV. The kTC noise of 0.37 mV due to the signal sampling onto the capacitor C_{sub} must also be taken into account. The Euclidian norm of these noise sources is the total electronic noise amounting to 0.57 mV.

In the noise analysis of the demodulation stage (see Fig. 5.12), the flicker or $1/f$ noise and the low-pass filtered white noise consisting of thermal and shot noise can clearly be distinguished. Flicker noise is reciprocally proportional to the frequency and mainly depends on the size of the devices. Shot noise in the case of transistors in weak inversion and thermal noise for transistors in strong inversion are reciprocally proportional to the transconductance and therefore reciprocally proportional to the current for weak inversion and to the square root for strong inversion. Size and current are both limited in the pixel. Since the integrator is reset after the time interval N/f_{Doppler} , it is sufficient to take only the noise integrating from about 5 kHz to infinity into account: the total noise is 0.24 mV, respectively 0.35 mV including the kTC reset noise.

The input referred noise of the pixel readout circuit is estimated to be 0.24 mV for the kTC sampling and for the thermal noise.

The overall electronic noise at the pixel output becomes, therefore

$$\sigma_{V_{\text{out}}}^2 = \left\{ 2N \cdot \sigma_{V_{\text{sample}}}^2 \cdot \left(\frac{C_{\text{sub}}}{C_{\text{int}} + C_{\text{ovl}}} \right)^2 + \sigma_{V_{\text{integrator}}}^2 + \sigma_{V_{\text{readout}}}^2 \right\} \cdot a_{\text{gain readout}}^2 \quad (5.11)$$

$$\sigma_{V_{\text{out}}} = 1.3 \text{ mV},$$

for a number of repetitions $N = 10$. The factor $2N$ is due to the fact, that for one demodulation sequence N samples are added and N are subtracted. The actual temporal noise was measured to be 2.4 mV, due to additional noise sources on the sensor and on the camera board, a fair agreement with the theoretical prediction.

The photonic shot-noise is given by the square root of the number of captured photo-generated charges. This leads to the following noise at the pixel output:

$$\sigma_{V_{\text{out,sn}}}^2 = 2N \cdot \overline{n_{\text{pe}^-}} \cdot \frac{q_e^2}{C_{\text{pn}}^2} \cdot \left(\frac{C_{\text{sub}}}{C_{\text{int}} + C_{\text{ovl}}} \right)^2 \cdot a_{\text{gain readout}}^2 \quad (5.12)$$

where $\overline{n_{pe}}$ is the mean number of photogenerated electrons during the integration time corresponding to a quarter demodulation period.

The capacitor ratio $C_{sub}/C_{int}+C_{ovl}$ has been chosen in order to obtain a photonic shot-noise of the same size as the electronic noise of the pixel for an optical power of 20 nW per photodiode*, i.e. a loss of 3 dB in *SNR* at this power and an insignificant loss at higher power. This limit is increased due to the electronic noise of the overall system to 70 nW per photodiode.

According to the simulation, the linear output swing is larger than 1.85 V. With a measured electronic noise of 2.4 mV, the maximum *SNR* of the sensor output signals *I* and *Q* becomes: $SNR_{IQ} = 20 \log_{10} (1.85 \text{ V}/2.4 \text{ mV}) = 57.7 \text{ dB}$ instead of 63.0 dB as predicted by the simulation of the sensor under ideal environmental conditions.

The maximum envelope amplitude *A* before saturation for an arbitrary phase corresponds to half of the total swing of *I* and *Q*. The standard deviation of *A* equals the noise of *I* or *Q* (see App. A.4). The *SNR* of the amplitude is therefore $SNR_A = 20 \log_{10} (A/\sigma_A) = 51.7 \text{ dB}$, if the non-linearity of the pixel follower is corrected. This is the dynamic range of the sensor and is not to be confused with the sensitivity.

5.3.7 Intensity mode

The chosen pixel architecture is very flexible and the different blocks are easily accessed by the control signals. This allows to use the pixel for other tasks than just for signal demodulation. An important requirement for the new pOCT sensor generation was an imaging mode that simplifies probe positioning. This new mode is the intensity imaging mode, in which the sensor is operated like a conventional grey level image sensor. This propriety is an enormous advantage for the alignment of the optical system and the probe handling.

For grey level imaging, just one branch of the pixel circuits, e.g. one discrete-time mixer, sample and hold, and readout buffer, is active. In the demodulation mode, the differences of optical signals integrated on the photodiode with delays equaling the half of the demodulation frequency are summed up. In the intensity mode, the differences between the signal integrated on the photodiode and the reset voltage are summed up. The timing diagram of the control signals is shown in Fig. 5.16. In contrast to the demodulation mode, this is a monotonous process. To avoid limitation of the voltage swing by the input PMOS transistor drain source saturation voltage of the OTA, the operation is chosen in a way to have a falling output for increasing

* Conditions: $\lambda = 820 \text{ nm}$, $f_{demod} = 50 \text{ kHz}$, $N = 10$

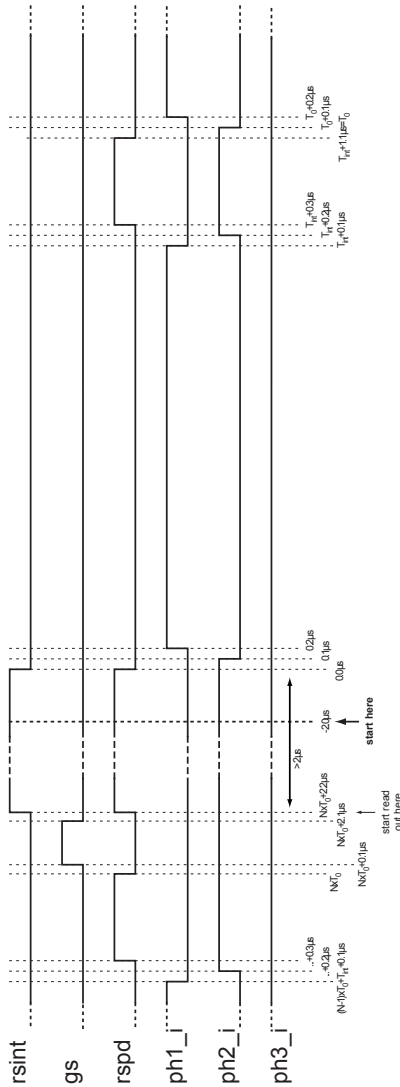


Figure 5.16: Timing diagram for the pixel control signals in the intensity mode. N is the number of repetitions.

illumination intensities. Therefore also the analog ground voltage is set to a higher level than in the demodulation mode, usually $AGND = 2.0V$. In order to obtain a

linear response and to distinguish also dark probe zones, the photodiode reset voltage is reduced to $V_{\text{reset}} = 2.275 \text{ V}$.

A dynamic range corresponding to the above mentioned output signal SNR is expected: $DR_{\text{intensity}} = 57.7 \text{ dB}$.

5.3.8 Pixel Layout

For the realization, a standard CMOS technology with $0.5 \mu\text{m}$ feature size, three metal layers, and poly-poly capacitors provided by AMIS Inc. has been chosen. This well-established but already relatively old technology is very advantageous in design kit and production costs, and availability, facilitating the prototyping process.

The horizontal pixel pitch was specified to be $50 \mu\text{m}$. With 10% fillfactor this leads to a vertical pitch of $86.3 \mu\text{m}$. Besides minimizing the size of the electronic circuit, it was important to minimize capacitive coupling to sensitive signals, especially on high-impedance nodes. Due to the very high illumination power, light shielding is crucial but also quite difficult due to the limited number of metal layers and the large number of control signals and references. Matching rules such as identical design, orientation, and current flow direction, common centroid, covering with the same potential (better is no covering, which is impossible due to the need for light shielding), no use of short channel devices, etc. have been followed wherever possible, to reduce mismatch in the OTAs and between the two output signals [41].

In the layout the main circuit blocks are easily distinguishable (see Fig. 5.17): the photodiode, the current source of the offset compensation circuit, the photodiode voltage follower, twice the capacitors C_{sub} and C_{int} , the two OTAs, the two readout signal storage nodes, the two pixel followers, and the many switches. The OTAs and the capacitors occupy most of the pixel area. The layers metal 2 and metal 3 are not shown for visibility reasons. A lot of the area on metal 2 is consumed by the large number of horizontal signal lines.

Using a more aggressive deep sub-micron CMOS process will essentially reduce the area consumption of the switches and the control signal lines. The size of the capacitors, chosen in order to minimize kTC reset noise, can only be reduced if the relative capacitance is increased. The used process features already a rather large poly-poly capacitance of $1.1 \text{ fF}/\mu\text{m}^2$. The size of the OTAs is determined by the speed and the gain, and by the flicker noise. A more advanced process will feature higher gains and speeds but the flicker noise will not improve.

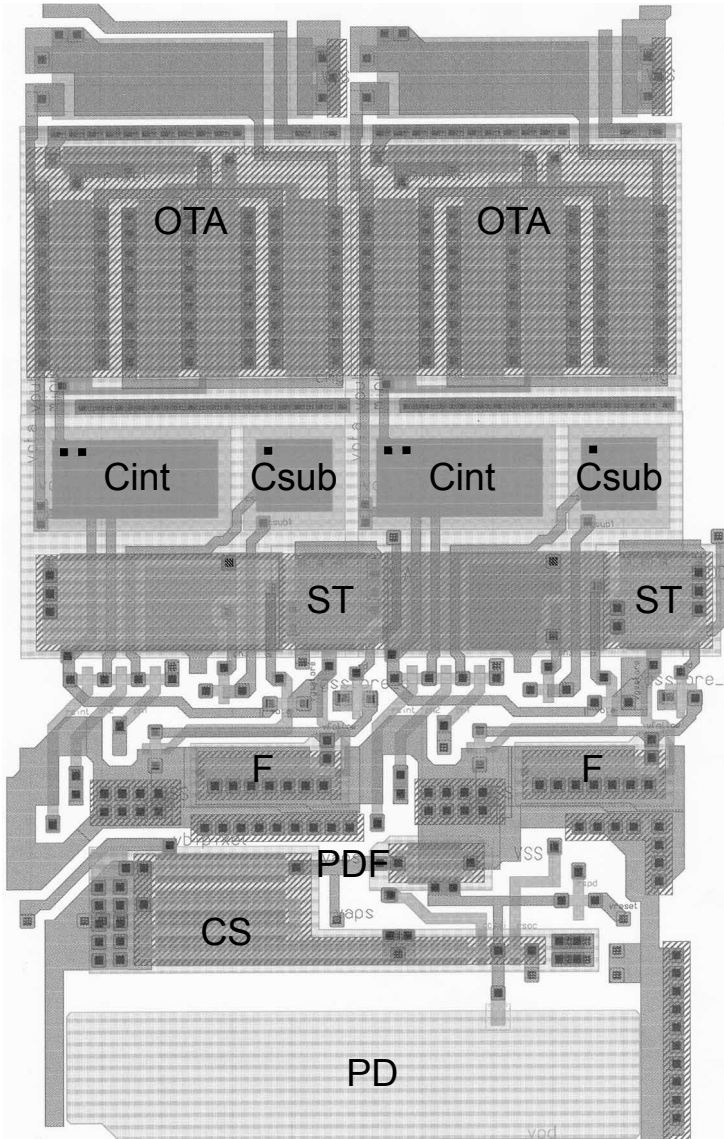


Figure 5.17: Layout of the smart pixel in a conventional 3M2P 0.5 μm CMOS process: the main blocks are the photodiode (PD), the current source of the offset compensation circuit (CS), the photodiode voltage follower (PDF), twice the capacitors Csub and Cint, the two OTAs, the two readout signal storage nodes (ST), the two pixel followers (F), and the many switches.

Bibliography

- [1] K. G. Larkin, "Efficient nonlinear algorithm for envelope detection in white light interferometry," *J. Opt. Soc. Am. A*, vol. 13, pp. 832–843, Apr. 1996.
- [2] S. S. C. Chim and G. S. Kino, "Three-dimensional image realization in interference microscopy," *Appl. Opt.*, vol. 31, pp. 2550–2553, May 1992.
- [3] M. D. Kulkarni and J. A. Izatt, "Digital signal processing in optical coherence tomography," in *Coherence Domain Optical Methods in Biomedical Science and Clinical Applications* (V. V. Tuchin, H. Podbielska, and B. Ovrzyn, eds.), vol. 2981 of *Proc. SPIE*, pp. 2–6, May 1997.
- [4] R. Windecker, M. Fleischer, B. Franzer, and H. J. Tiziani, "Two methods for fast coherence tomography and topometry," *J. Mod. Optics*, vol. 44, pp. 967–977, 1997.
- [5] L. Blanchot, M. Lebec, E. Beaurepaire, P. Gleyzes, A. C. Boccara, and H. Saint-Jalmes, "Low-coherence in-depth microscopy for biological tissue imaging: design of a real-time control system," in *Photon Propagation in Tissues III* (D. A. Benaron, B. Chance, and M. Ferrari, eds.), vol. 3194 of *Proc. SPIE*, pp. 198–204, Dec. 1997.
- [6] E. Beaurepaire, A. C. Boccara, M. Lebec, L. Blanchot, and H. Saint-Jalmes, "Full-field optical coherence microscopy," *Opt. Lett.*, vol. 23, pp. 244–246, Feb. 1998.
- [7] M. Willemin, N. Blanc, G. K. Lang, S. Lauxtermann, P. Schwider, P. Seitz, and M. Wány, "Optical characterization methods for solid-state image sensors," *Optics and Laser in Engineering*, vol. 36, pp. 185–194, 2001.
- [8] P. Seitz and N. Blanc, "CCD and APS/CMOS technology for smart pixels and image sensors," in *Detectors and Associated Signal Processing* (J. P. Chatard and P. N. J. Dennis, eds.), vol. 5251 of *Proc. SPIE*, pp. 142–153, Feb. 2004.
- [9] "Tesla vs. Marconi." U.S. Supreme Court Case #369, June 1943.
- [10] J. C. Bose, "Detector for electrical disturbances." US Patent 755 840, Mar. 1904.
- [11] P. K. Bondyopadhyay, "Sir J. C. Bose's diode detector received Marconi's first transatlantic wireless signal of december 1901 (The "Italian navy coherer" scandal revisited)," in *Proceedings of the IEEE, Volume 86, No. 1, pp. 259-285 (1998)*, pp. 259–285, Jan. 1998.
- [12] S. Bourquin, V. Monterosso, P. Seitz, and R. P. Salathé, "Video-rate optical low-coherence reflectometry based on a linear smart detector array," *Opt. Lett.*, vol. 25, pp. 102–104, Jan. 2000.
- [13] S. Bourquin, P. Seitz, and R. P. Salathé, "Optical coherence topography based on a two-dimensional smart detector array," *Opt. Lett.*, vol. 26, pp. 512–514, Apr. 2001.
- [14] M. Ducros, M. Laubscher, B. Karamata, S. Bourquin, T. Lasser, and R. P. Salathé, "Parallel optical coherence tomography in scattering samples using a two-dimensional smart-pixel detector array," *Opt. Commun.*, vol. 202, pp. 29–35, Feb. 2002.

- [15] M. Laubscher, M. Ducros, B. Karamata, T. Lasser, and R. Salathe, "Video-rate three-dimensional optical coherence tomography," *Opt. Express*, vol. 10, pp. 429–435, May 2002.
- [16] V. X. D. Yang, M. L. Gordon, B. Qi, J. Pekar, S. Lo, E. Seng-Yue, A. Mok, B. C. Wilson, and I. A. Vitkin, "High speed, wide velocity dynamic range Doppler optical coherence tomography (Part I): System design, signal processing, and performance," *Opt. Express*, vol. 11, pp. 794–+, July 2003.
- [17] B. H. Park, M. C. Pierce, B. Cense, and J. F. de Boer, "Real-time multi-functional optical coherence tomography," *Opt. Express*, vol. 11, pp. 782–793, 2003.
- [18] B. E. Bouma and G. J. Tearney, *Handbook of Optical Coherence Tomography*. New York: Marcel Dekker Inc, 2002.
- [19] J. E. Volder, "The CORDIC Trigonometric Computing Technique," *IRE Trans. Electronic Computers*, vol. 8, pp. 330–334, Sept. 1959.
- [20] R. Andraka, "A survey of CORDIC algorithms for FPGA based computers," in *FPGA '98: Proceedings of the 1998 ACM/SIGDA sixth international symposium on Field programmable gate arrays*, (New York, NY, USA), pp. 191–200, ACM Press, 1998.
- [21] B. Gilbert, "A precise four-quadrant multiplier with subnanosecond response," *IEEE J. Solid-State Circ.*, vol. 3, pp. 365–373, Dec. 1968.
- [22] D. G. Reed, *The ARRL handbook for radio communications*. Newington: ARRL, the national association for amateur radio, 2003.
- [23] S. S. C. Chim and G. S. Kino, "Correlation microscope," *Opt. Lett.*, vol. 15, pp. 579–581, May 1990.
- [24] G. S. Kino and S. S. C. Chim, "Mirau correlation microscope," *Appl. Opt.*, vol. 29, pp. 3775–3783, Sept. 1990.
- [25] K. G. Larkin, "A self-calibrating phase-shifting algorithm based on the natural demodulation of two-dimensional fringe patterns," *Opt. Express*, vol. 9, pp. 236–253, May 2001.
- [26] D. X. Yang, B. A. Fowler, and A. El Gamal, "A Nyquist rate pixel level ADC for CMOS image sensors," in *Proc. IEEE 1998 Custom Integrated Circuits Conference*, pp. 237–240, May 1998.
- [27] A. V. Harton, M. I. Ahmed, A. Beuhler, F. Castro, L. M. Dawson, B. W. Herold, G. Kujawa, K. F. Lee, R. D. Mareachen, and T. J. Scaminaci, "High dynamic range CMOS image sensor with pixel level ADC and in-situ image enhancement," in *Computational Imaging III* (C. A. Bouman and E. L. Miller, eds.), vol. 5677 of *Proc. SPIE*, pp. 67–77, Mar. 2005.
- [28] B. A. Fowler, A. El Gamal, and D. X. Yang, "A CMOS area image sensor with pixel-level A/D conversion," in *ISSCC Digest of Technical Papers*, pp. 226–227, Feb. 1994.
- [29] C. Lai, Y. King, and S. Huang, "A 1.2V 0.25- μm clock output pixel sensor with

- wide dynamic range," in *Computational Imaging III* (C. A. Bouman and E. L. Miller, eds.), vol. 5677 of *Proc. SPIE*, pp. 47–54, Mar. 2005.
- [30] B. Pain, S. K. Mendis, R. C. Schober, R. H. Nixon, and E. R. Fossum, "Low-power low-noise analog circuits for on-focal-plane signal processing of infrared sensors," in *Infrared Detectors and Instrumentation* (A. M. Fowler, ed.), vol. 1946 of *Proc. SPIE*, pp. 365–374, Oct. 1993.
- [31] T. Dresel, G. Häusler, and H. Venzke, "Three-dimensional sensing of rough surfaces by coherence radar," *Appl. Opt.*, vol. 31, pp. 919–925, Mar. 1992.
- [32] K. G. Larkin, *Topics in Multi-dimensional Signal Demodulation*. PhD thesis, University of Sydney, 2001.
- [33] J. C. Wyatt, *Laser Focus*, p. 65, May 1982.
- [34] K. Creath, "Phase-measurement interferometry techniques," in *Progress in Optics*, vol. XXVI, E. Wolf (Ed.), Elsevier, 1988.
- [35] T. Oggier, M. Lehmann, R. Kaufmann, M. Schweizer, M. Richter, P. Metzler, G. Lang, F. Lustenberger, and N. Blanc, "An all-solid-state optical range camera for 3D real-time imaging with sub-centimeter depth resolution (SwissRanger)," in *Optical Design and Engineering* (L. Mazuray, P. J. Rogers, and R. Wartmann, eds.), vol. 5249 of *Proc. SPIE*, pp. 534–545, Feb. 2004.
- [36] B. Büttgen, T. Oggier, R. Kaufmann, P. Seitz, and N. Blanc, "Demonstration of a novel drift field pixel structure for the demodulation of modulated light waves with application in three-dimensional image capture," in *Three-Dimensional Image Capture and Applications VI* (B. D. Corner, P. L, and R. P. Pargas, eds.), vol. 5302 of *Proc. SPIE*, pp. 9–20, Apr. 2004.
- [37] S. Beer, P. Zeller, N. Blanc, F. Lustenberger, and P. Seitz, "Smart pixels for real-time optical coherence tomography," in *Three-Dimensional Image Capture and Applications VI* (B. D. Corner, P. Li, and R. P. Pargas, eds.), vol. 5302 of *Proc. SPIE*, pp. 21–32, Apr. 2004.
- [38] S. G. Chamberlain and J. P. Y. Lee, "A novel wide dynamic range silicon photodetector and linear imaging array," *IEEE J. Solid-State Circ.*, vol. 19, pp. 41–48, Feb. 1984.
- [39] O. Vietze and P. Seitz, "Image sensing with programmable offset pixels for increased dynamic range of more than 150 dB," in *Solid State Sensor Arrays and CCD Cameras* (C. N. Anagnostopoulos, M. M. Blouke, and M. P. Lesser, eds.), vol. 2654 of *Proc. SPIE*, pp. 93–98, Mar. 1996.
- [40] B. Pain and E. R. Fossum, "A Current Memory Cell With Switch Feedthrough Reduction By Error Feedback," *IEEE J. Solid-State Circ.*, vol. 29, pp. 1288–1290, Oct. 1994.
- [41] A. Hastings, *The Art of Analog Layout*. New Jersey: Prentice-Hall, Inc., 2001.

Chapter 6

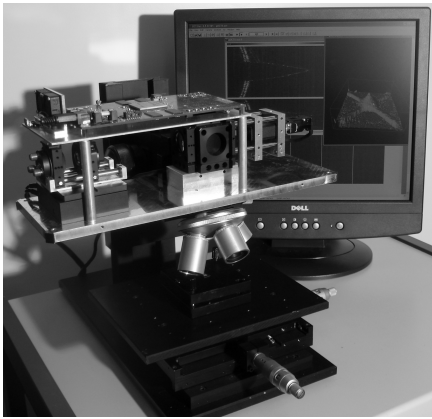
POCT System Realization

This chapter describes the main pOCT system that has been built as part of this work. The system consists of a high-speed image sensor based on the developed smart pixel architecture presented in the chapter above, a camera system for sensor control and data acquisition, software to view the data, a Linnik interferometer, and an optical path delay scanner together with its control electronics (see Fig. 6.1).

6.1 POCT high-speed image sensor

Some CMOS processes, such as the standard $0.5\ \mu\text{m}$, three metal, two poly process provided by AMIS Inc. used in this project, allow a large reduction in mask set costs if the layout occupies less than a quarter of the maximum mask size. This discount is due to the so-called multi-layer mask (MLM) technique that divides the number of generated masks by a factor four. To take advantage of this feature, the sensor has been designed to fit into a quarter reticle, e.g. the sensor occupies $9.15\ \text{mm} \times 9.49\ \text{mm}$ leaving an almost quadratic area of $7.200\ \text{mm} \times 7.767\ \text{mm}$ for an array of 144×90 pOCT smart pixels of the architecture presented in the chapter above.

The sensor frame rate requirement depends on the depth resolution and the axial scan speed of the reference mirror. For a typical scan speed of $20\ \text{mm/s}$ and an optical source featuring a depth resolution of $10\ \mu\text{m}$ (FWHM), $6\ \text{kframes/s}$ have to be acquired if three points per envelope are desired. The required data rate then amounts to more than $155\ \text{MS/s}$, since every pixel has two output values. The designed device therefore can be considered to be a high-speed image sensor [1–3]. It has been designed with eight



(a)



(b)

Figure 6.1: POCT system, with and without cover, consisting of a microscope body, the pOCT camera, the Linnik interferometer with the sample optics selection revolver, an SLD as illumination source, the axial scanner, the scanner driver (not shown), and the pOCT acquisition and viewer software.

analog output channels, and special high-speed readout techniques have been applied.

As already mentioned in Sec. 5.3, every pixel features a signal storage node for each of the two generated signals to be read out. In conventional CMOS imagers, this architecture is called global shutter because it allows starting and stopping of the optical signal integration for all pixels simultaneously. The main advantage of this architecture in our case is the fact that it allows to read out the pixel field values and at the same time to continue to demodulate and integrate the interferometric signal on the photodiode in order to generate the in-phase and quadrature signals of the next frame. This is indispensable to achieve high frame rates.

To avoid a time consuming additional row-preset time, the pixel field is split into a left and a right half, each with an individual row address decoder. These decoders are identical apart from the fact that their registers are sensitive on opposite edges of the row address clock (see Fig. 6.2). Therefore their row select signals are delayed with respect to each other by the time necessary to read out one half sensor row e.g. while the right half of a row is still being read out, the left half of the next row is being selected giving the pixel follower time to pre-charge the column amplifier of at least 900 ns, corresponding to the time needed to read out half of a row. Therefore the pixel field is read out continuously without any time interrupts inserted between the rows. To reduce the noise due to the half row switching, the power supply line of the pixel

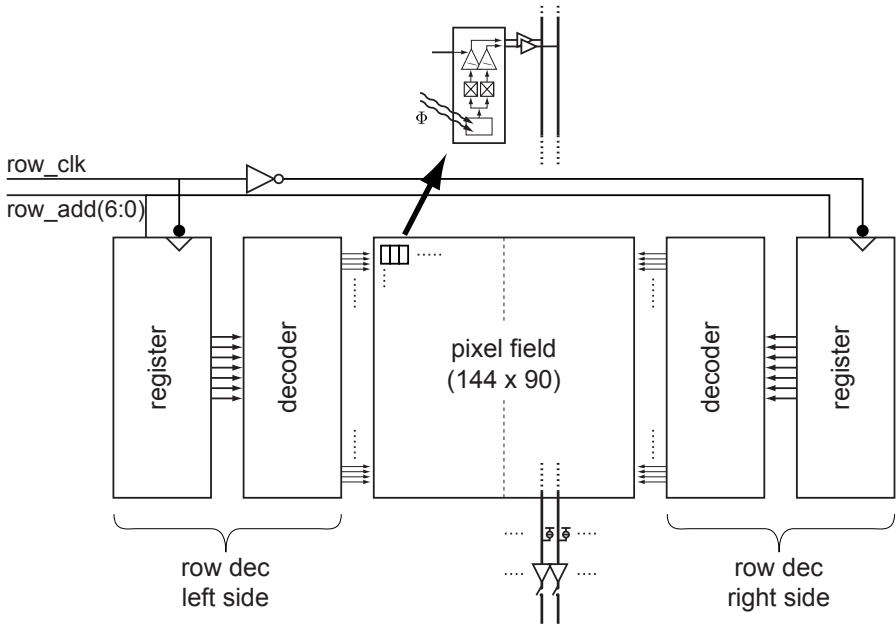


Figure 6.2: Schematic drawing of the row select signal generation and the pixel field: The pixel field and row decoder is split in two halves to avoid a time-consuming additional row-preset cycle and guarantee a pixel follower pre-charge time of 900 ns.

follower current source located at the bottom of the pixel field has also been split in two halves.

Similar pre-charging is applied in the second stage shown in Fig. 6.3. The 288 column drivers are multiplexed on four buses of eight analog channels each. The four higher bits (denoted g_4 to g_1 in the schematic) of the six bit column address are used to select a group of eight column outputs to be multiplexed to a bus. By the column address clock (clk_g), these four bits are transmitted through four-stage shift register, selecting the corresponding block with a certain delay in number of clocks. Fig. 6.3 illustrates the following example: If the address [0000] is set to the four higher column address bits, at the first rising edge, the signals of the columns 0 to 3 (in-phase and quadrature signals for each) are set to the eight channels of signal bus number 0. At the second edge, the columns 4 to 7 are connected to bus number 1, then 8 to 11 to number 2, and then 12 to 15 to number 4. Then the new address [0001] is applied to the registers connecting the columns 16 to 19 again instead of 0 to 3 to bus number 0 etc. Thus every bus is pre-charged during three cycles of the column address clock e.g. during 150 ns,

Description	Value	Comment
Imager size	9.15 mm × 9.49 mm	fitting the MLM size 9.17 mm × 9.49 mm
Number of pixels	144 × 90	
Number of analog values per pixel	2	
Pixel pitch	50 μm × 86.3 μm	
Pixel field size	7.2 mm × 7.767 mm	
Shutter mode	global shutter	
Output channels	8 analog taps	
Sample rate	20 MS/s	per channel continuous
Total sample rate	160 MS/s	
Maximum frame rate	6 kframes/s	with two values per pixel, featuring three amplitude values per OCT signal envelope (FWHM) 10 μm at 20 mm/s scan speed
Supply voltage pixel field	3.3 V	
Supply voltage read out circuitry	4.5 V	
Total power consumption	~ 225 mW	analog power supplies only, digital negligible

Table 6.1: POCT smart sensor parameter specification

before its eight channels are multiplexed to the eight output drivers. The two lower bits of the column address denoted *am1* and *am0* in the illustration control this last multiplexer.

The maximum achievable output driver pixel rate in the used process is around 30 MS/s for true 10 bit operation and a typical external capacitive load of 10 pF. For symmetry reasons, the sensor has been designed with eight taps with a pixel rate of 20 MS/s each, moderately relaxing the design constraints.

The operational amplifiers in the drawings of this section are PMOS Miller operational transconductance amplifiers (OTA). In order to preserve the output range of the PMOS

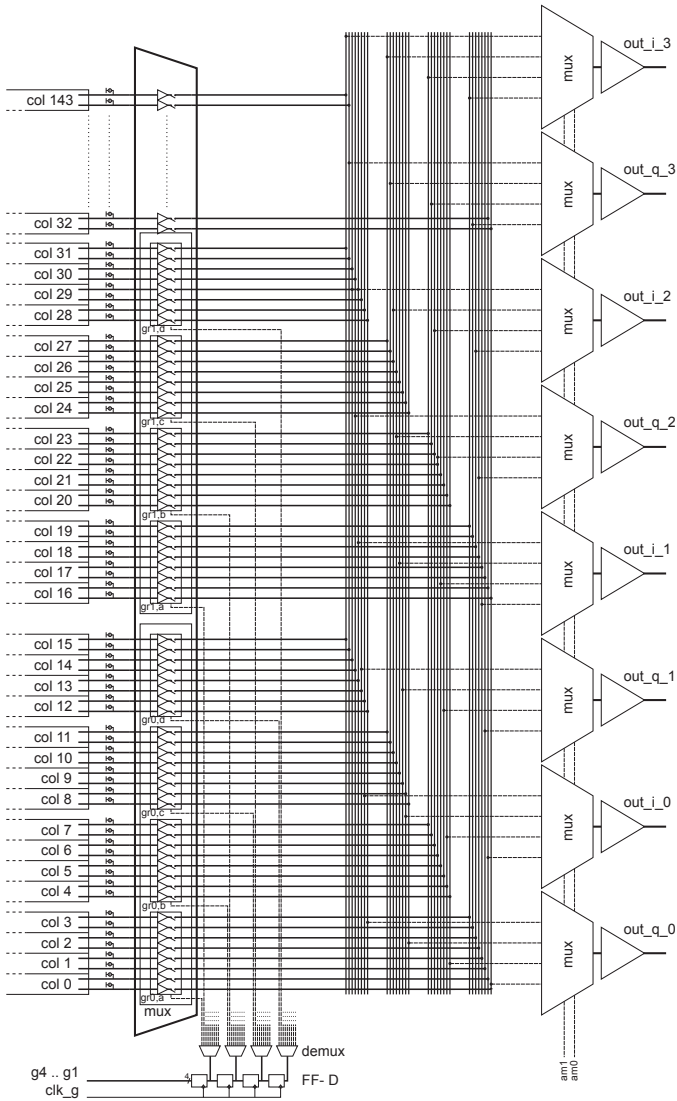


Figure 6.3: Schematic illustrating the analog column readout path: A multiplexing structure with four intermediate buses of eight channels each allows pre-charging of the analog channels to save power and time.

pixel follower, the supply voltage of these OTAs has been raised from the nominal supply voltage of this technology of 3.3 V in the pixel field to 4 V. The technology allows with some layout constraints supply voltages up to 5 V at the cost of a degrading noise performance.

6.2 High-speed data acquisition and system control electronics

6.2.1 POCT camera

It is crucial that the data acquisition system maintains the high sensor frame rate of up to 6 kframes/s over the time of one three dimensional volume acquisition, e.g. for more than 300 two-dimensional frames in a sequence. An overview schematic of the electronics in the pOCT system with emphasis on the camera is shown in Fig. 6.4. The camera consists, apart from the smart pixel imager, of an FPGA controlling the data streams, an analog-to-digital converter (ADC), two RAM blocks of 256 Mbit each, and a USB transceiver chip.

The ADC has eight channels of 10 bit each to convert the eight analog sensor output signals. Its conversion factor is 2.431 mV/DU . While a new three-dimensional frame is acquired and written to one RAM block, the last frame stored in the other block is sent via USB 2.0 to the computer. A first optional FPGA block between data acquisition and memory storage removes the signal offset and a second one applies a pipelined CORDIC algorithm to convert the in-phase and quadrature signal directly to envelope amplitude and phase values.

Because of the limited bandwidth of the USB 2.0 connection of around 40 MB/s data stream, the 3D frame rate is reduced to a few Hertz although the acquisition of a typical frame only takes some ten milliseconds. A third optional FPGA block still under development applies a simple lossless data compression algorithm based on Huffman coding in order to increase the frame rate.

The camera and the axial scanner are synchronized by a trigger signal to start a 3D frame. The scanner is the master because the timing of the signal acquisition is easier to control than the position of the scanner.

6.2.2 Software for POCT data acquisition and viewing

The software for this project consist of a USB camera driver based on the open source project `usb-lib`, and a front end to control the camera registers, acquire, decode, view,

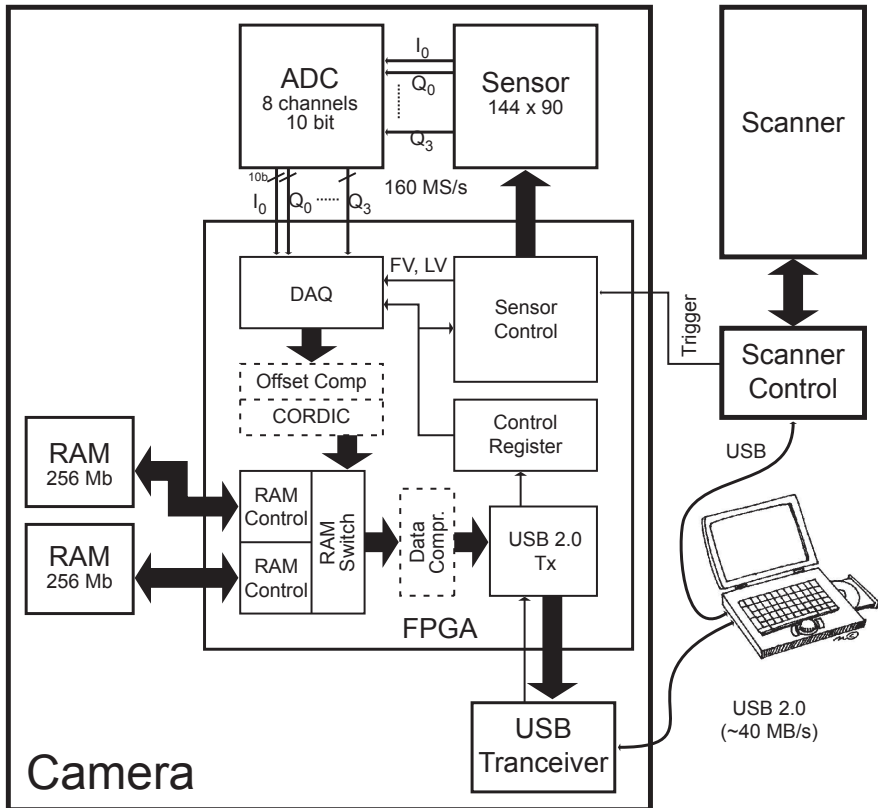


Figure 6.4: Overview of the electronic part of the pOCT system and especially the camera board: The camera, housing the pOCT smart sensor, contains an FPGA as main unit controlling the sensor and the data streams between sensor, RAMs, and PC interface.

and save the data representing the volumetric images. It is written in C++ and runs on any recent MS Windows version. Not only slices representing the signal amplitude or phase in the XZ, YZ, and XY plans can be viewed but also a three-dimensional data cloud representation as well as the fitted surface of the sample. By opening the grey-level imaging window, the needed camera control signals are generated.

A filter allows to import the acquired and saved pOCT data into Matlab for further analysis.

6.2.3 Axial scanner

Different axial scanners have been used to change the length of the reference path. Two types developed at CSEM SA based on a flexure technique allowed to move a reference mirror with a high precision. All measurements shown in this work have been acquired with a system using the scanner V106 from Physik Instrumente (PI) GmbH. Its actuator is a voice coil and the position feedback is based on an incremental linear encoder. It allows to mount not only the reference mirror but also imaging optics on the moving table up to a total weight of 100 g. The resolution of the encoder is interpolated to 100 nm. With a total travel range of 6 mm, the repeatability of positioning the table is specified to be better than 200 nm. The maximum speed is 50 mm/s. The scanner therefore fits the pOCT system's needs of 1 – 3 mm depth range at 20 mm/s scan speed. As for most of the commercially available translation stages, this scanner's controller was rather developed to rapidly move to a very precise position with a high repeatability and keep this position with a high accuracy. It has not been optimized for high scan-speed precision as required in our case (see Sec. 4.4). Therefore we have developed a scanner controller based on the DSP development kit TMS320C6713 DSK from Texas Instruments Inc. With an algorithm developed as relatively simple PID controller in Matlab, much better performance was measured in the pOCT system than with the original scanner driver.

The scanner controller algorithm parameters can be written to an on-board flash by a USB connection, thus the scanner serves also as a stand-alone unit. During operation, one of two predefined scan speeds is selected by an external switch.

6.3 Optical set-up

The whole system except for the scanner driver and the computer has been integrated into a microscope-like pOCT demonstrator. The Linnik interferometer, on which it is based, consists of a beam splitter that sends the light from the illumination source into the two interferometer arms, imaging optics in the two arms, and a reference mirror mounted on the axial scanner in the reference arm, as shown in Fig. 6.5. The smart pixel pOCT sensor is positioned at the interferometer output, where the sample image is formed.

The optical design had two requirements: the magnification factor between the sample and the image formation on the sensor must be selectable in a certain range, e.g. 1:2 to 1:6, and the use of spatially coherent as well as incoherent light sources must be guaranteed. To retain as much optical power in the system as possible also in case

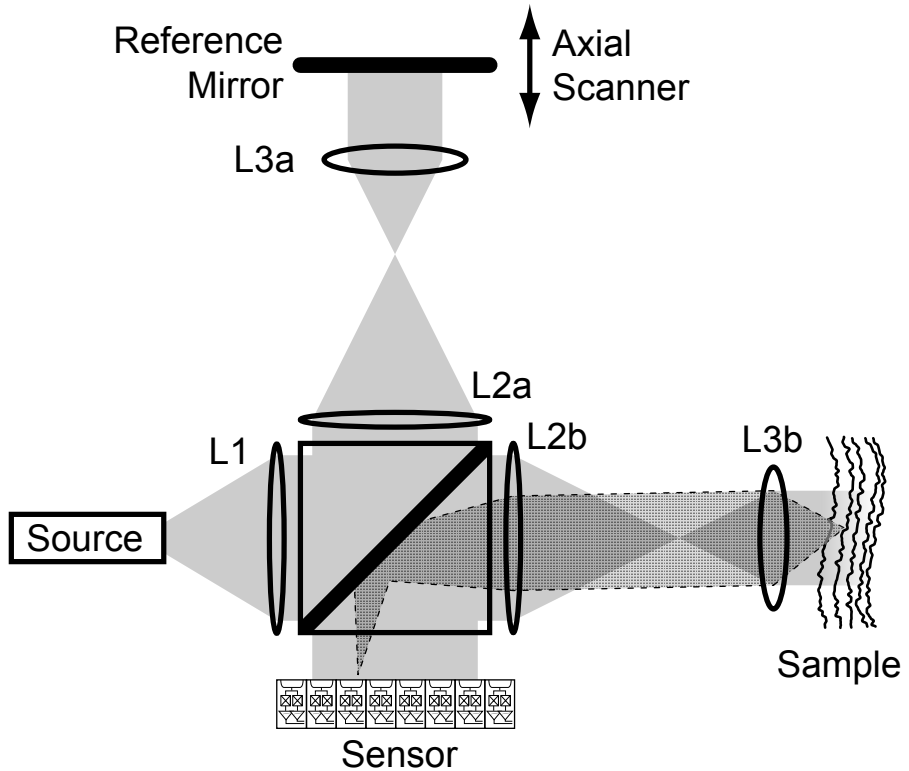


Figure 6.5: Optical set-up of the pOCT demonstrator: Linnik interferometer with illumination source, collimation optics (L1), beam splitter, imaging optics (L3a/b to L2a/b), and smart pixel sensor.

of incoherent sources such as light emitting diode (LED) arrays, the optical distances have been chosen as small as possible. This is the reason for placing the second imaging lens (L2) on the sample respectively the reference arm side of the beam splitter instead between splitter and sensor as usual. Spatially incoherent illumination sources are often chosen because of the cost-efficiency and, especially, to reduce the optical crosstalk when imaging tomographic samples, as mentioned in Chap. 3. For optimum crosstalk rejection an imaged volume defined by the optical resolution limit must match the coherence volume given by the Van Cittert-Zernike theorem $A_c = \lambda^2/\Omega$, where Ω denotes the solid angle. This is guaranteed if the entrance pupil of the sample objective is filled with spatially incoherent light e.g. if the objective aperture defines the entrance pupil of the illumination system as shown by Karamata [4,5].

The lenses L2a and L2b are achromats with a focal length of 60 mm and a diameter of 27 mm. They are at the focal distance to the pOCT sensor. The lens 3a is biconvex and features 16 mm focal length. If it is placed on the same moving table as the reference mirror, the influence of a tip-tilt error of the mirror is reduced. Three different lenses are set into a microscope objective selection revolver and serve as lens L3b. They have focal distances of 25 mm, 16 mm, and 10 mm, where the last one actually is composed of two lenses of 20 mm focal distance put together. They are all biconvex with 23 mm diameter. A magnification factor of 2.5, 3.75, and 6.0 leading to an imaged sample area of $2.9 \text{ mm} \times 3.1 \text{ mm}$, $1.9 \text{ mm} \times 2.0 \text{ mm}$, and $1.2 \text{ mm} \times 1.3 \text{ mm}$ respectively can be selected. The lateral resolution e.g. the corresponding pixel spacing on the sample ranges from $8 \mu\text{m}$ to $20 \mu\text{m}$ in the X direction, which is larger than the theoretical optical resolution would allow. Even though biconvex lenses suffer from spherical aberration degrading the numerical aperture NA , they have been chosen due to the larger diameter increasing the amount of captured light backscattered from the sample and also because the optical resolution cannot be exploited due to the sensor pixel size. With a theoretical numerical aperture of $NA = \sin(\arctan(D/2f)) \sim 0.4$, the depth of focus corresponding to the axial depth range $Z = \pi\lambda/2NA^2$ is in the micrometer range. A telecentric design, e.g. an additional diaphragm in the sample arm would increase the theoretical depth range at the cost of a very large loss in optical power reflected from the sample. If samples of much larger depth ranges are imaged, a loss in lateral resolution is noticed in out-of-focus positions.

Three different types of illumination sources have been used: several LED arrays, a superluminescent diode (SLD), and a mode-locked femtosecond laser. The results are described in the next chapter.

The SLD used for most of the measurements is an SLD-380-HP1 from Superlum Diodes Ltd. and features a center wave length of 821 nm and a FWHM spectral bandwidth of 19 nm, leading to a theoretical FWHM depth resolution of $15.4 \mu\text{m}$. The maximum optical output power is around 30 mW. The SLD is temperature controlled, and the driver ensures operation without current peaks that could damage the device.

6.4 Conclusion

A complete high-speed pOCT system has been developed, consisting of the high-speed custom-design pOCT sensor based on the smart pixel architecture, the camera electronics, the illumination source, the Linnik interferometer, the reference path scanner and its driver, the microscope body, and the software. Each component, with the exception of the scanner and the illumination source, has been specifically developed for

this project. The system is optimized for high-speed TD-OCT imaging. The volume acquisition speed, given by the scanner speed $v_{\text{typical}} = 20 \text{ mm/s}$ times the lateral resolution 144×90 pixel, is to our knowledge the fastest TD-OCT system that has ever been described [6].

Bibliography

- [1] S. Lauxtermann, G. Israel, P. Seitz, H. Bloss, J. Ernst, H. Firla, and S. Gick, "A megapixel high speed CMOS imager with sustainable Gigapixel/sec readout rate," in *Proceedings of the workshop on charge-coupled devices and advanced image sensors*, (Lake Tahoe, USA), June 2001.
- [2] F. Lustenberger, M. Lehmann, L. Cavalier, N. Blanc, W. Heppner, J. Ernst, S. Gick, and H. Bloss, "A colour 3200 fps high-speed CMOS imager for endoscopy in biomedical applications," in *Proceedings of the 30th European Solid-State Circuit Conference ESSCIRC*, (Leuven, Belgium), Sept. 2004.
- [3] P. Donegan, E. Fox, B. Li, M. Sonder, F. Feng, M. Kiik, and S. Xie, "A 4m pixel image sensor for high speed image capture," in *Proceedings of the workshop on charge-coupled devices and advanced image sensors* (E. Fossum, A. Theuwissen, and N. Teranishi, eds.), (Karuzawa, Nagano, Japan), pp. 185–188, June 2005.
- [4] B. Karamata, P. Lambelet, M. Laubscher, R. P. Salathé, and T. Lasser, "Spatially incoherent illumination as a mechanism for cross-talk suppression in wide-field optical coherence tomography," *Opt. Lett.*, vol. 29, pp. 736–738, Apr. 2004.
- [5] B. Karamata, *Multiple scattering in wide-field optical coherence tomography*. PhD thesis, École Polytechnique Fédérale de Lausanne, 2004.
- [6] J. Szydlo, N. Delachenal, R. Giannotti, R. Wälti, H. Bleuler, and R. P. Salathé, "Air-turbine driven optical low-coherence reflectometry at 28.6 kHz scan repetition rate," *Opt. Commun.*, vol. 154, pp. 1–4, 1998.

Chapter 7

POCT measurements and system performance

This chapter describes the measurements to determine the performance of the developed pOCT pixel architecture and to compare it to the theory. Isolated pixel performance measurements are impossible since the experiment is always influenced by the behavior of the total system. To reduce external influences, the sensor has been tested by direct illumination by a modulated illumination source in previous work [1]. All measurements in this chapter have been acquired with the system described in Chap. 6 occasionally slightly modified.

7.1 Sensitivity measurements

The sensitivity of an OCT system describes the smallest detectable power reflection coefficient in a sample. As already derived in Sec. 2.2, it is proportional to the optical power per pixel illuminating the sample and proportional to the integration time per sample, i.e. reciprocally proportional to the scan speed and proportional to the depth spacing of the samples.

The sensitivity performance of different OCT system is usually compared by either the use of a sample with known reflectivity or by imaging of typical OCT samples such as the retina. The use of a calibrated sample allows the comparison of the theoretical sensitivity of the system to its real performance.

7.1.1 Experimental set-up

Two different types of experiments were performed:

1. Measurement of the sensitivity of the total system described in Chap. 6
2. Measurement of the maximum sensitivity of the pixel architecture with a femtosecond laser type Mira 900-F

The interferometer described in the chapter above was used. The sample was replaced by a mirror and a neutral density filter with a power transmittance T_f measured at the illumination source spectrum, simulating a sample with a reflectivity $R_s = T_f^2$ (see Fig. 7.1).

For the second and third experiment, the lens L1 used to adjust the beam collimation has been modified in focal length and position in order to illuminate only a very small sample area corresponding to a few pixels on the sensor, and therefore increase the optical power per pixel, since the pixel architecture and not the overall system performance was of interest.

In the second experiment a neutral density filter of $T_{of} = 10^{-0.5}$ was placed in the reference arm in order to reduce the overall optical power on the sensor, avoiding saturation of the in-pixel offset compensation circuit.

7.1.2 Data processing

The theoretical sensitivity for the TD-pOCT system with smart pixels of our type in the case of 100% reference arm reflectivity is calculated as

$$S_{\text{theory}} = \frac{1}{R_{s_c, \text{min}}} \simeq \frac{16}{\pi^2} \cdot \frac{\eta P_{\text{pd}} T}{hc/\lambda_0}, \quad (7.1)$$

as seen from Chaps. 2 and 4, where η is the quantum efficiency of around 0.3 at $\lambda_0 \simeq 820$ nm peak wavelength, and P_{pd} is the optical power on the photodiode of a pixel coming from the sample arm if a sample of 100% reflectivity is assumed. If the reference arm is not attenuated, this corresponds to the optical power per photodiode coming from the reference arm. T is the integration time per sample and corresponds to $T = N/f_D = N \cdot \lambda_0/2v$, as seen from Chap. 5, where N is the number of periods over which averaging is done and v is the scan speed.

This theoretical sensitivity is reduced by 3 dB if pixel-level offset compensation (OC) is used due to the additional shot-noise of the offset current. If the assumption stated

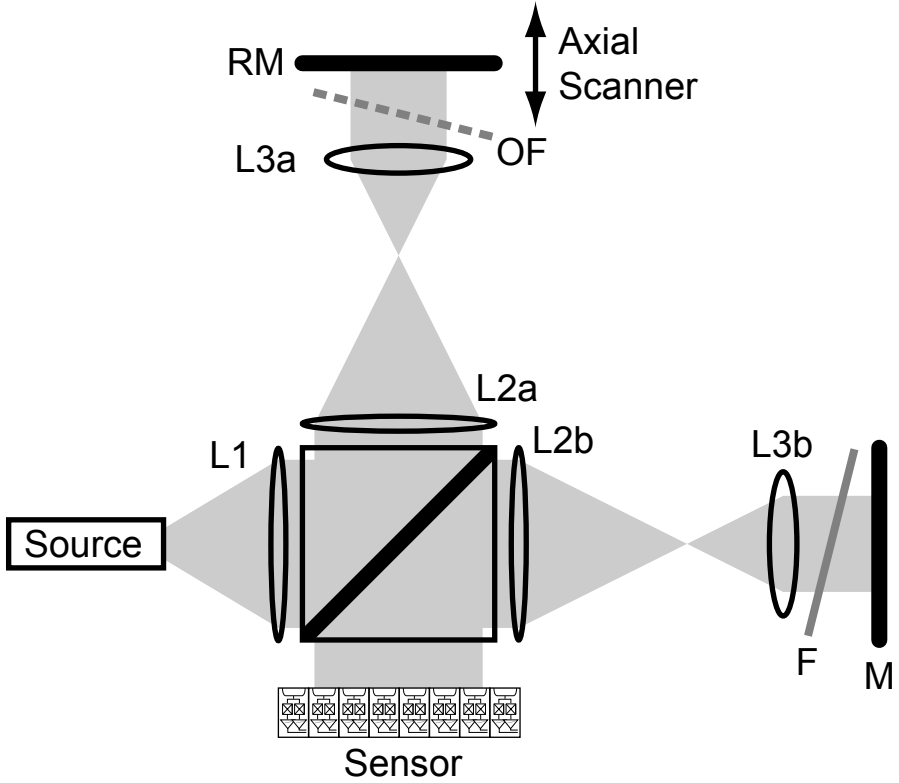


Figure 7.1: Optical set-up of the pOCT system and pixel performance measurements: The interferometer presented in Chap. 6 was used. The sample consists of a mirror (M) and a neutral density filter (F) of measured transmittance. For some measurements, lens L1 was modified and a second optional neutral density filter (OF) was placed in the reference arm to avoid sensor saturation.

in Chap. 2 that the relative intensity noise of broadband illumination sources is negligible, does not hold anymore (in the case of a very strong reference arm power), the sensitivity in the case of OC becomes

$$S_{\text{theory}} \simeq \frac{16}{\pi^2} \cdot \frac{\eta P_{\text{pd}} T}{hc/\lambda_0} \cdot \frac{1}{2 + \frac{1 + \Pi^2}{2} \cdot \frac{\eta P_{\text{pd,a}} \tau_c}{hc/\lambda_0}}, \quad (7.2)$$

where P_{pd} is the optical power on the photodiode without attenuating the reference arm, and $P_{\text{pd,a}}$ is the optical power on the photodiode during the measurement, i.e.

which a neutral density filter in the reference arm (for detailed calculations see Sec. A.3). Π denotes the degree of polarization.

Measuring the sensitivity in the experiment corresponds to measuring the SNR of the detected envelope amplitude and the power reflectance of the sample. The sensitivity is then given as

$$S_{\text{meas}}[\text{dB}] = SNR_{\text{meas}}[\text{dB}] + 10 \log_{10} (1/R_s) \tag{7.3a}$$

$$= SNR_{\text{meas}}[\text{dB}] - 20 \log_{10} (T_f), \tag{7.3b}$$

as commonly stated [2].

In our case the envelope amplitude is given as

$$A = \sqrt{A_I^2 + A_Q^2}, \tag{7.4}$$

where A_I and A_Q are the in-phase and quadrature signals given by the sensor output voltage of which the mean value has been subtracted.

Due to a very limited matching of the scan position and two-dimensional frame acquisition, the interferogram and therefore also the measured amplitude at a certain position in the acquired data varies from 3D scan to 3D scan. Therefore it is not useful to calculate the SNR from a series of measured amplitude values at a certain sampling depth position. The SNR is rather measured as the maximum envelope amplitude of a scan A_{max} compared to the noise of the amplitude. This noise is measured in a part of the interferogram where no interference occurs, e.g. where the signals A_I and A_Q are close to zero. But even for these input signals, due to the noise and the rectifying character of Eq. 7.4, the measured amplitude there is not zero on average. For the same reason, the theoretical standard deviation of the amplitude is smaller there than the standard deviation for non-zero in-phase and quadrature signals. It can be shown that the standard deviation of the envelope for non-zero input signals corresponds to the standard deviation of A_I and A_Q at any position:

$$\sigma_A \Big|_{A_I, A_Q \neq 0} = \sigma_{A_I, Q}, \tag{7.5}$$

if $\sigma_{A_I} = \sigma_{A_Q}$ (see Appendix A.4). For practical reasons, the following equation has been chosen to calculate the SNR from an experiment

$$SNR_{\text{meas}} = \frac{A_{\text{max}}^2}{\frac{\sigma_{A_I}^2 + \sigma_{A_Q}^2}{2}}, \tag{7.6}$$

where σ_{A_I} and σ_{A_Q} are the standard deviations calculated from the signal values of A_I and A_Q over the first 32 2D frames of every volume acquisition. It has always been verified that no signal oscillation occurred on these first frames and that $\sigma_{A_I} \simeq \sigma_{A_Q}$.

7.1.3 Results and discussion

System performance with fully SLD illuminated pixel field

In this experiment, the sensitivity of the pOCT demonstrator with the SLD as illumination source has been measured with calibrated samples but without any other modification. The light source fully illuminates the pixel field. Nevertheless due to the Gaussian beam profile, the optical power and therefore the performance degrades slightly at the borders of the sensor. All measurements refer to an area located in the middle of the sensor.

The optical power coming from the reference arm with blocked sample arm was 22 nW per photodiode or around 3 mW on the total pixel field. This shows that from the illumination source's optical power of about 30 mW not only a factor 4 is lost due to the beam splitter but again a factor ~ 2.5 due to the Gaussian profile of the beam, the non-unitary aspect ratio of the beam, reflections in the system, and other non-idealities. With a scan speed $v = 20 \text{ mm/s}$, the peak wavelength $\lambda_0 = 820 \text{ nm}$, and the number averaged periods $N = 10$, the integration time per depth sample becomes $T = 205 \mu\text{s}$ and with a quantum efficiency of $\eta = 0.3$, the theoretical sensitivity is $S \simeq 69.6 \text{ dB}$. The sensitivity has been measured for three different neutral density filters. Without filter, the pixel output signals saturate. Tab. 7.1 shows the results.

The measurements show that the system is only 0.9 – 2.4 dB below the theoretical limit, which is a very satisfactory result. It could signify that the electronic noise corresponds to about 50 – 90 % of the photonic shot noise. Shot-noise limited operation was only expected for a three times larger optical power. Every experiment has been repeated with switched on and off pixel-level offset compensation. The optical power on the photodiode corresponds to a photocurrent of about $\overline{I_{el,0}} \simeq 4.4 \text{ nA}$. The offset compensation circuit only compensates for currents larger than about 10 nA and should be used for currents larger than 40 nA to avoid pixel saturation. This is the reason why no significant difference is noticeable between the measurements with OC and without.

Fig. 7.2 shows the acquired signals of one pixel over three subsequent depth scans with a calibrated sample of $10^{-2.11}$ power reflectance. The measured SNR is 46 dB. The calculated envelope amplitude has a FWHM of about 16 – 17 μm , close to the predicted depth resolution of 15 μm . The peak position jitter is much smaller than the

Sample Reflectance $R_s = T_f^2$	Amplitude SNR no OC	Amplitude SNR OC	OCT sensitivity no OC	OCT sensitivity OC
1	saturated signals, ≥ 53 dB			
$10^{-2.11}$	46.1 dB	45.7 dB	67.2 dB	66.8 dB
$10^{-3.50}$	33.7 dB	33.2 dB	68.7 dB	68.2 dB
$10^{-4.14}$	27.1 dB	25.9 dB	68.5 dB	67.3 dB

Table 7.1: Sensitivity measurement of the pOCT system, with three different neutral density filters in the sample arm and without filter. The optical power per photodiode was 22 nW leading to a theoretical sensitivity of 69.6 dB. The measured sensitivity is 0.9 – 2.4 dB smaller than predicted by the theory and independent of the sample reflectance in its linear range.

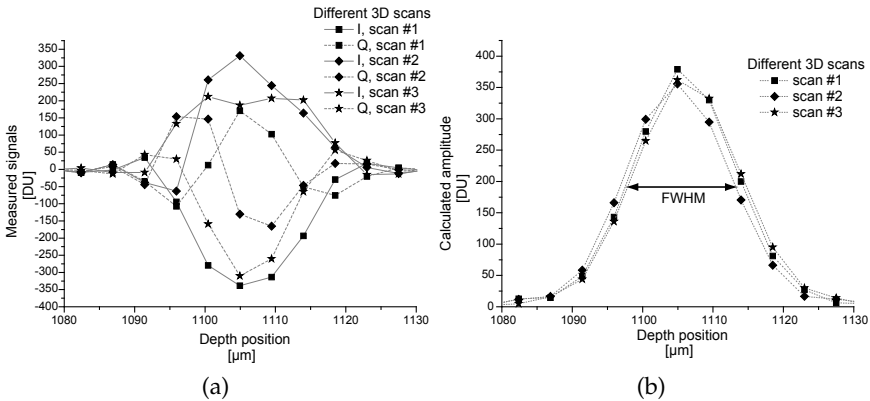


Figure 7.2: Comparison of the acquired in-phase A_I , quadrature A_Q , and envelope amplitude A signals of one pixel over three subsequent depth scans. The power reflectance in the sample path was $10^{-2.11}$ and an SNR of more than 46 dB has been measured. (a) shows the read out pixel values, (b) shows the calculated amplitude. The peak position jitter is much less than the depth spacing of 4.51 µm. The envelope FWHM is around 16 – 17 µm.

depth sampling $\Delta z = (N + 1) \cdot \lambda_0/2 = 4.51 \mu\text{m}$. From the in-phase and quadrature signals it can be seen that the phase does not stay constant for an envelope. This is due to a mismatch between Doppler and demodulation frequency, caused by a limited scan speed accuracy. If the phase is changing rapidly e.g. if there is a large phase shift during the averaging of one depth sample, the envelope amplitude is reduced leading

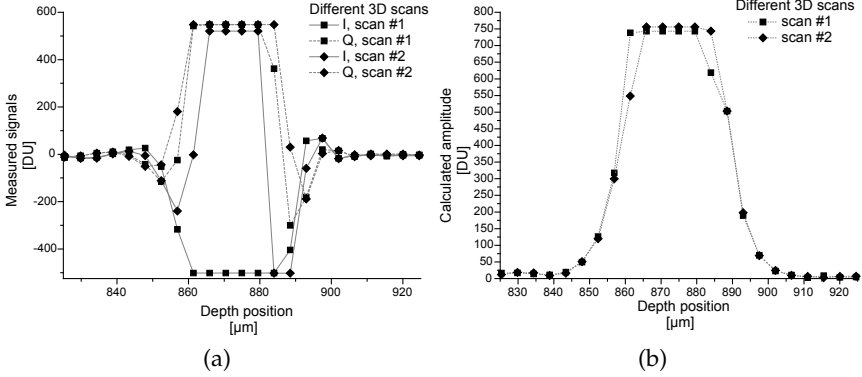


Figure 7.3: Measurement of a sample with 100 % power reflectance: (a) The pixel output signals A_I and A_Q saturate. (b) The peak of the calculated envelope amplitude is cut off. The reflectance is still detected but the depth resolution degrades.

to a reduced SNR as shown in Chap. 4.

With a sample of 100 % reflectivity, the pixel output signals A_I and A_Q saturate due to their limited dynamic range. The pixel-level offset compensation does not compensate for this effect, since not the photodiode but the opamps and the pixel drivers saturate. The offset compensation circuit avoids photo-transducer stage saturation due to a large constant signal offset. Fig. 7.3 illustrates the signal saturation effect. A_I and A_Q have slightly different saturation levels, probably due to some device mismatch on the pixel level or in the output path leading to a difference of the subtracted mean voltage. The measured $SNR \geq 53$ dB corresponds to the saturation of both output signals. But depending on the phase, signal distortion already occurs if one signal is saturating and the other is zero. The dynamic range of the system therefore becomes $DR \geq 50$ dB. This corresponds well to the predicted 51.7 dB calculated in Chap. 5. In the case of signal saturation, the surface is still detected, only the depth resolution is degraded, since the envelope peak is cut off. The resolution can be improved to about one depth sampling Δz by finding the center of gravity of the calculated envelope.

A dynamic range of $DR \geq 50$ dB signifies that for a given sensitivity S , defining the smallest detectable reflection $R_{s,\min}$, given by a certain optical power, integration time per depth sample, and wavelength, the largest reflection coefficient that is detectable without saturation is $R_{s,\max} = 10^5 \cdot R_{s,\min}$. With the parameters of this experiment, this leads to $R_{s,\max} = 0.014$. By combining Eqs. 2.12 and 2.15, the maximum modulation amplitude of the photocurrent becomes $I_{el,\text{mod}} \simeq 2 \sqrt{R_{s,\max}} \cdot \bar{I}_{el,0} \simeq 1.0$ nA in the

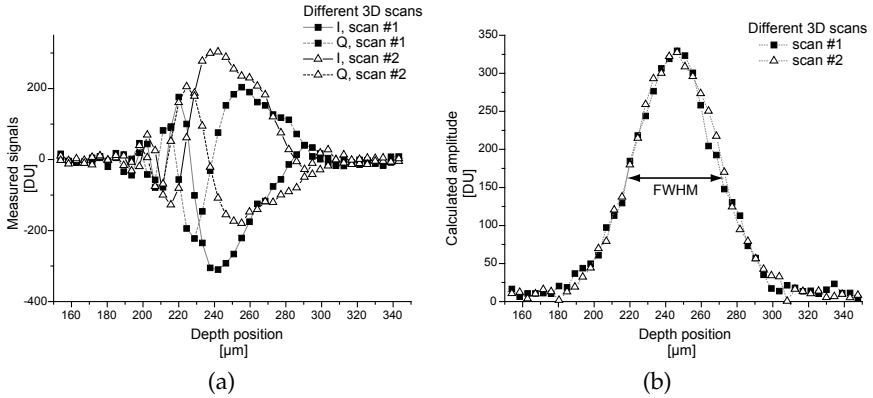


Figure 7.4: Sensitivity measurement with the fs laser illumination source: (a) Pixel output signals in-phase A_I and quadrature A_Q and (b) the calculated envelope amplitude are shown. With a sample of reflectance $R_s = 10^{-5.8}$, a performance of $SNR \gtrsim 32$ dB was measured, corresponding to a sensitivity of ~ 90 dB. The FWHM envelope width is about $54 \mu\text{m}$, which corresponds to a fs laser pulse width of several hundreds of femtoseconds.

case of $N = 10$. For increasing illumination powers, the shot noise increases while the range stays the same, therefore the DR is slightly reduced.

Maximum pixel sensitivity with a fs laser

A fs laser Mira 900-F was used to determine the maximum sensitivity of the developed pixel architecture. The laser was tuned to a center wavelength of $\lambda_0 \simeq 800$ nm at which the quantum efficiency of the photodiode is around $\eta \simeq 0.4$. With the scan speed $v = 20$ mm/s and $N = 10$ averaging periods, the integration time per depth sampling was $T = 200 \mu\text{s}$ with a spacing of $\Delta z = 4.4 \mu\text{s}$. The optical power per photodiode was estimated to be $P_{\text{pd}} \simeq 4.6 \mu\text{W}$ without an additional filter in the reference path. To avoid sensor saturation by a large constant photocurrent offset in spite of the pixel-level offset compensation circuit, as well as to reduce the relative intensity noise (RIN), the optical power was attenuated by adding a filter of $T_f = 10^{-0.5}$ in the reference arm (see Fig. 7.1). This reduces the average power per photodiode to 460 nW, which corresponds to a photocurrent of about 120 nA. Using Eq. 7.2, which includes the offset compensation and the remaining RIN, this leads to a sensitivity of $S_{\text{theory}} = 90.2$ dB.

With a mirror and a filter with a transmittance of $T_f = 10^{-2.9}$ measured at the fs laser

spectrum, a sample with a reflectivity $R_s = 10^{-5.8}$ was simulated. Without the in-pixel offset compensation circuit, the photodiode saturates during every demodulation quarter period and the output signals A_I and A_Q are always zero.

Fig. 7.4 shows the measured signals of one pixel of two subsequent 3D scans and the calculated envelope amplitude. Again, as in the measurements above, the mismatch between the Doppler and the demodulation frequency leads to phase variations during one envelope detection. The measured envelope width (FWHM) is very large, about $\sigma_z \simeq 54 \mu\text{m}$. This corresponds to an illumination spectrum width of only 5 nm if a Gaussian shape is assumed or a pulse length of several hundreds of femtoseconds. A pulse compressor should be added to the femtosecond laser to ameliorate its performance.

Because of the very large envelope width, the depth sampling spacing could have been increased, extending the integration time and therefore increasing the theoretical sensitivity. But as described in Chap. 5, the pixel is optimized for a number of averaged periods $N = 8$ to 12. Therefore N was kept at the above mentioned value, and because the depth sampling spacing was much smaller than the envelope width, the SNR was not only measured as described by Eq. 7.6, but also by comparing the peak values of a pixel over a series of 3D scans. The first method results in a performance of $SNR \simeq 32$ dB, while the second one even yields 32.5 dB. With the measured sample reflectance, this corresponds to a sensitivity of $S_{\text{meas}} \simeq 90$ dB and hence is in good agreement with the theory.

This measurement shows that the in-pixel offset compensation circuit works well. It does not introduce more noise than the expected additional shot noise, which is due to the electrons' Poisson distribution and which cannot be avoided.

7.2 Phase measurements

The pOCT smart sensor has the ability of measuring not only the envelope amplitude but also the phase difference between the carrier of the optical signal and the demodulation signals. The relation is shown in Fig. 7.5. This section describes the expected phase accuracy and compares it with the experimental results.

7.2.1 Experimental set-up

The experimental set-up corresponds exactly to the one used in Sec. 7.1.3, e.g. the pOCT demonstrator in its standard configuration. The illumination source was the

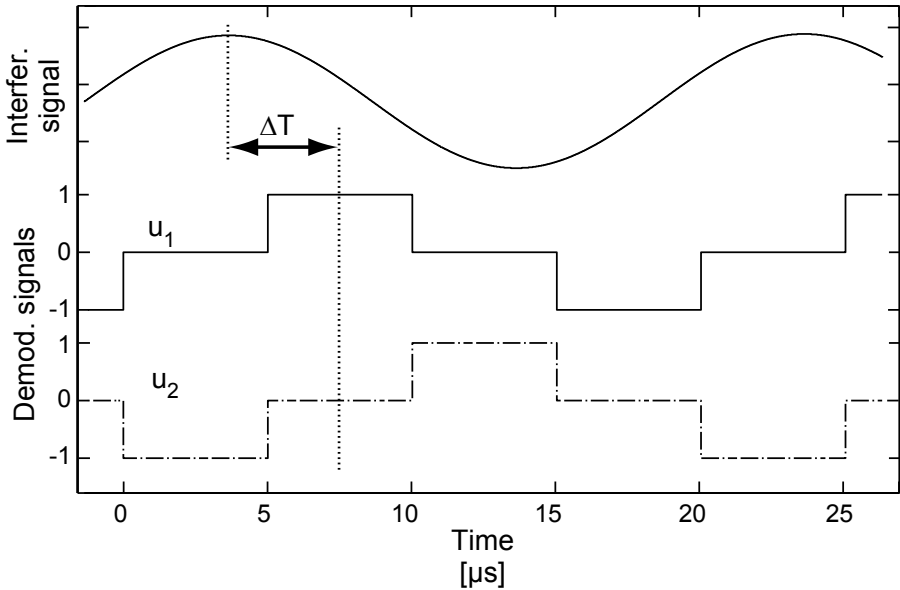


Figure 7.5: Phase detection: At the pixel level, the interferogram signal is multiplied by the signals u_1 and u_2 in order to generate the in-phase A_I and quadrature A_Q signals. The phase of these two generated signals is proportional to the time delay between the interferometric signal and u_1 : $\phi = 2\pi f_D \cdot \Delta T$.

above described SLD featuring an optical power on the photodiodes of $P_{pd} \simeq 22 \text{ nW}$. The number of averaged periods was $N = 10$ corresponding to a depth sampling spacing of $\Delta z = 4.51 \text{ } \mu\text{m}$ and an integration time per sample $T = 205 \text{ } \mu\text{s}$ at the scan speed $v = 20 \text{ mm/s}$.

Measurements were taken with three different neutral density filters in the sample arm and also without filter. Only the results without pixel-level offset compensation are shown, actually, the results with OC are practically identical.

7.2.2 Signal processing and expected performance

For every 3D frame, the phase of the detected interference is different. This is due to the limited accuracy of the scanner position. The phase of the interference at one pixel even varies slightly from one 2D frame to the next due to the frequency mismatch as seen above. Therefore it is not possible to measure the sensor's phase detection

Sample reflectance $R_s = T_f^2$	Measured amplitude SNR	Theoretical phase error $\sigma_{\phi,\text{theory}}$	Measured phase error $\sigma_{\phi,\text{meas}}$
1	saturated signals, ≥ 53 dB		45° steps
$10^{-2.11}$	46.1 dB	0.3°	2.0°
$10^{-3.50}$	33.7 dB	1.2°	1.9°
$10^{-4.14}$	27.1 dB	2.5°	2.7°

Table 7.2: Phase measurement of the pOCT system, with three different neutral density filters in the sample arm and without filter. The optical power per photodiode was 22 nW leading to a theoretical sensitivity of 69.6 dB. The measured sensitivity is 0.9 – 2.4 dB smaller than predicted by the theory and independent of the sample reflectance in its linear range.

performance absolutely. But the phase difference between two pixels is independent of the absolute phase and constant over different 3D frames. In this case both pixels contribute noise to the phase difference. Assuming this noise is only due to photonic shot noise or independent temporal noise of each pixel, the phase noise of one pixel is $\sqrt{2}$ times smaller than the measured phase difference noise. The measurements shown below take this factor already into account.

It can be shown that the theoretical phase noise corresponds to

$$\sigma_{\phi,\text{theory}} = \frac{1}{\sqrt{\text{SNR}_A}} \quad (7.7)$$

(see A.5). The phase error was measured by comparing the phase difference of two pixels at a certain depth position over a series of 3D frames. The amplitude SNR was also measured, and it was used to determine the theoretical phase error. The two errors are then compared.

7.2.3 Results and discussion

Tab. 7.2 shows the results of the phase measurements. The measured amplitude SNR is 0.9 – 2.4 dB smaller than the shot noise limit, as demonstrated above. For the measurements with the least reflective sample, the measured result corresponds well to the theory. The theoretic phase error decreases for more reflective samples, where larger signal amplitudes and better SNR are measured. But the measured phase error decreases only down to about 2°. It can be expected that this noise is due to the output

signal path non-linearity, and therefore could theoretically be improved by calibration.

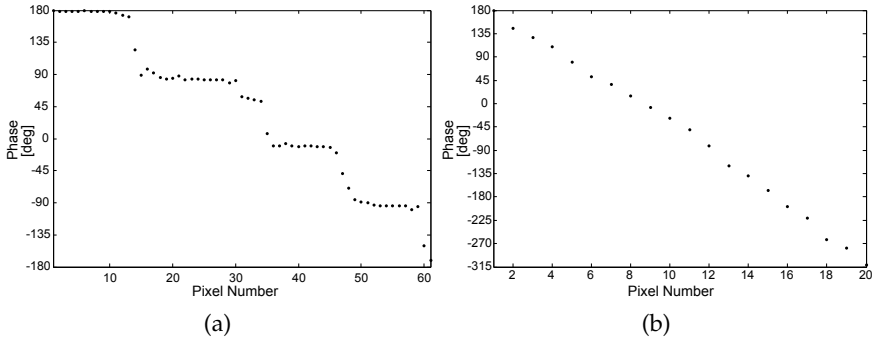


Figure 7.6: Measured phase over some neighboring pixels of one 2D frame: (a) shows the measurement without any filter in the sample path. Only phase steps of 90° are possible due to the saturation of the pixel output signals, while in the measurement with the sample reflectivity $R = 10^{-4.14}$ shown in (b), the signals do not saturate and any phase can be measured. The mirror has not exactly the same inclination for the two measurements, which explains the slope difference.

In Sec. 7.1.3 it was shown that if the sample reflectance is too high, the pixel output signals saturate due to their limited swing. This reduces not only the measured SNR and broadens the depth resolution but also destroys the phase measurement capabilities. Fig. 7.6 shows the case of the measurement of the sample with reflectivity $R = 1$, where only 90° steps are detectable.

The phase detection capability of the pOCT smart pixel sensor was proven by this experiment to work as expected. The achieved accuracy of 2° corresponds to a depth distance of around 2.3 nm for surface detection. Obviously attention must be paid to adjust the contrast and illumination level to obtain optimum results.

7.3 Demodulation frequency mismatch and vibrations

This section describes the experimental verification of the reduction of the measured amplitude by the mismatch of the modulation and the demodulation frequency and by vibrations of the interferometer path-length described in Sec. 4.4.

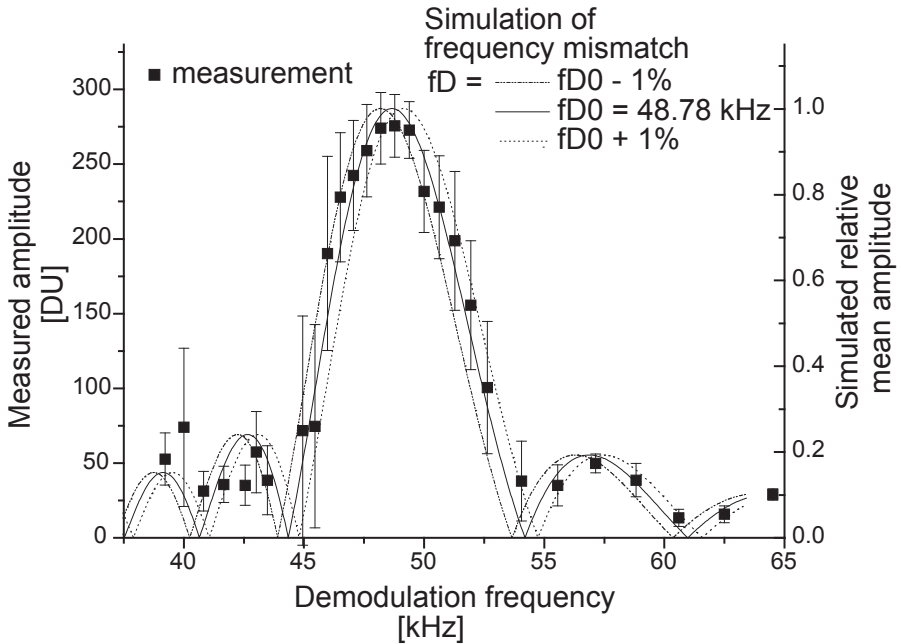


Figure 7.7: Measurement of the detected amplitude as a function of the mismatch between the modulation and the demodulation frequency. The mean value of the measured maximum amplitude follows the simulated curve. The dependance of the standard deviation of the measurements on the frequency mismatch can be explained by assuming a standard deviation of $\sim 1\%$ of the Doppler frequency.

7.3.1 Mismatch of modulation and demodulation frequency

The carrier frequency of the detected photocurrent depends on the carrier of the complex coherence function of the illumination source, which can be expressed as their center wavelength, and the speed of the path-length change, e.g. the reference mirror speed. In the described pOCT system, this carrier is not recovered in order to generate the demodulation frequency. Instead, the correct demodulation frequency is calculated and generated independently. This makes the system susceptible to temporal drifts of the scanner control and of the spectrum of the illumination source. Furthermore, the scan speed accuracy is limited and features a non-linear behavior, especially for large depth ranges.

Experimental set-up

The original set-up was used with a mirror and a neutral density filter of $T_f = 10^{-2.11}$ in the sample arm, as described in Sec. 7.1.3. The SLD has a peak wavelength of $\lambda_0 \simeq 820$ nm and the scanner is moved with a constant speed $v \simeq 20$ mm/s, resulting in a Doppler frequency of $f_D \simeq 48.78$ kHz. The number of periods, over which the in-phase and quadrature signals are averaged, was $N = 10$. A series of 3D frames was acquired for a given demodulation frequency. For one pixel the maximum amplitude was detected in every 3D frame. Of this maximum amplitude the mean value and the standard deviation was calculated over the series of 3D frames.

Results and discussion

The experimental results for frequency mismatch are shown in Fig. 7.7. The measured mean value of the maximum amplitude follows the simulated curve. A frequency mismatch of $\pm 6\%$ reduces the measured mean amplitude already by more than a factor 2.

The standard deviation shows a strong dependence on the demodulation frequency. The standard deviation of the simulation due to different phase delays between modulated and demodulation signal is much smaller and does not explain this behavior. As already discussed in Sec. 7.1.3, the limited scanner position precision for a sample at a certain depth in the acquired 3D frame leads to an amplitude variation between different measurements. This explains the relation between demodulation frequency and amplitude standard deviation neither. The amplitude deviation seems to be related to the slope of the amplitude vs. demodulation frequency curve. This behavior can be explained by assuming a scan speed respectively a Doppler frequency standard deviation of $\sim 1\%$.

A reduction of this type of signal distortion can be achieved by reducing the number of periods over which the signals are averaged N . Another possibility to reduce this effect is a closed loop system that modifies the demodulation frequency during a scan in agreement with the measured scan speed. Such a feedback will reduce the precision requirements for the scanner, since it also allows a sinusoidal movement near resonance. Further robustness against distortion due to frequency mismatch can be achieved with a smart pixel architecture, in which the envelope instead of the in-phase and quadrature signals is averaged.

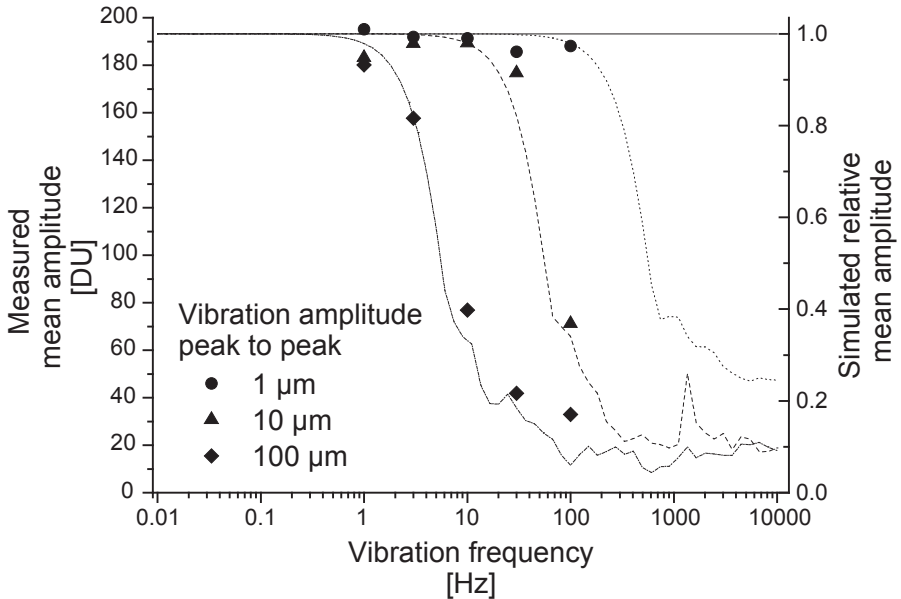


Figure 7.8: Measurement of the detected amplitude as a function of the sample vibration amplitude and frequency.

7.3.2 Sample vibration effects

A targeted application of this pOCT system is industrial quality control. Unlike in a lab, in these environments usually significant vibrations occur. The measurements presented in this section show the experimental verification of the system performance degradation due to vibrations of the sample.

Experimental set-up

The original set-up was used. The sample was a neutral density filter of $T_f = 10^{-2.11}$ and a mirror on a voice coil. The voice coil was driven by a wave generator and produced a sinusoidal movement of the sample in the axial direction. The displacement of the sample had been calibrated with the pOCT system. The illumination and the system parameters were the same as in the frequency mismatch experiment described above. Unfortunately the cut-off frequency of the sample was around some hundreds of Hz. This allows to observe the signal degradation for vibrations with amplitudes of

several μm .

Results and discussion

The measured amplitude reduction as function of the vibration amplitude and frequency is compared to the simulation in Fig. 7.8. The general behavior as predicted in Sec. 4.4 can be observed for the measurements with vibrations with peak to peak amplitudes of $10\ \mu\text{m}$ and $100\ \mu\text{m}$.

The vibratory conditions of an industrial production environment vary in a large range. In some cases a special effort will be necessary to reduce the amplitude of the vibrations between the two interferometer arms by damping mechanisms in order to achieve the limit of the vibration frequency amplitude product stated in Sec. 4.4. Above this limit, three-dimensional images cannot be acquired reliably. By increasing the scan speed, the degrading effect of vibrations is reduced but an illumination source with more optical power is required.

7.4 Grey-level imaging performance

The pOCT smart pixel imager not only allows OCT signal demodulation at the pixel level but also conventional intensity images can be acquired. This mode simplifies system alignment and probe handling significantly. The following sections describe the grey-level imaging performance.

The experimental parameter determination follows in set-up and calculations the methods proposed by Willemin *et al.* [3]. An Ulbrichts sphere was used to generate a homogeneous illumination of the sensor. The peak wavelength was $\lambda_0 = 730\ \text{nm}$ yielding a quantum efficiency around $\eta \simeq 0.6$ for the photodiodes.

The timing diagram as well as the reference voltages presented in Sec. 5.3.7 are applied. Two parameters affecting the intensity imaging timing can be set in the camera registers: the number of integration cycles per readout N and the integration time T for each cycle. The total integration time therefore is $T_{\text{tot}} = N \times T$.

7.4.1 Optimum number of integration cycles N

The sensor output voltage was measured as a function of the irradiance while varying the number of integration cycles per readout N . All measurements were taken with

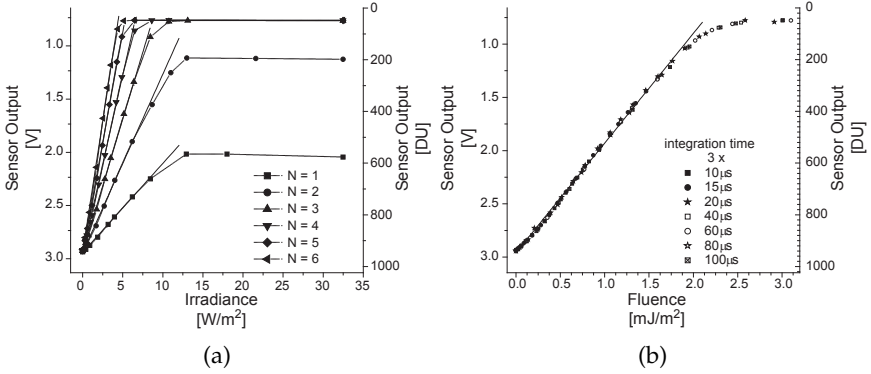


Figure 7.9: Intensity mode measurements: (a) Sensor output versus irradiance as a function of the number of integration cycles per readout N : The gain is proportional to N but the maximum swing is only reached for $N \geq 3$. (b) Sensor output versus fluence for $N = 3$ and different integration times: a sensitivity of 1.03 kV/l/m^2 corresponding to 650 nV/phonon at $\lambda = 730 \text{ nm}$ was measured.

the integration time $T_{\text{tot}} = N \times 80 \mu\text{s}$. The maximum irradiance was around $I_{\text{max}} \approx 30 \text{ W/m}^2$. The results (Fig. 7.9(a)) show that the output signal is proportional to T_{tot} and therefore proportional to the number of cycles N .

The maximum swing of 2.1 V is only achieved for $N \geq 3$. This is due to the fact that in the smart pixel architecture, the swing of the photodiode times the subtraction to integration capacitor ratio is around 60% smaller than the signal output swing. Therefore usually $N = 3$ is chosen.

7.4.2 Sensor characterization in grey-level mode

The linearity measurements exhibit a sensitivity of 1.03 kV/l/m^2 corresponding to 650 nV/phonon at $\lambda = 730 \text{ nm}$, independent of the integration time. Fig. 7.9(b) shows a certain non-linearity: for small fluences, the sensitivity is smaller than for moderate fluences. The deviation from a linear response is less than 2% on a linear range of around 1.8 V .

The temporal noise was measured by comparing two consecutively acquired frames with an integration time of $T_{\text{tot}} = 3 \times 80 \mu\text{s}$ in the dark. It is $\sigma_V = 2.67 \text{ mV}$, leading to a linear dynamic range of $DR \geq 56 \text{ dB}$. This corresponds well to the dynamic range of 57.1 dB predicted by the theory. The fixed pattern noise (*FPN*), denoting the constant

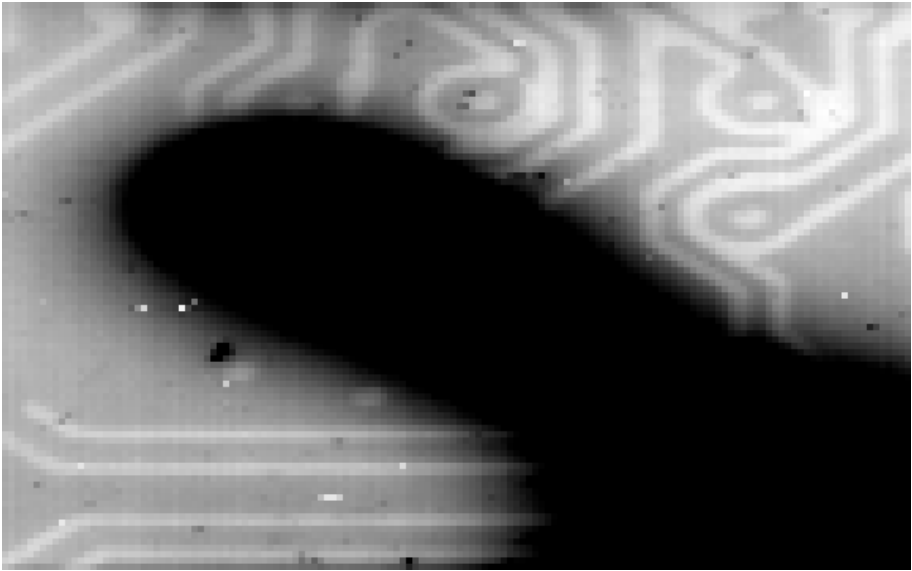


Figure 7.10: Intensity image of a part of a bead of dispensed glue for a die bonding application: The number of integration cycles was $N = 3$ and the total integration time was 9 ms. The pOCT system optics was set to a field of view of $2.9 \text{ mm} \times 3.1 \text{ mm}$ and an external illumination source was used. Not only the glue is visible but also some electrical tracks on the substrate.

offset between the pixels without illumination, is $FPN = 15.8 \text{ mV}$.

For the targeted applications, such as e.g. system alignment and sample handling, the intensity-imaging performance of the sensor is absolutely satisfactory. In the pOCT system, care must be taken that the reference arm is blocked during the intensity-image acquisition to avoid signal saturation. Even better results are achieved if an external illumination source is used instead of the integrated SLD, because some reflections from the beam splitter are avoided and the sample is optimally illuminated. Fig. 7.10 shows the intensity image of a part of a bead of dispersed glue for a die bonding application. On the substrate, electric tracks are visible. Some dead pixels are noticeable. The contrast is sufficient, and details that are in focus are well visible.

7.5 Conclusion

The developed smart pixel architecture exhibits near shot-noise limited performance. With an additional neutral density filter in the reference arm, a sensitivity of 90 dB is achieved, exceeding the initially targeted specification. The sensitivity of the total system, which is to our knowledge the fastest TD-OCT system, is limited by the SLD illumination source power of 30 mW to about 67 dB. It has been proved by the use of the fs laser that a better light source will significantly increase the sensitivity performance. By doubling the illumination source power, the sensitivity is increased by 3 dB. Assuming the same optics, i.e. with the same optical power loss in the system, a source with an optical output of 1 W will allow three-dimensional imaging at the same scan speed with a sensitivity of about 79 dB. It is expected that microlenses increasing the pixel fillfactor will increase the sensitivity by 3 – 9 dB.

Scanning OCT systems usually feature a dynamic range of 40 – 60 dB. In human retina imaging for example, the largest reflected signal is about 50 dB smaller than the incident optical power. The best OCT systems achieve a sensitivity of the order of 110 dB, signifying a maximum dynamic range of 60 dB. The measured OCT dynamic range of the presented system of ≥ 50 dB is therefore in the same order as competing systems. Reflectances causing larger interference signals are not lost but just broaden the detected peak degrading the depth resolution. In the case of topography imaging, this broadening can be reduced to an insignificant level by an additional calculation effort.

The developed sensor does not only allow to detect the amplitude of an OCT signal, but allows also the detection of the phase with a measured resolution of 2° . For topographic imaging, the depth difference of two neighboring pixels, if it is smaller than one interferogram period of 410 nm, can be detected with a precision of 2.3 nm. Better results might be achieved through a better scanner motion control.

An important feature of the presented pixel architecture is its ability to acquire intensity grey-level images, simplifying system alignment and probe handling significantly. The measured dynamic range of 56 dB is absolutely satisfactory for the targeted applications.

In an industrial environment, vibrations might occur, which degrade the performance of pOCT imaging just like for any other interferometric device. The calculated signal degradation from Chap. 4 was experimentally verified. In some cases, an additional effort is required to reduce the vibration below the acceptable limit by damping mechanisms. Signal degradation due to scan speed variation was also experimentally verified. The speed accuracy of the chosen scanner and the developed control electronics is sufficient to prevent this effect.

Bibliography

- [1] S. Beer, S. Waldis, and P. Seitz, "Video-rate optical coherence tomography imaging with smart pixels," in *Optical Coherence Tomography and Coherence Techniques* (W. Drexler, ed.), vol. 5140 of *Proc. SPIE*, pp. 69–76, June 2003.
- [2] M. Laubscher, M. Ducros, B. Karamata, T. Lasser, and R. Salathe, "Video-rate three-dimensional optical coherence tomography," *Opt. Express*, vol. 10, pp. 429–435, May 2002.
- [3] M. Willemin, N. Blanc, G. K. Lang, S. Lauxtermann, P. Schwider, P. Seitz, and M. Wány, "Optical characterization methods for solid-state image sensors," *Optics and Laser in Engineering*, vol. 36, pp. 185–194, 2001.

Chapter 8

Applications

The presented pOCT system allows the acquisition of the amplitude and the location in the three-dimensional space of reflections of a sample in real-time. Topography images and tomography images of transparent low-scattering samples can be acquired. The image volumes in the order of some to some ten mm^3 are acquired several times per second. Compared with other topography imaging systems, the pOCT system is either faster (compared to white light interferometry, conventional TD-OCT), allows imaging of noncontinuous surfaces (fringe counting interferometry, some holography systems), or features higher resolution and is not limited by shading (triangulation, fringe projection).

Tomographic imaging applications are also possible with the presented system. An appropriate illumination source with a power of several hundreds of mW is required, potentially increasing the cost of the system.

Among the targeted applications is industrial quality control, where often high-speed surface detection is required. The next section describes a pOCT surface and volume detection application in the field quality control of dispensed glue in a die attach process.

8.1 High-speed topography imaging for optical volume determining of dispensed glue

The process of attaching an IC on a substrate for packaging is called die attach or die bonding. First a glue is dispensed on the substrate, then the IC is picked from the blue

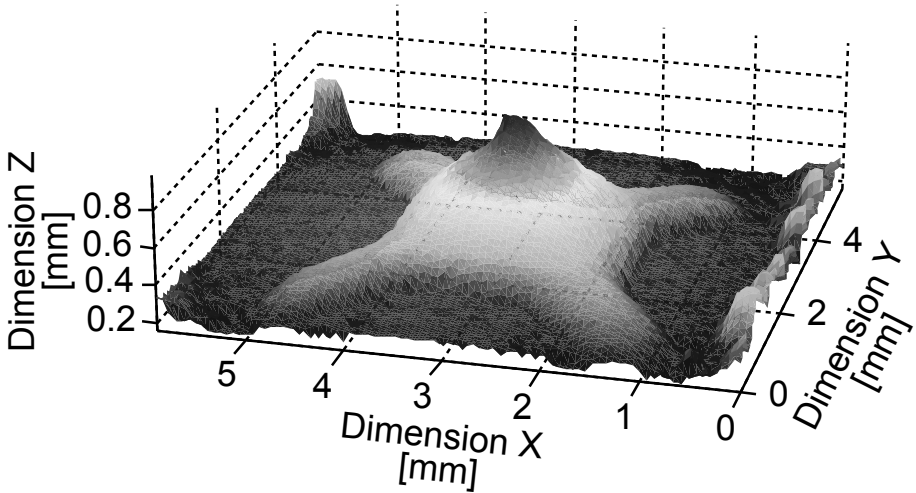


Figure 8.1: Topography of a glue cross dispensed on a substrate for device die bonding: the surface fit of the acquired volumetric pOCT data is shown.

tape that holds the diced wafer. The IC is then placed on the substrate and finally the glue is cured. The reliability is an extremely important property in the IC manufacturer industry. The control of the volume of the dispensed glue allows the prediction if a single device could fall off, and even more importantly, it allows the early detection of a problem with the dispenser that otherwise potentially would damage a whole series of devices. The former control requires testing of every device, while the latter relaxes the requirement to a sample control rate of one to a few per second.

A further area, where pOCT might increase the value of a die bonder, is stacked die packaging: packaging several ICs into one carrier and especially stacking several dies on top of each other is an emerging trend in the IC manufacturer industry. The maintenance of the parallelism of the stacked dies is essential and a challenging task. A pOCT system is capable of detecting the height difference between one side of a die to the other in the order of some micrometers. If an even higher resolution is required, the detected phase can be taken into account.

8.1.1 Measurements

For the proof of principle of dispensed glue volume detection, the presented pOCT system has been slightly modified, e.g. the sample lens L3b has been replaced by a lens

with a focal distance of 50 mm in order to increase the field of view to about 39 mm^2 . Due to the mismatch of the lenses in the sample and in the reference arm, the wavefronts from the sample and the reference arm are differently bent and a curvature of the sample image occurs. This can be corrected either by calibration and data processing, or optical design modifications.

A volume image of 1 mm depth is acquired in 50 ms. The acquired volumetric data is fit by a simple algorithm, which detects the maximum amplitude per pixel over the 3D scan, corresponding to the sample surface. The volumes of several samples of different shapes and sizes has been measured by weighting and then has been compared to the volumes determined by pOCT.

8.1.2 Results and discussion

An example of a surface fit of a bead of dispensed glue in a cross shape is shown in Fig. 8.1. The complete bead is well detected. At the corners and one edge of the field of view, noise is noticeable. This is due to the Gaussian profile of the illumination beam: In the corners, the optical power is smaller, leading to a less distinctive optical interference signal and a reduced *SNR* of the generated envelope amplitude. Therefore the fitting algorithm fails and produces additional bumps.

Fig. 8.2 shows a cross-section through the presented sample. It corresponds to the amplitude data of the sensor row number 42 acquired during the depth scan. Obviously the matt surface with a slope of up to more than 60° is detected. A lacquer of an optical thickness of about $50 \mu\text{m}$ covering the substrate is well visible.

For large probes that spread over the complete field of view and had volumes in the order of $2 - 2.5 \text{ mm}^3$, the pOCT measured volumes were an average 3.1 % larger than the control measurements with the weighting machine. Their standard deviation corresponds to about 2.5 % of the volume. The average error is probably due to the limited accuracy of the field of view estimation and thus can be corrected by system calibration. The standard deviation might have different reasons: the limited lateral resolution of 144×90 pixel, the limited depth resolution due to the illumination source spectrum and the scan speed and position variations, and insufficient sample illumination power especially at the field of view borders, leading to a reduced *SNR* and fitting algorithm failure.

Optical glue volume measurement with an accuracy of $\sim 2.5 \%$ in only 50 ms for any bead shape was demonstrated. Some additional effort to improve the optical system and its calibration, the illumination power, and the fitting algorithm, will further increase the accuracy. It can be assumed that the integration of such a system into e.g. a

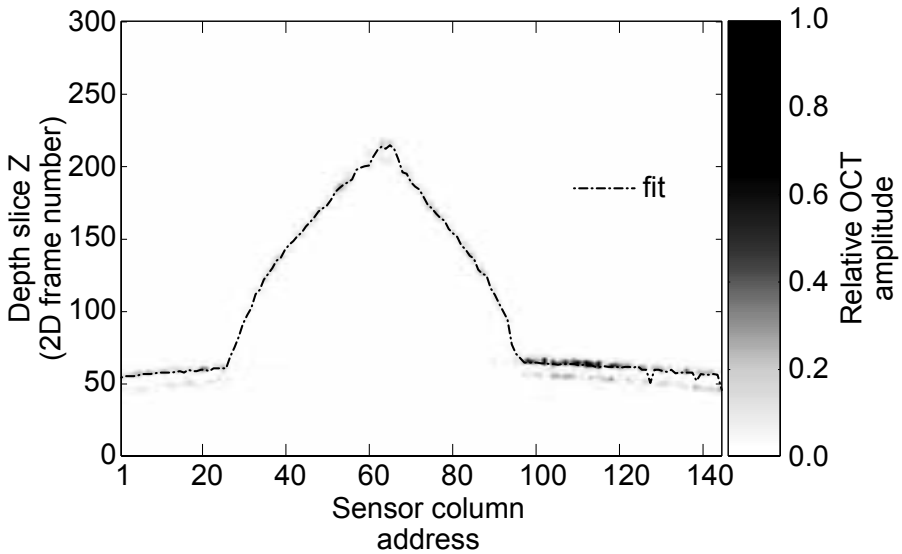


Figure 8.2: Cross-section through the sample shown in Fig. 8.1 at the row #42 corresponding to $Y = 2.87$ mm. The acquired OCT amplitude signal is shown as well as the surface fit. The curvature of the substrate is due to the different lenses in the reference and the sample path. The substrate is covered by a lacquer of an optical thickness of about $50\ \mu\text{m}$.

die attach machine, will lead to an additional advantage for marketing this machine.

8.2 Conclusion

Volume determination of beads of dispensed glue for quality control in a die bonding process has been demonstrated as an example of an industrial application. A volume detection precision of 2.5 % was achieved within 50 ms per sample. This is satisfactory for the detection of dispenser malfunction and the prediction of the sample fixity.

Other industries have also needs in the determination of surfaces and volumes just as in the chosen example. POCT offers a cost efficient solution to these tasks. Surfaces in the range of hundreds of micrometers to tens of millimeters are detected in real-time. In the case of dynamically focusing, the depth range of the sample may extend to some millimeters. Also very steep slopes are detected. Not only surfaces but also structures in transparent or low-scattering materials can be imaged [1] as well as the thickness

of a semi-transparent film such as a lacquer, extending the range of applications for which the pOCT system offers a suitable solution.

Bibliography

- [1] S. Beer, P. Zeller, N. Blanc, F. Lustenberger, and P. Seitz, "Smart pixels for real-time optical coherence tomography," in *Three-Dimensional Image Capture and Applications VI* (B. D. Corner, P. Li, and R. P. Pargas, eds.), vol. 5302 of *Proc. SPIE*, pp. 21–32, Apr. 2004.

Chapter 9

Conclusion

For the past 250 years, optical microscopy has been one of the major tools for the advancement of many fields of science and technology. This achievement has been possible despite the obvious restriction of optical microscopy images to two dimensions. To overcome this limitation, several techniques have been proposed in the past, most notably holography, confocal microscopy, and various forms of imaging interferometry. With the first practical implementations of optical coherence tomography (OCT) techniques, it has suddenly become possible to image any type of object in full three dimensions, even if it is highly scattering and only partially translucent. Still, the technical implementations of OCT suffer from one serious drawback compared to conventional optical microscopy, the lack of real-time operation (frame rates of 10 Hz or more).

The goal of this work was the development of a real-time volumetric OCT imaging system. An approach with massively parallel signal processing has been exploited in order to achieve this objective. The developed key component is a smart imager with pixel-level signal demodulation. The design of the developed high-speed parallel (p-) OCT system is optimized in order to work close to the physical limit. With this demonstrator, we have proved that pOCT provides solutions for real-time three-dimensional imaging. With a lateral resolution of 144×90 pixels and an axial scan speed of typically 20 mm/s , we have achieved the, to our knowledge, fastest time-domain (TD-) OCT volumetric frame acquisition. This was only possible by developing a smart pixel architecture, which is the basic structure of the CMOS custom designed pOCT imager (patent granted). The versatile pixel architecture allows not only the detection of the envelope of a typical modulated OCT signal but also its phase, and in a different mode the acquisition of grey-level images.

The developed sensor features stable operation under different conditions. The scan speed can be varied in a large range, e.g. Doppler frequencies up to 50 kHz with full sensor resolution and even above 100 kHz with windowing to reduce the data flow can be handled; and there are no constraints for the lower limit. The interferometric signal is averaged over a selectable number of periods N , optimally between 8 and 12. By the use of windowing, N can be further reduced. Therefore high-resolution OCT is possible with an appropriate illumination source. Flexibility as well as also performance, robustness, and handling have been significantly improved compared to the former generation pOCT sensor [1]. Very few parameters have to be set and no calibration is required.

The chosen CMOS process features a quantum efficiency above $\eta = 0.3$ for wavelengths between 420 nm and 850 nm. This limits the range of eligible light sources as well as the targeted samples, e.g. dermatology applications, which usually apply illumination spectra around 1300 nm, require further developments, such as a hybrid technology approach.

The pixel achieves a sensitivity of more than 90 dB and a dynamic range of about 50 dB. This is more than sufficient for topographic imaging and enough for tomographic imaging of many technical samples e.g. transparent liquids or lacquer. On the other hand, a sensitivity of more than 100 dB is required for biomedical applications in e.g. ophthalmology or dermatology [2]. The modification of the pixel architecture to increase the sensitivity is straight forward, but there are non-negligible technical barriers for the development of the opto-mechanical system, especially the illumination source. As discussed in Chap. 2, the sensitivity is proportional to the optical energy available per voxel. High-speed TD-OCT systems usually suffer, in comparison, from low sensitivities because of the small integration time. In Chap. 3, the use of spatially incoherent light sources such as thermal lamps to suppress the optical cross-talk between the pixels was discussed. These sources feature even less optical power per pixel. The crucial steps to improve pOCT systems for tomographic imaging are, therefore, apart from advancements in pixel performance and sensor size, the development of powerful light sources.

Frequency-domain (FD-) OCT with a spectrometer to analyze the detected signal or with a wavelength tunable illumination source represents a strong competitor for TD-OCT [3, 4]. Its sensitivity advantage becomes very important especially under low-illumination conditions or in high-speed applications. Since only lateral and no axial scanning is required, it features the same system simplicity advantage over scanning TD-OCT as pOCT. The most recent publications show that its maximum volume acquisition rate will soon approach the performance of our system [5, 6]. In spite of FD-OCT's sensitivity advantage, TD-pOCT represents the better solution for several

applications: Dynamically focussing is only possible with TD-OCT, therefore it is the preferred technique for samples with a depth range of several millimeters.

Recent OCT systems feature a depth resolution, which is limited by the illumination source spectrum, in the sub-micrometer range [7–10]. Diffraction in the optical system e.g. the numerical aperture limits the lateral resolution defined as the minimum distance between two points, for which they are still distinguishable. In a system without dynamic focus control, this lateral resolution and the depth range are linked by the numerical aperture. The number of A-scans, or in the case of pOCT the number of sensor pixels, is also referred to as lateral resolution of an OCT image. Usually the lateral distance between A-scans is set to be in the order of the minimum distance, relating the two definitions of the resolution by the width of the sample image. In pOCT this relation holds also for an optical system optimized for resolution. But the number of pixels is not unlimited as is the number of A-scans. A pOCT smart pixel has a certain area consumption: in the presented version $50\ \mu\text{m} \times 86.3\ \mu\text{m}$; for future versions this size might decrease by a one-digit factor. The maximum pixel field area, which determines the number of pixels, is limited by optical and CMOS process constraints. The larger the pixel field is, the larger become the optical components such as beam splitter and lenses, the larger and more expensive becomes the total system. In the same way the sensor production costs increase superproportionally. A reticle size sensor (usually around $400\ \text{mm}^2$) would allow a sensor with a resolution close to quarter VGA (320×240). A smart-pixel sensor with one million pixels is only imaginable by the use of a completely different principle or in combination with a hybrid or TFA sensor technology.

The larger the resolution in number of pixels, the larger becomes also the amount of data to be handled. For surface detection, where the pOCT image mainly contains zeros, the required data can be reduced to a small fraction of the originally acquired data. This can be done on the software level to reduce the storage capacity requirements, but it is even better to introduce data compression at an earlier level. Imaginable is the implementation of a surface detection algorithm on the camera logic, thus reducing the data rate between camera and PC. Even more advantageous but also much more demanding is it to place the signal processing at the sensor level. For tomographic imaging, data compression will be much less efficient, and the maximum data rate of the connection between the camera and the PC will play a major role. The advancements in computer technology may solve this bottleneck with successor products of e.g. Gigabit Ethernet and CameraLinkTM.

Increasing the number of pixels of a pOCT smart sensor requires also an increase of the total illumination power, if the sensitivity and the scan speed are to be maintained. As stated above, the illumination source poses a problem already for smaller arrays.

An increase of the fillfactor by using either microlenses or a hybrid technology such as thin film on ASIC (TFA) will allow increasing the lateral resolution by a small one-digit factor while maintaining the illumination source, the speed, and the sensitivity. The stated problems due to an increase of the pixel resolution can be solved by sacrificing one dimension e.g. by the development of a smart pixel line sensor, as already developed in the former pOCT smart pixel architecture [11]. For tomographic applications with a human observer and without automatic three-dimensional feature extraction, this might become a pragmatic and practically useful solution.

This work has also demonstrated the wide possibilities of CMOS smart pixels. Massively parallel signal processing at the pixel level permits the acquisition of a large amount of data and filter out just the required information. This same pixel architecture can be useful for a variety of applications other than pOCT just as the former generation sensor was [12–15]. There are also other problems that cannot be solved by the presented pixel architecture, but will be solved by other smart pixels profiting from the parallel signal processing advantage; and even pOCT's most promising competitor FD-OCT will profit from solutions and improvements made possible by smart pixel technologies, overcoming the limitations in dynamic range, resolution, and read-out speed of conventional CCD sensors.

In the rapidly evolving field of OCT with many different trends, the present work represents a significant step towards high-speed imaging. We believe that smart imagers will play an increasingly important role in OCT imaging.

Bibliography

- [1] S. Bourquin, P. Seitz, and R. P. Salathé, "Optical coherence topography based on a two-dimensional smart detector array," *Opt. Lett.*, vol. 26, pp. 512–514, Apr. 2001.
- [2] D. Huang, E. A. Swanson, C. P. Lin, J. S. Schuman, W. G. Stinson, W. Chang, M. R. Hee, T. Flotte, K. Gregory, C. A. Puliafito, and J. G. Fujimoto, "Optical coherence tomography," *Science*, vol. 254, pp. 1178–1181, 1991.
- [3] R. A. Leitgeb, C. K. Hitzenberger, and A. F. Fercher, "Performance of fourier domain vs. time domain optical coherence tomography," *Opt. Express*, vol. 11, pp. 889–894, Mar. 2003.
- [4] M. A. Choma, M. V. Sarunic, C. Yang, and J. A. Izatt, "Sensitivity advantage of swept source and Fourier domain optical coherence tomography," *Opt. Express*, vol. 11, pp. 2183–2189, May 2003.
- [5] N. Nassif, B. Cense, B. Hyle Park, S. H. Yun, T. C. Chen, B. E. Bouma, G. J. Tearney, and J. F. de Boer, "In vivo human retinal imaging by ultrahigh-speed spectral domain optical coherence tomography," *Opt. Lett.*, vol. 29, pp. 480–482, Mar. 2004.

- [6] R. Huber, K. Taira, M. Wojtkowski, T. H. Ko, J. G. Fujimoto, and K. Hsu, "High-speed frequency swept light source for Fourier domain OCT at 20 kHz A-scan rate," in *Coherence Domain Optical Methods and Optical Coherence Tomography in Biomedicine IX* (D. Kessel, ed.), vol. 5690 of *Proc. SPIE*, Apr. 2005.
- [7] W. Drexler, U. Morgener, F. X. Kärtner, C. Pitris, S. A. Boppart, X. D. Li, E. P. Ippen, and J. G. Fujimoto, "In-vivo ultrahigh-resolution optical coherence tomography," *Opt. Lett.*, vol. 24, pp. 1221–1223, 1999.
- [8] A. F. Fercher, C. K. Hitzenberger, M. Sticker, E. Moreno-Barriuso, R. Leitgeb, W. Drexler, and H. Sattmann, "A thermal light source technique for optical coherence tomography," *Opt. Commun.*, vol. 185, pp. 57–64, Nov. 2000.
- [9] L. Vabre, A. Dubois, and A. C. Boccara, "Thermal-light full-field optical coherence tomography," *Opt. Lett.*, vol. 27, pp. 530–532, Apr. 2002.
- [10] B. Povazay, K. Bizheva, A. Unterhuber, B. Hermann, H. Sattmann, A. F. Fercher, W. Drexler, A. Apolonski, W. J. Wadsworth, J. C. Knight, P. S. J. Russell, M. Vetterlein, and E. Scherzer, "Submicrometer axial resolution optical coherence tomography," *Opt. Lett.*, vol. 27, pp. 1800–1802, 2002.
- [11] S. Bourquin, V. Monterosso, P. Seitz, and R. P. Salathé, "Video-rate optical low-coherence reflectometry based on a linear smart detector array," *Opt. Lett.*, vol. 25, pp. 102–104, Jan. 2000.
- [12] J. Mitić, T. Anhut, M. Meier, M. Ducros, A. Serov, and T. Lasser, "Optical sectioning in wide-field microscopy obtained by dynamic structured light illumination and detection based on a smart pixel detector array," *Opt. Lett.*, vol. 28, pp. 698–700, May 2003.
- [13] J. Mitić, T. Anhut, A. Serov, T. Lasser, and S. Bourquin, "Real-time optically sectioned wide-field microscopy employing structured light illumination and a CMOS detector," in *Three-Dimensional and Multidimensional Microscopy: Image Acquisition and Processing X* (J.-A. Conchello, C. J. Cogswell, and T. Wilson, eds.), vol. 4964 of *Proc. SPIE*, pp. 41–49, July 2003.
- [14] S. Bourquin, R. P. Prasankumar, F. X. Kärtner, J. G. Fujimoto, T. Lasser, and R. P. Salathé, "High-speed femtosecond pump-probe spectroscopy with a smart pixel detector array," *Opt. Lett.*, vol. 28, pp. 1588–1590, Sept. 2003.
- [15] M. Laubscher, S. Bourquin, L. Froehly, B. Karamata, and T. Lasser, "Spectroscopic optical coherence tomography based on wavelength de-multiplexing and smart pixel array detection," *Opt. Commun.*, vol. 237, pp. 275–283, July 2004.

Appendix A

Appendix: Formulas

A.1 Gaussian illumination spectrum

Gauss spectrum with a spectrum FWHM of $\Delta\nu$:

$$S(\nu) = I_0 \cdot \frac{2\sqrt{\frac{\ln 2}{\pi}}}{\Delta\nu} \cdot e^{-4 \ln 2 \frac{(\nu-\nu_0)^2}{\Delta\nu^2}} \quad (\text{A.1})$$

The total intensity is

$$\begin{aligned} I &= \int_0^{\infty} S(\nu) d\nu = I_0 \cdot \frac{2\sqrt{\frac{\ln 2}{\pi}}}{\Delta\nu} \cdot \underbrace{\int_0^{\infty} e^{-4 \ln 2 \frac{(\nu-\nu_0)^2}{\Delta\nu^2}} d\nu}_{\frac{\sqrt{\pi} \cdot \Delta\nu}{2\sqrt{\ln 2}}} \\ &= I_0 \end{aligned} \quad (\text{A.2})$$

The coherence function is the inverse Fourier transform (Wiener-Khinchin theorem)

$$\begin{aligned} \Gamma(\tau) &= \mathcal{F}^{-1} \{S(\nu)\} = \int_0^{+\infty} S(\nu) e^{j2\pi\nu\tau} d\nu \\ &= I_0 \cdot e^{-\frac{\pi^2 \cdot \Delta\nu^2}{4 \ln 2} \cdot \tau^2} e^{j2\pi\nu_0\tau} \end{aligned} \quad (\text{A.3})$$

by using

$$\mathcal{F}^{-1} \left\{ \sqrt{\frac{\pi}{a}} e^{-\frac{\pi^2 \nu^2}{a}} \right\} = e^{-a\tau^2} \quad (\text{A.4})$$

and the frequency shift theorem

$$\mathcal{F} \{f(\tau)\} = F(\nu) \quad \longrightarrow \quad \mathcal{F} \{f(\tau) \cdot e^{j2\pi\nu_0\tau}\} = F(\nu - \nu_0). \quad (\text{A.5})$$

The FWHM of $\Gamma(\nu)$ is

$$\tau_c = \frac{4 \ln 2}{\pi \Delta\nu}, \quad (\text{A.6})$$

which translates to a coherence length as function of the wavelength

$$l_c = \tau_c \cdot c = \frac{4 \ln 2}{\pi} \cdot \frac{\lambda^2}{\Delta\lambda}. \quad (\text{A.7})$$

A.2 Rectangular illumination spectrum

Rectangular spectrum with a spectrum FWHM of $\Delta\nu$:

$$S(\nu) = \frac{I_0}{\Delta\nu} \cdot \begin{cases} 1 & \text{if } |\nu - \nu_0| \leq \Delta\nu/2 \\ 0 & \text{else.} \end{cases} \quad (\text{A.8})$$

Its inverse Fourier transform is

$$\Gamma(\tau) = \mathcal{F}^{-1} \{S(\nu)\} = I_0 \cdot \Delta\nu \cdot \text{sinc}(\Delta\nu\tau) e^{j2\pi\nu_0\tau} \quad (\text{A.9})$$

with a FWHM of

$$\tau_c \simeq 0.6/\Delta\nu \quad (\text{A.10})$$

and the disadvantage of sidelobes of 13 dB.

A.3 Theoretical SNR and sensitivity with offset compensation and relative intensity noise

The SNR of an OCT system is given by

$$SNR_{\text{OCT}} = \frac{(m_{\text{mod}})^2}{\sigma_{m_{\text{total}}}^2}, \quad (\text{A.11})$$

where m_{mod} is the root mean square number of photogenerated modulation electrons and $\sigma_{m_{\text{total}}}$ is the total noise.

At photodetection, for a photon flux of Poisson or Bose-Einstein distribution, the distribution of photogenerated charges remains of the same type with a mean value reduced by a factor η called quantum efficiency. The partially coherent light used in an OCT system is neither a pure Poisson nor a pure Bose-Einstein distribution. Nevertheless, in this calculation, the preservation of its distribution type during the absorption process is assumed for simplicity reasons.

As seen in Chap. 2, the number of modulated photoelectrons is

$$m_{\text{mod}} \simeq \frac{\eta T}{h\nu} \cdot \sqrt{2P_r P_s}, \quad (\text{A.12})$$

where T is the integration time and $P_{r,s}$ is the optical power coming from the reference and the sample path, respectively, while blocking the other one. The photon noise is

$$\sigma_n^2 = \bar{n} + \frac{1 + \Pi^2}{2N} \cdot \bar{n}^2, \quad (\text{A.13})$$

where the first term is due to the Poisson contribution and the second term represents the so-called excess noise due to the Bose-Einstein photon bunching [1]. Π is the degree of polarization. N is the effective number of detected modes, e.g. $N = 1$ for a pure thermal field, resulting in the Bose-Einstein distribution, $N = \infty$ for a purely coherent field, resulting in the Poisson distribution. Usually N is the ratio of the detection time to the coherence time and the detection area to the coherence area, $N = T/\tau_c \cdot A/A_c$ [2].

The detector noise is assumed to be negligible, except for the offset compensation electron shot noise that is due to the Poisson distribution of the compensation current. The total electron noise becomes

$$\sigma_{m_{\text{total}}}^2 = \underbrace{\bar{m}}_{\text{Photoelectron Poisson}} + \underbrace{\frac{1 + \Pi^2}{2N} \cdot \bar{m}^2}_{\text{Photoelectron Bose-Einstein}} + \underbrace{\bar{m}}_{\text{OC current Poisson}}, \quad (\text{A.14})$$

where $\bar{m} \simeq \eta P_s T / h\nu$. Assuming that the detection area corresponds to the coherence area, $N = T/\tau_c$. If the signal reduction due to the natural sampling applied in the presented system is taken into account, the SNR becomes

$$SNR_{\text{OCT}} \simeq \frac{16}{\pi^2} \frac{\eta P_s T}{h\nu} \cdot \frac{1}{2 + \frac{1+\Pi^2}{2} \cdot \frac{\eta P_s \tau_c}{h\nu}}. \quad (\text{A.15})$$

In many cases, especially in pOCT, $\tau_c \eta P_s / h\nu \ll 2$ and therefore the correction term due to the photon bunching is negligible.

The sensitivity taking into account natural sampling, OC, and excess noise is given as

$$S = \frac{1}{R_{\min}} \simeq \frac{16}{\pi^2} \frac{\eta P_{s0} T}{h\nu} \cdot \frac{1}{2 + \frac{1+\Pi^2}{2} \cdot \frac{\eta P_s \tau_c}{h\nu}}, \quad (\text{A.16})$$

where P_{s0} signifies the optical power on the detector when replacing the sample by a mirror of reflectance $R = 1$ and blocking the reference arm.

A.4 SNR calculation from measurements

The amplitude and its SNR are defined as:

$$A = \sqrt{A_I^2 + A_Q^2} \quad (\text{A.17})$$

$$SNR_A = \left(\frac{A}{\sigma_A} \right)^2. \quad (\text{A.18})$$

The variance is calculated thus

$$\sigma_A^2 = \left(\frac{\partial A}{\partial A_I} \right)^2 \cdot \sigma_{A_I}^2 + \left(\frac{\partial A}{\partial A_Q} \right)^2 \cdot \sigma_{A_Q}^2 \quad (\text{A.19})$$

$$= \frac{A_I^2}{A^2} \cdot \sigma_{A_I}^2 + \frac{A_Q^2}{A^2} \cdot \sigma_{A_Q}^2. \quad (\text{A.20})$$

In the case of $\sigma_{A_I} = \sigma_{A_Q} = \sigma_{A_{I,Q}}$, the variance becomes

$$\sigma_A^2 = \sigma_{A_{I,Q}}^2. \quad (\text{A.21})$$

Therefore for practical reasons the SNR has been calculated as

$$SNR_A = \frac{A_{\max}^2}{\frac{\sigma_{A_I}^2 + \sigma_{A_Q}^2}{2}}, \quad (\text{A.22})$$

in the experiments after verifying that $\sigma_{A_I} \simeq \sigma_{A_Q}$.

A.5 Theoretical phase noise due to the limited amplitude SNR

The phase is calculated from the two sensor outputs I and Q. It is given by

$$P = \text{angle}(A_I/A_Q) \equiv \arctan(A_I/A_Q) \quad (\text{A.23})$$

Its variance is

$$\sigma_P^2 = \left(\frac{\partial P}{\partial A_Q}\right)^2 \cdot \sigma_{A_I}^2 + \left(\frac{\partial P}{\partial A_I}\right)^2 \cdot \sigma_{A_Q}^2 \quad (\text{A.24})$$

$$= \left(\frac{A_Q}{A^2}\right)^2 \cdot \sigma_{A_I}^2 + \left(\frac{A_I}{A^2}\right)^2 \cdot \sigma_{A_Q}^2. \quad (\text{A.25})$$

if we assume $\sigma_{A_I} = \sigma_{A_Q} = \sigma_{A_{I,Q}}$ and introduce Eq. A.18, we get

$$\sigma_P = \frac{\sigma_{A_{I,Q}}}{A} \quad (\text{A.26})$$

$$= \frac{1}{\sqrt{\text{SNR}_A}}. \quad (\text{A.27})$$

Bibliography

- [1] B. M. Hoeling, A. D. Fernandez, R. C. Haskell, E. Huang, W. R. Myers, D. Petersen, S. E. Ungersma, R. Wang, M. E. Williams, and S. E. Fraser, "An optical coherence microscope for 3-dimensional imaging in developmental biology," *Opt. Express*, vol. 6, pp. 136–145, Mar. 2000.
- [2] B. E. A. Saleh, *Photoelectron Statistics*, ch. 5.2. New York: Springer Verlag, 1978.

Acknowledgements

This work was accomplished at the Swiss Center for Electronics and Microtechnology (CSEM) SA, Photonics Division, located in Zurich. It has been supported by the Albert Koechlin Stiftung AKS, Lucerne.

I would like to thank my Ph.D. supervisor, Prof. Peter Seitz, for the freedom and support he gave to me. Thank you for believing in me!

I owe special thanks to Michael Lehmann, for all the pixel design discussions, for the introduction to high-speed imager design, for the practical help on IC tools, etc. You always took the time for a coffee break with me when I needed it, thank you! I like sharing the office with you very much, and even more, I like going climbing with you!

Matthias Schweizer and Michael Richter developed the camera electronics hosting the sensor and Matthias did the firmware programming. Without you, this sensor would never ever have worked. But much more than for your work, I want to thank you for the time we've spent together. I really enjoy having fun with you. Matthias, I owe you so much, you always had an open ear for me concerning work, life, or anything.

Claus Urban did most of the optical design needed for this work. Claus, thanks for helping me so much with my thesis and for all the inspiring discussions! I hope a good part of your many ideas will become experimental set-ups and even products some day!

I'm grateful to Thierry Zamofing, who did all the software programming. Thank you for your flexibility to modify the software again and again.

Furthermore, I would like to thank all the others, who work with me at the Image Sensing Group or in the Photonics Division: David Beyeler, Nicolas Blanc, Bernhard Büttgen, for the fruitful discussions about his related work, Roger Cook, for the English, the digital, and the fun, Christiane Gimkiewicz, Rolf Kaufmann, for the discussions about real physics, Felix Lustenberger, Peter Metzler, for sharing his profound

experience in any imaginable field, Simon Neukom, Thierry Oggier, for the encouragements, Jörn Pedersen, Rodrigo Rüttimann, for the fast mechanical support, and Philipp Zeller, for the help on optical problems!

I'm very grateful for my parents and my sisters, who always encouraged me and believed in me!

Finally and most of all I want to thank my wonderful wife and best friend Christine, who supported me in all the joyful and all the difficult times through this thesis. Without your support, I would not have achieved it! Life is so much better with you!

Ps. 69:31

Curriculum Vitae

I was born on Aug. 28, 1975 in Schaffhausen, Switzerland. After finishing high-school at the Kantonsschule Schaffhausen in 1995 (Matura Type B), I went to Togo for 5 months as a development volunteer with Mercy Ships / YWAM.

I enrolled at the Institute of Microtechnology, University of Neuchâtel, Switzerland, in 1996, and received a Diploma (M.Sc.) in Physical Electronics in 2001. From 2001 to 2005, I was employed as a PhD student and performed my dissertation research in the Photonics Division at the Centre Suisse d'Electronique et de Microtechnique SA in Zurich, Switzerland.

Besides optical coherence tomography, my main interests are analog and mixed-signal circuit design for smart pixel and high-speed imagers.